Fast transport of single atoms in optical lattices using quantum optimal control

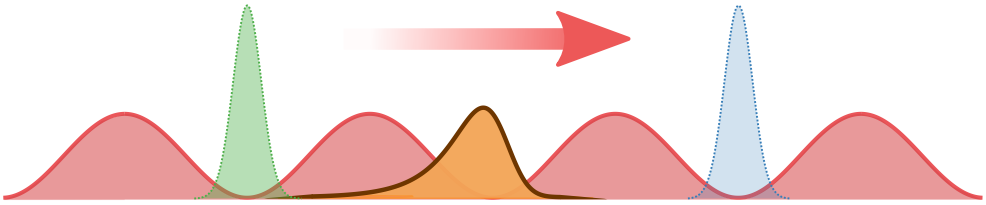

Masterarbeit in Physik

von

Thorsten Georg Groh

angefertigt im

Institut für Angewandte Physik,

vorgelegt der

Mathematisch-Naturwissenschaftlichen Fakultät

der

Universität Bonn

im

April 2018.

1. Gutachter
Prof. Dr. Dieter Meschede

2. Gutachter
Prof. Dr. Martin Weitz

Abstract

This thesis describes the theoretical and experimental work for reaching fast, high fidelity transport operations of single cesium atoms in a state-dependent optical lattice. By applying optimal control theory to position and depth of the optical lattice potential and using a computer simulation judging the fidelity, fast transport sequences preserving the internal atomic quantum state and preventing any motional excitation can be identified. To allow transport times down to a few microseconds the feedback control system used for steering depth and position of the optical lattice deterministically is overdriven in a controlled way. Transport induced motional excitations are measured experimentally by means of a special microwave sideband spectroscopy, which is improved to reliably detect any excitation and allows a full tomography of the vibrational states of the anharmonic optical lattice potential. Optimal control sequences allowing single site transport of atoms in the oscillation period of the trapping potential are believed to reach the fundamental quantum speed limit of the system.

Contents

Introduction

In the recent years trapped ultracold atoms have become a versatile platform for a variety of quantum optical applications. Atomic optical lattice clocks for example are currently the most stable, and therefore most precise, timekeepers in the world [1]. State of the art atomic clocks now reach fractional systematic uncertainties down to 1×10^{-18} [2, 3] and instabilities in the order of 1×10^{-16} at 1 s [2, 4, 5] triggering even discussions about redefinition of the International System of Units (SI) second [5].

Neutral atoms in optical lattices also represent a strong contender in the pursuit of quantum computing and quantum simulation. With the advantage of high controllability and tuneability, these experiments can easily deal as quantum simulators [6] mimicking the Hamiltonian of other systems. This allows not only simulating known matter, like solid state systems [7–9], but also artificial quantum matter, like topological insulators [10]. In the last years solid-state topological insulator devices have attained a high level of control enabling the demonstration of quantum devices such as electronic Mach-Zehnder and Hong-Ou-Mandel-like interferometers [11, 12]. However solid state topological insulator systems still face a lot of experimental challenges like high magnetic fields or the need for cryogenic temperatures to suppress finite temperature effects [13]. Cold atoms trapped in optical lattices instead provide the experimenter with high precision control over the system at hand. The depth of the trapping potential and therefore the tunneling rate to neighboring lattice sites can be directly tuned by changing the power of the lattice beams using electro- or acousto-optical modulators [14]. Methods for single-atom state preparation and detection e. g.by fluorescence imaging [14] of the internal and external states of optically trapped atoms, state-dependent optical lattice schemes in two dimensions [10], as well as imaging techniques with single lattice-site resolution [15–17] have been developed in the last years. The current state of the art experiments pave the way for scalable quantum computers [18] with the ability for the realization of fundamental quantum gates [19], quantum error correction [20] or topologically protected surface codes [21].

The building block of our research in Bonn is the discrete-time quantum walk (DTQW), i.e. the quantum mechanical equivalent of the classical random walk. Therefore single massive cesium atom are trapped in a one-dimensional state-dependent optical lattice [14] and quantum information is encoded in two long-lived hyperfine ground states as well as in the spatial position of the lattice. The DTQW protocols are defined by periodic sequences consisting of internal state rotations and state-dependent spatial translations, which makes the experiments fall under the class of Floquet systems. This driving provides the flexibility of tuning the quantum system, which allowed the realization of atomic quantum interferometers with massive particles like Hong-Ou Mandel interferometers [14] or experiments on the violation of the Leggett-Garg-Inequality using ideal negative measurements [22]. The driving also gives rise to novel properties not possessed by static quantum systems. For example DTQW in 1D described by the theory of Floquet topological insulators [23] show a much richer topological phase diagram [24] than expected by the theory of non-driven topological systems [25]. These topological nontrivial phases are directly accessible by just varying the protocol of the walk evolution and the associated topologically protected edge states even show robustness against environmental induced decoherence [10]. Therefore DTQWs with ultracold neutral atoms trapped in optical lattices offer a versatile and highly tunable platform for the experimental investigation of topological insulator materials.

But making a quantum system tunable requires full control over all possible degrees of freedom.

In the case of DTQW with neutral atoms this demands not only for controlling the preparation and induced transition between the internal electronic states of the atom, but also control over the external state – the spatial position in the optical lattice and transport between lattice sites. Our recently built, fast, high-precision optical polarization synthesizer [14, 26] allows control over the relative position between the two standing waves of the polarization-synthesized optical lattice to a precision of 1.2 Å, which corresponds to less than 0.03 % of the lattice site spacing. Together with the possibility to cool the atoms to the motional ground state of the lattice potential by means of sideband-resolved microwave transitions this allows a robust positioning of the atom in the static dipole trap even for long storage times [14].

Interferometry applications like DTQWs require transport operations of single atoms over multiple lattice sites, where the atomic internal quantum state should not be altered. In the case of optical lattices this does not only includes the spin state, but also the (quantized) motional excitation inside the lattice potential wells. One approach to achieve transport operations which do not excite the atom to higher motional states is by adiabatically ramping the trap position and therefore dragging the atoms slowly with the moving lattice. But unfortunately this also limits the speed of operations extremely, often to times much longer than the coherence time of the quantum system, which is the main limitation for long multiple-step experimental sequences.

Shortcuts to adiabaticity can be obtained by the use of optimal control theory. By effectively allowing arbitrary modulations of the transport trajectories both the transport fidelity as well as the transport time can be optimized by employing mathematical optimization algorithm. Optimal control generally describes the methods used to find a control feedback which minimizes or maximizes a specific performance criterion of a control system overcoming the iterative trial-and-error attempt of classical control system design [27]. Constraint optimal control approaches also allow to include any practical limits on the laboratory controls [28]. In the last years, optimal control theory was applied to numerous quantum experiments obtaining control in manipulating and initialization of photonic, atomic or ionic states [29–31]. High-speed operations in quantum systems is a key element in quantum information processing and quantum computation and in the last years the number of optimal control applications grew continuously, for instance providing the experimenters with methods to counteract decoherence [32]. In ultracold atom experiments quantum optimal control was used to e.g. realize quantum phase transitions [33], to produce entanglement by trap shaking [34] and to interfere matter-waves [35]. Until now optimal control for transporting single particles was only applied to single ions in segmented linear traps allowing fast transport of ions over macroscopic distances without producing significant excitations [36]. Numerical optimization approaches based on the theory of optimal control were already successfully applied to atoms trapped by optical tweezers [37, 38]. The theoretical limitation of dynamical speedups due to optimal control theory is only given by the quantum speed limit. This fundamental limit of any quantum system [39] results from the Heisenberg energy time uncertainty relation. Whether one can reach this speed limit in the context of fast atomic transport should be answered in this thesis.

Outline

This thesis is divided into four parts: In chapter 1 the theoretical background and experimental realization of an one-dimensional optical lattice for cesium atoms is presented. In chapter 2 is shown how polarization synthesis is used to allow transporting atoms dependent on their internal qubit state. After recapping the microwave sideband cooling scheme and presenting a motional state tomography scheme in chapter 3, chapter 4 introduces the ideas of optimal control theory, which are then applied to the problem of transporting single atoms under the demand for speed and preservation of their quantum states. Using a computer simulation of the quantum system fast, high-fidelity transport sequences are identified and analyzed experimentally.

Chapter 1

State-dependent optical lattices

Optical lattices are spatially periodic potentials generated by the interference of counter-propagating laser beams and are widely used for cooling, trapping, shaping and transporting atomic clouds, Bose-Einstein condensates and single atoms. While most experiments rely on optical lattices which trap particles independent of their quantum state, our experimental setup allows the state-dependent control over the trapped atoms, which enables for instance the spin-dependent shift operation in quantum walk sequences or the application of sideband-resolved microwave spectroscopy.

State-dependent trapping

The key difference between quantum and classical mechanics is the phenomenon of superposition of states giving rise to interference effects and the uncertainty principle. When working with quantum systems with multiple levels in the context of quantum information applications or e. g. atomic quantum interferometers for proving fundamental physical properties and behaviors, the different levels are not only used for storing quantum information, it is also necessary to couple different states allowing conditional manipulation of quantum information as needed for example for quantum walks or enabling quantum gates for quantum computing. In our experiment we encode quantum information in the two outermost atomic hyperfine ground states of Cesium,

$$\boxed{\begin{aligned} |\uparrow\rangle &= |J = 1/2,\ I = 7/2\rangle \otimes |F = 4,\ m_F = 4\rangle \\ |\downarrow\rangle &= |J = 1/2,\ I = 7/2\rangle \otimes |F = 3,\ m_F = 3\rangle \end{aligned}}, \tag{1.1}$$

as shown in figure 1.1. We will call these states spin states or qubit in the following. Furthermore quantum information is also encoded in the position degree of freedom, where the Wannier states best describe the atomic wave packet localized at some position $|x\rangle$. Coupling these two degrees of freedoms can be realized by state-dependent optical dipole forces, where the trapping potential depends on the spin state in which the atom is located. By individually controlling the position of these trapping potentials state-dependent transport of atoms can be realized which in our experiment is an essential tool for quantum interferometer applications.

The concept of state-dependent optical trapping goes back to Deutsch [40] and Jaksch [41] around 1998 and relies on the differences in the dipole interaction between optical radiation and individual internal atomic level. It has since been used experimentally in a lot of different applications, reaching from transport of neutral atoms while keeping its coherence [19] to quantum walks of single neutral atoms [42].

The big challenge of state-dependent trapping is to engineer two spatially overlapped, but independently controllable optical dipole traps which just have effect on atoms in a specific internal atomic state.

In this chapter, I will first reflect the concepts of the optical dipole force as well as the properties and limits of optical lattices in section 1.1 and explain our state-dependent optical lattice setup in 1.2,

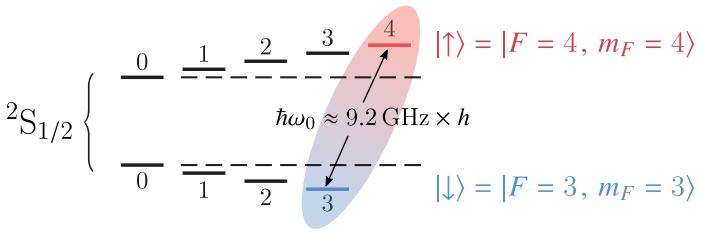

Fig. 1.1: Qubit states. The outermost hyperfine states $|\uparrow\rangle = |^2S_{1/2};\, F = 4,\, m_F = 4\rangle$ and $|\downarrow\rangle = |^2S_{1/2};\, F = 3,\, m_F = 3\rangle$ in the $^2S_{1/2}$ ground state of cesium build the qubit states of our atom interferometer. The energy difference between these two hyperfine levels is enlarged to $\hbar\,\omega_0 \equiv h\,\nu_0 \approx 9.2\,\mathrm{GHz} \times h$ due to a Zeeman splitting of the m_F hyperfine levels resulting from a magnetic field of $|\boldsymbol{B}_0| = 3\,\mathrm{G}$, which forms the quantization axis for angular momentum states.

before taking a closer look at the form and distribution of quantum states trapped by lattice potential in section 1.3 and 1.4.

1.1 Optical dipole potential

The optical dipole force is the attractive or repulsive force induced by the interaction between atomic energy levels and a (far) detuned laser field. It can be understood semiclassically (see e. g. [43]) as the electric field $\boldsymbol{E}(\boldsymbol{x},t) = \hat{\boldsymbol{\epsilon}}\, E_0(\boldsymbol{x}) \cos(\omega t)$ inducing an atomic dipole moment $\boldsymbol{\mu}(\boldsymbol{x},t) = \hat{\boldsymbol{\epsilon}}\, p(\boldsymbol{x}) \cos(\omega t)$ oscillating at the driving frequency ω with amplitude $p(\boldsymbol{x}) = \alpha(\omega)\, E(\boldsymbol{x})$ given by the complex polarizability α. The effective potential induced by this coupling is then given by

$$U(\boldsymbol{x}) = -\frac{1}{2}\langle \boldsymbol{\mu}(\boldsymbol{x},t) \cdot \boldsymbol{E}(\boldsymbol{x},t)\rangle_t = -\frac{1}{2\epsilon_0 c}\,\mathrm{Re}(\alpha(\omega))\, I(\boldsymbol{x}) \tag{1.2}$$

where $\langle\cdot\rangle_t$ denotes the time average and $I(\boldsymbol{x}) = 2\epsilon_0 c\,|E(\boldsymbol{x})|^2$ the light field intensity. Taking the expression for the polarizability α derived from a classical Lorentz oscillator with resonance frequency ω_0 and using the rotating wave approximation, the dipole potential can be expressed as

$$U(\boldsymbol{x}) = \frac{3\pi c^2}{2\omega_0^3}\frac{\Gamma}{\Delta} I(\boldsymbol{x}) \tag{1.3}$$

where $\Delta = \omega - \omega_0$ is the detuning of the light field to the resonance frequency of the atomic oscillator and Γ the on-resonance damping rate is determined by the dipole matrix element between ground $|g\rangle$ and excited state $|e\rangle$ [44],

$$\Gamma = \frac{\omega_0^3}{3\pi\hbar\epsilon_0 c^3}\,|\langle e|\,\boldsymbol{\mu}\,|g\rangle \cdot \boldsymbol{\epsilon}|^2\ . \tag{1.4}$$

For a red-detuned light field ($\Delta < 0$) the potential is attractive and a blue-detuned dipole trap ($\Delta > 0$) gives rise to an repulsive potential trapping the atoms in the intensity maxima of the light field.

The cesium atoms trapped in our experiment exhibit a complex electronic multilevel substructure, which demands for a quantum mechanical description of the problem. The interaction between far-detuned light field and the electronic level structure of the atomic quantum system can be expressed semi-classically as the interaction Hamiltonian

$$\mathscr{H}_{\mathrm{int}}(t) = -\boldsymbol{\mu} \cdot \boldsymbol{E}(t) \tag{1.5}$$

where $\boldsymbol{\mu}$ now denotes the dipole operator. The optical dipole potential affecting an atom in ground state $|i\rangle$ can then be understood as the light induced energy shift – the so called ac Stark effect –

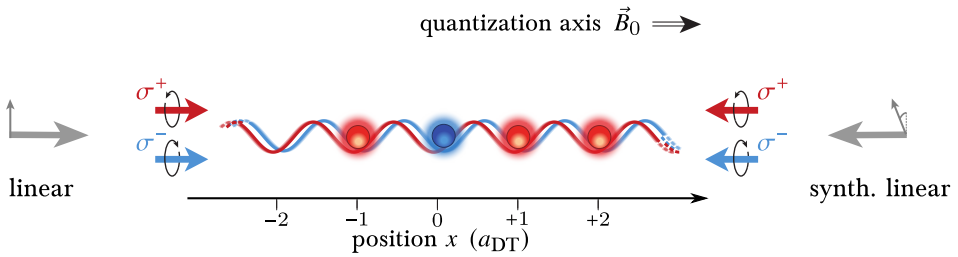

Fig. 1.2: State-dependent optical lattices resulting from a superposition of a linear polarized beam with a polarization synthesized beam. This results in two standing waves of σ^+ and σ^- polarized light forming a dipole potential for the two spin states, while allowing the independent control on the positions of the two beams. The quantization axis is defined by a magnetic field of $|\boldsymbol{B}_0| = 3\,\mathrm{G}$ along the direction of the optical lattice.

arising from second order perturbation theory[1]

$$\boxed{U^i(\boldsymbol{x}) = \Delta E_{|i\rangle,\text{ac Stark}} = \frac{1}{4\hbar}\sum_{k\neq i}\frac{|\langle k|\,\mathscr{H}_{\text{int}}(0)\,|i\rangle|^2}{\omega-\omega_{ki}} = \frac{1}{2\hbar\epsilon_0 c}\sum_{k\neq i}\frac{|\langle k|\,\boldsymbol{\mu}\,|i\rangle\cdot\boldsymbol{\epsilon}|^2}{\omega-\omega_{ki}}I(\boldsymbol{x})}, \tag{1.6}$$

where $\omega_{ki} = \omega_k - \omega_i$ is the transition frequency between the ground state $|i\rangle$ and excited state $|k\rangle$.

1.1.1 Optical lattice

The optical dipole potential in our experiment are formed by two counter-propagating Gaussian laser beams at $\lambda_{\mathrm{dt}} = 865.9\,\mathrm{nm}$ wavelength which are focused to a waist of $w_{\mathrm{dt}} = 17\,\mu\mathrm{m}$ inside the vacuum glass cell and form a standing wave pattern in the longitudinal direction, which I will denote by x. The phase ϕ of one of the two beams can be modulated via an acousto-optical modulator (AOM), as explained in detail in section 2.1, and the spatial intensity pattern as a function of longitudinal position x and radial distance $\rho = \sqrt{y^2+z^2}$ can therefore be written as

$$I(\boldsymbol{x}) = I_0\cos^2\left[k_{\mathrm{dt}}x - \phi/2\right]\mathrm{e}^{-2\rho^2/w_{\mathrm{dt}}^2} \tag{1.7}$$

where $k_{\mathrm{dt}} = 2\pi/\lambda_{\mathrm{dt}}$ is the lattice beam wavevector. Here we neglected any spatial aberrations as well as the curvature and Gouy phase of the Gaussian beams, which is a good approximation for the region of interest – a few hundred lattice sites in which experiments are performed. The resulting dipole interaction therefore forms a periodic sinusoidal potential with lattice spacing $a_{\mathrm{dt}} = \lambda_{\mathrm{dt}}/2$, which can be written as

$$\boxed{U(\boldsymbol{x}) = -U_0\,\cos^2\left[k_{\mathrm{dt}}(x-x_0)\right]\mathrm{e}^{-2\rho^2/w_{\mathrm{dt}}^2}} \tag{1.8}$$

and is commonly known as an optical lattice. The lattice position x_0 can be controlled by modulating the phase ϕ via the AOM and therefore allows the transport of cooled, trapped atoms by dragging them along with the lattice (see chapter 1). I will define the position of the lattice to be

$$x_0 = \frac{\lambda_{\mathrm{dt}}}{2}\frac{\phi}{2\pi} = a_{\mathrm{dt}}\frac{\phi}{2\pi} \tag{1.9}$$

A more detailed description of the experimental can be found in [45] for the main experimental apparatus and [14] for the improvements implemented in the last years.

1.1.2 Scattering of lattice photons

The calculation above just took into account the trapping effect of the optical dipole potential and it seemed, that allowing high laser intensities to generate really deep lattices is the way to go, to

[1] See derivation in A.1.

optimally trap even not perfectly cooled atoms. Though one has to take into account the likelihood that trapped atoms also scatter light, which leads to two undesired effects.

One can approximate the quantum system as a two level system which coupled via the dipole trap radiation. Under this assumption, as shown in Robens [14], and using the generalized Fermi's golden rule, the photon scattering rate can be calculated and is given by

$$\Gamma_{\text{scat}} = \frac{6\pi c^2}{\omega_0^3} \left(\frac{\Gamma}{\Delta}\right)^2 I, \tag{1.10}$$

and is directly proportional to the intensity I of the dipole trap light at the position of the atom.

From the rules of energy and momentum conservation, each lattice photon scattered on the atom now increases the total energy of the atoms by $\Delta E = 2\,E_{\text{rec}}$, where the recoil energy is given by

$$E_{\text{rec}} = \frac{h^2}{2\,M\,\lambda_{\text{dt}}^2}, \tag{1.11}$$

with $M = 2.273\,395\,7 \times 10^{-25}\,\text{kg}$ the cesium-137 atomic mass. This leads to heating of the atoms, which increases the mean motional state and can also lead to a complete loss of the atom.

The second effect, which is not so important for the here considered transport of single atoms, but for it's application like atomic interferometer experiments, is decoherence. Scattering of lattice photons leads both to dephasing in the spatial position as well as in the spin degree of freedom. When a lattice photon is scattered from the atom, the quantum position state is effectively measured, which destroys spatial coherence by projecting the quantum walker's wave packet into a single lattice site. The main effect leading to decoherence in the spin state, is elastic Rayleigh scattering, which preserves the spin populations and just leads to pure spin dephasing. In a simple model [46], the decoherence rate, describing the loss of information with time is directly proportional to the intensity of the lattice potential,

$$\gamma_{\text{dec}} \propto I \left(\frac{1}{\Delta_{\text{D}_2}^2} - \frac{1}{\Delta_{\text{D}_1}^2}\right). \tag{1.12}$$

Here Δ_{D_1} and Δ_{D_2} are the detunings of the lattice beam with respect to the D_1 and D_2 line.

Therefore, to reduce the photon scattering rate of the optical lattice beams to a minimum, the laser intensities of the lattice beams have to decreased as much as possible and far of-resonant dipole traps are preferred, since both the photon scattering rate as well as the decoherence rate scale as $1/\Delta^2$, while the potential scales only as $1/\Delta$. However, to ensure that even not perfectly cooled atoms are still trapped properly and also due to a limited range for of our intensity lock setup, which is presented in chapter 2, the laser intensity should not be lowered below $5\,\mu\text{K}$ to $10\,\mu\text{K}$.

The experimental sequences cosidered in this thesis will mainly involve two different intensity levels. Loading the atoms from the MOT to the lattice as well as imaging with the EMCCD camera demands for high laser powers to obtain good trapping and confinement. We therefore employ our deep optical lattice by providing $\sim 30\,\text{mW}$ of optical power in each of the two counter-propagating laser beams, which results in a trap depth of about $U_0 = 370\,\mu\text{K}\times k_B$. To reduce decoherence and scattering induced losses during experimental sequences we then reduce the potential depth to about $80\,\mu\text{K}\times k_B$ by using only $6\,\text{mW}$ of optical power per lattice beam. As we will see in chapter 4, optimal control transport with transport times down to the quantum speed limit can demand – due to technical limitations of our amplitude locks – for even shallower traps with trap depths down to $10\,\mu\text{K}\times k_B$. All these different modes of operation give rise to a wide range of trap depths.

1.2 State-dependent optical lattice for cesium

Although we are interested in state-dependently trapping the two hyperfine structure qubit states $|\uparrow\rangle$ and $|\downarrow\rangle$, it is useful to first ignore the hyperfine structure and look at AC vector polarizabilities of the

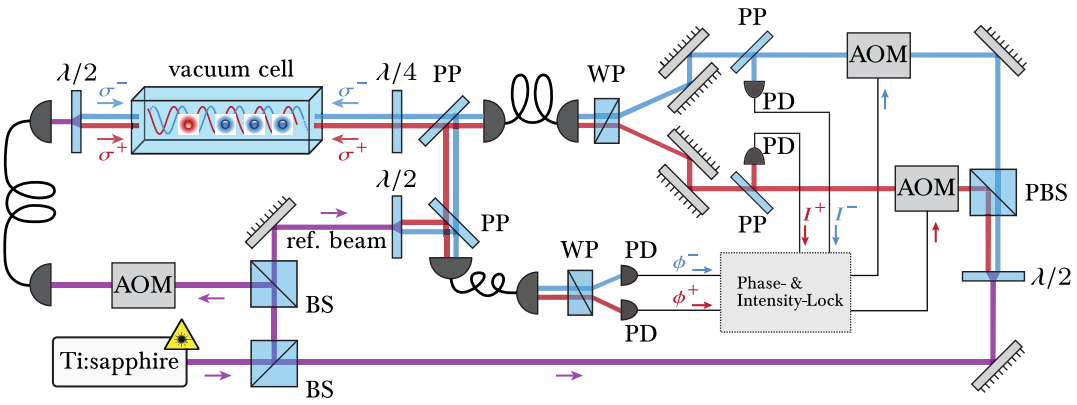

Fig. 1.3: Optical lattice setup. The laser source – a Ti-sapphire laser system delivering up to 2.5 W output power at a wavelength of $\lambda_{dt} = 865.9\,\mathrm{nm}$ – is split using a non-polarizing beamsplitter (BS) into two parts of equal intensity. Using a half-wave plate ($\lambda/2$) combined with a polarization beam splitter, one of the beams is splitted into two components which later form the two circular polarized lattice beams. The optical dipole traps are formed by overlapping this pair of laser beams (coming from the right) with a counter-propagating linear polarized beam (coming from the left) which effectively forms two standing waves of circular polarization. Phase and intensity control of the lattice beams is achieved via acousto-optical modulators (AOM) controlled by an electronic lock loop. The electronic phase and intensity lock is based on a direct measurement of the intensities of the two circular polarized arms – detected by a photodiode (PD) combined with a pick-up plate (PP) – as well as a measurement of the beating signal between the polarization synthesized and reference beam from which the relative phase of the two lattices can be determined. The electronic lock setup is shown in more detail in figure 2.2. Splitting and overlapping beams of different polarization is done using multiple Wollaston prisms (WP). The set points controlling trap depth and lattice position are directly controlled by the laboratory computer system. For simplicity the pure intensity lock of the linear polarized reference beam, indicated by the AOM on the left hand side, is omitted.

two fine structure states

$$\begin{aligned} |+\rangle &= |L = 1/2,\ S = 1/2\rangle \otimes |J = 1/2,\ m_J = +1/2\rangle \\ |-\rangle &= |L = 1/2,\ S = 1/2\rangle \otimes |J = 1/2,\ m_J = -1/2\rangle \end{aligned} . \tag{1.13}$$

As illustrated in figure 1.4 one can now find a wavelength $\lambda^\star_{dt}$, which is blue detuned to the D_1 transition ($^2S_{1/2} \rightarrow {}^2P_{1/2}$) and red detuned to the D_2 transition ($^2S_{1/2} \rightarrow {}^2P_{3/2}$), such that an atom in state $|\pm\rangle$ does not experience any potential arising from $\sigma^\mp$-polarized light. The different sign in the detuning then cancels the attractive and repulsive contribution from the two $m_J = \mp 1/2$ states, one in $^2P_{1/2}$ and one in $^2P_{3/2}$. Therefore state $|\pm\rangle$ just sees the attractive potential arising from $\sigma^\pm$-polarized light, which allows a state-dependent lattice setup. The so-called magic wavelength for cesium can be calculated numerically by use of equation (1.6) taking into account the coupling to all excited hyperfine states and lies at $\lambda^\star_{dt} = 865.9\,\mathrm{nm}$. I will set $\lambda_{dt} = \lambda^\star_{dt}$ in the following.

Experimental setup

In the experiment, we like to overlap two standing waves of σ^+ and σ^- polarized light forming a dipole potential for the two spin states, while allowing the independent control on the positions of the two beams. The quantization axis is defined by a magnetic field of $|\boldsymbol{B}_0| = 3\,\mathrm{G}$ along the direction of the dipole laser beams. Therefore we superpose a linear polarized beam with polarization $\hat{\boldsymbol{\epsilon}}_{lin}$ with a pair of left- and right-handed polarized beams of polarization $\hat{\boldsymbol{\epsilon}}_\pm$, which are individually controlled by two AOMs imprinting the phases $\phi^\pm$ on the light fields. The laser source is a Ti-sapphire laser system which delivers up to 2.5 W output power. Its beam is separated into the counter-propagating arms of the optical lattice using a beamsplitter. The setup is shown in detail in figure 1.3.

Using the fact that the linear polarization of the reference beam can be expressed as a superposition

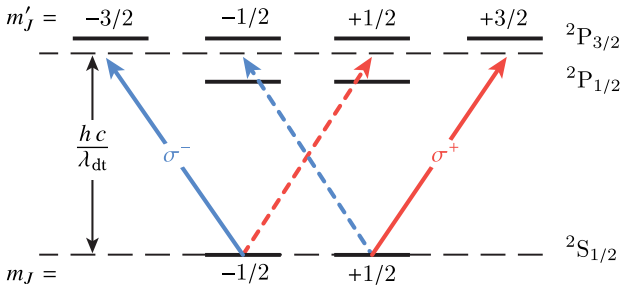

Fig. 1.4: State-dependent dipole force. At the magic wavelength $\lambda_{dt} = \lambda^\star_{dt}$ the attractive and repulsive forces associated to the four $m_J = \pm 1/2$ states cancel out each other in pairs, so that atoms in state $|+\rangle$ just see the attractive potential arising from σ^+-polarized and atoms in $|-\rangle$ only the one arising from σ^--polarized light.

of the two circular polarizations, $\hat{\boldsymbol{\epsilon}}_{\text{lin}} = (\hat{\boldsymbol{\epsilon}}_+ + \hat{\boldsymbol{\epsilon}}_-)/\sqrt{2}$, the electric field can be written as

$$\begin{aligned}\boldsymbol{E}(\boldsymbol{x},t) &= A(\rho)\left[E_0\,\hat{\boldsymbol{\epsilon}}_{\text{lin}}\,\mathrm{e}^{\mathrm{i}k_{dt}x} + \left(E_0^+\,\hat{\boldsymbol{\epsilon}}_+\,\mathrm{e}^{\mathrm{i}\phi^+} + E_0^-\,\hat{\boldsymbol{\epsilon}}_-\,\mathrm{e}^{\mathrm{i}\phi^-}\right)\mathrm{e}^{-\mathrm{i}k_{dt}x}\right]\mathrm{e}^{-\mathrm{i}\omega t} \\ &= A(\rho)\left[E_0^+\,\hat{\boldsymbol{\epsilon}}_+\left(1+\mathrm{e}^{-\mathrm{i}(2k_{dt}x-\phi^+)}\right) + E_0^-\,\hat{\boldsymbol{\epsilon}}_-\left(1+\mathrm{e}^{-\mathrm{i}(2k_{dt}x-\phi^-)}\right)\right]\mathrm{e}^{\mathrm{i}(k_{dt}x-\omega t)}\end{aligned} \tag{1.14}$$

where we assumed that the intensity of the linear polarized reference beam is always set to the summed intensity of the two circular polarized beams, $E_0^{+2} + E_0^{-2} = {E_0}^2$ and that the radial dependency $A(\rho) = \mathrm{e}^{-\rho^2/w_{dt}^2}$ is common for all beams. At the magic wavelength, $\lambda_{dt} = \lambda^\star_{dt}$, an atom in the state $|\pm\rangle$ exhibit just the light force from the $\sigma^\pm$-polarized part, the effective dipole potential reads $U^\pm(\boldsymbol{x}) = -U_0^\pm \cos^2\left[k_{dt}(x - x_0^\pm)\right]\mathrm{e}^{-2\rho^2/w_{dt}^2}$, where $U_0^\pm \propto I_0^\pm \propto {E_0^\pm}^2$ [1] and $x_0^\pm = a_{dt}\phi^\pm/(2\pi)$, which can be tuned by controlling the radio signal of the two AOMs.

The individual control over the phases $\phi_\pm$ and amplitudes $E_0^\pm$ of the $\sigma^\pm$-polarized light can also be viewed as a complete synthesis of the polarization of the lattice beam coming from the right [26]. From equation (1.14) we can see, that the polarization angle θ_{pol} and ellipticity ϵ_{pol} are given by the relative difference between the control parameters of the two polarizations,

$$\theta_{\text{pol}} = \phi^- - \phi^+, \qquad \epsilon_{\text{pol}} = \frac{E_0^{-2} - E_0^{+2}}{E_0^{-2} + E_0^{+2}}, \tag{1.15}$$

which allows reaching any point on the Poincaré sphere and therefore to synthesize any polarization.

Dipole trap crosstalk

Taking into account the cesium nuclear momentum and by use of the Clebsch-Gordon coefficients, $\langle J,\, I,\, F,\, m_F \,|\, I,\, m_I,\, J,\, m_J\rangle$, we can now project the hyperfine qubit states on the considered fine structure ground states. To obtain the projection, we sum over all possible m_J and m_I, $|J,\, I,\, F,\, m_F\rangle = \sum_{m_I=-I}^{I}\sum_{m_J=-J}^{J}\langle J,\, I,\, F,\, m_F \,|\, I,\, m_I,\, J,\, m_J\rangle\,|I,\, m_I,\, J,\, m_J\rangle$, and the non-vanishing terms read

$$\begin{aligned}|\uparrow\rangle &= \quad |I = 7/2, m_I = 7/2\rangle \otimes |+\rangle \\ |\downarrow\rangle &= \sqrt{\frac{1}{8}}\,|I = 7/2, m_I = 7/2\rangle \otimes |+\rangle - \sqrt{\frac{7}{8}}\,|I = 7/2, m_I = 5/2\rangle \otimes |-\rangle\end{aligned}. \tag{1.16}$$

While qubit state $|\uparrow\rangle$ feels the same dipole potential as $|+\rangle$, the other state $|\downarrow\rangle$ experiences a sum of the two potentials seen by $|+\rangle$ and $|-\rangle$. By inserting equation (1.16) into (1.6) one obtains

$$U^\uparrow(\boldsymbol{x}) = U^+(\boldsymbol{x}), \qquad U^\downarrow(\boldsymbol{x}) = \frac{1}{8}\,U^+(\boldsymbol{x}) + \frac{7}{8}\,U^-(\boldsymbol{x}). \tag{1.17}$$

[1] The proportionality factor is given by equation (1.6).

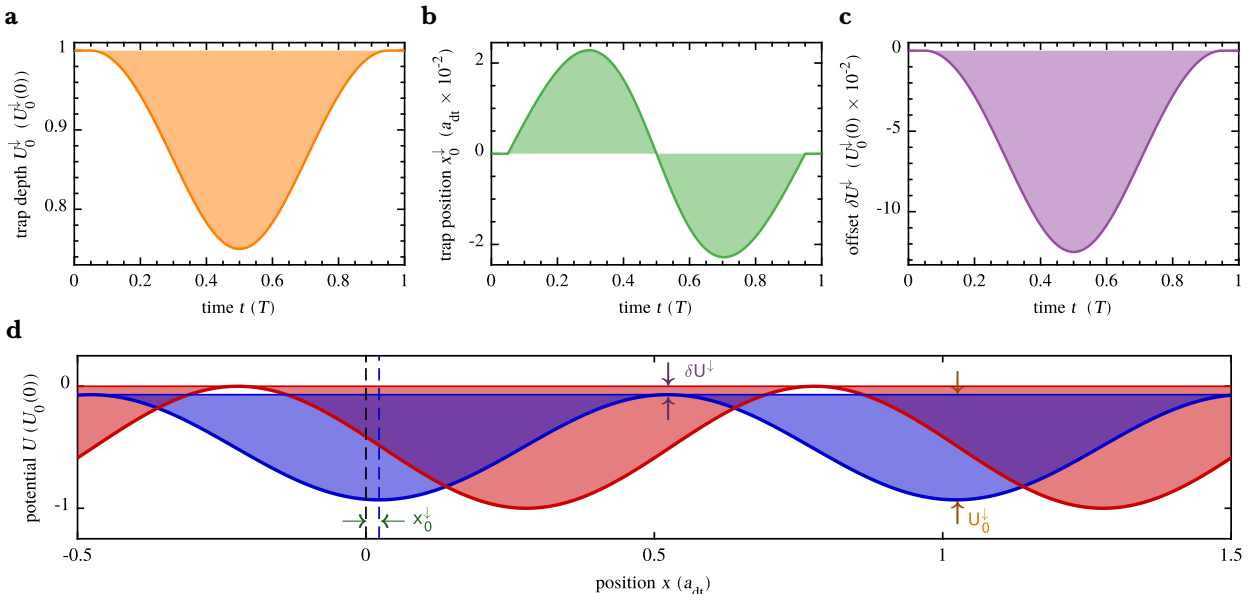

Fig. 1.5: Dipole trap crosstalk for qubit state $|\downarrow\rangle$. The σ^+-polarized lattice is shifted linearly by one lattice site, while the σ^--polarized lattice is kept constant. The total transport time for this shift is denoted by T. (a) trap depth $U_0^\downarrow$, (b) trap position $x_0^\downarrow$ and (c) offset $\delta U^\downarrow$ of the dipole trap seen by spin $|\downarrow\rangle$ vary during the transport. (d) the trapping potentials seen by spin $|\downarrow\rangle$ (blue) and spin $|\uparrow\rangle$ (red) at time $t = 0.3\,T$. The distortion of the spin $|\downarrow\rangle$ potential due to the dipole trap crosstalk is visible.

However, as shown in appendix A.2 one can express this sum as a potential of form (1.8) with an additional offset, which allows to write the potential felt by spin state $|\mathcal{S}\rangle$ with $\mathcal{S} = \uparrow, \downarrow$ as

$$\boxed{U^{\mathcal{S}}(\boldsymbol{x}) = \left\{\delta U^{\mathcal{S}} - U_0^{\mathcal{S}} \cos^2\left[k_{\mathrm{dt}}\,(x - x_0^{\mathcal{S}})\right]\right\} \mathrm{e}^{-2\rho^2/w_{\mathrm{dt}}^2}}, \tag{1.18}$$

where the lattice positions $x_0^{\mathcal{S}}$, trap depths $U_0^{\mathcal{S}}$ and trap depth offsets $\delta U^{\mathcal{S}}$ are given by

$$x_0^\uparrow = x_0^+ \qquad U_0^\uparrow = U_0^+ \qquad \delta U^\uparrow = 0 \tag{1.19}$$

$$x_0^\downarrow = \frac{a_{\mathrm{dt}}}{2\pi} \arctan\left(\frac{s^\pm}{c^\pm}\right) \qquad U_0^\downarrow = \sqrt{s^{\pm 2} + c^{\pm 2}} \qquad \delta U^\downarrow = \frac{1}{2}\left(U_0^\downarrow - \frac{1}{8}U_0^+ - \frac{7}{8}U_0^-\right) \tag{1.20}$$

and where we defined

$$s^\pm = \frac{1}{8}U_0^+ \sin\left(2k_{\mathrm{dt}}x_0^+\right) + \frac{7}{8}U_0^- \sin\left(2k_{\mathrm{dt}}x_0^-\right), \tag{1.21}$$

$$c^\pm = \frac{1}{8}U_0^+ \cos\left(2k_{\mathrm{dt}}x_0^+\right) + \frac{7}{8}U_0^- \cos\left(2k_{\mathrm{dt}}x_0^-\right). \tag{1.22}$$

1.3 Loading atoms from the background gas

The optical lattice is enclosed in a rectangular-shaped glass cell connected to a vacuum chamber with a high-efficiency vacuum pump reducing the inside pressure to less than $10 \times 10^{-10}\,\mathrm{mbar}$. At room temperature, the background vapor of cesium atoms follows a Boltzmann distribution with mean velocity of $\sim 200\,\mathrm{m\,s^{-1}}$. Even in our really deep lattice with a trap depth of $370\,\mu\mathrm{K} \times k_B$, which is used for imaging, the overlap between the Boltzmann distribution of the hot atomic cloud and the available motional states, which are trapped by the optical lattice – the states with energy below $370\,\mu\mathrm{K} \times k_B$ – is below 2×10^{-6}, which makes direct trapping by just switching on the lattice beams nearly impossible. Furthermore, for atom interferometer experiments, as well as in the interest of this thesis, we want the

atoms to be in the motional ground state of the lattice potential, which all demands for the application of cooling techniques.

A magnetic quadrupole field generated by a pair of coils in a anti-Helmholtz configuration combined with three pairs of circular-polarized laser beams at the ${}^2\mathrm{S}_{1/2}\, F = 4 \rightarrow {}^2\mathrm{P}_{3/2}\, F = 5$ (D_2) then creates a three dimensional magneto-optical trap (MOT), which slows down the atoms due to the anisotropic subsequent spontaneous reemission of photons and traps the atoms in the center of the quadrupole field. Off-resonant scattering to the $F = 3$ ground state is dealt with by repumping the atoms back using a second laser resonant on the ${}^2\mathrm{S}_{1/2}\, F = 3 \rightarrow {}^2\mathrm{P}_{3/2}\, F = 4$ (D_2) transition. The intrinsic temperature limit of this method due to subsequent momentum kicks from reemitted photons is given by the Doppler temperature which lies at about $125\,\mu\mathrm{K}$. Sub-Doppler cooling is achieved via extending the optical molasses using pairs of orthogonally circularly polarized counterpropagating laser beams, which creates a viscous friction force for atoms moving in arbitrary directions and cools the trapped atoms to about $10\,\mu\mathrm{K}$.

By ramping up the optical lattice and simultaneously moving the magnetic field offset and finally switching off the MOT fields, as well as the MOT beams, the atoms are loaded to the optical lattice. The overlap between the possible trapped states of the deep imaging lattice and the thermal distribution of the atoms after being cooled by molasses and MOT is about $95\,\%$, which results in a good loading with atom numbers from 20 up to 60, which results in up to half filling of the optical lattice in the field of view of the EMCCD camera (~ 100 sites). To finally bring the trapped atoms to the ground state of the lattice potential, we apply microwave sideband cooling, which will be explained in more detail in chapter 3.

1.4 Atomic states in optical lattices

When one restricts the lattice potential, defined in equation (1.8), to the longitudial, one-dimensional part by setting $\rho = 0$, the periodicity of the potential, $U(x) = U(x + a_{\mathrm{dt}})$, and the associated discrete translational symmetry $x \rightarrow x + a_{\mathrm{dt}}$ allows to write the eigenstates by use of the Floquet theorem. Labeled by their band index $n \in \mathbb{N}^{\geq 0}$ and their quasimomentum k the eigenstates are given by the Bloch wave functions

$$\varphi_{n,\,k} \equiv \langle x|n,\, k\rangle = u_{n,\,k}(x)\, \mathrm{e}^{\mathrm{i}\,k\,x} \tag{1.23}$$

where $u_{n,\,k}(x) = u_{n,\,k}(x + a_{\mathrm{dt}})$ is a periodic function in x. Here we consider the reduced scheme, where the quasimomentum k is restricted and wrapped into the first Brillouin zone $\mathrm{BZ} = \mathbb{R} \cap [-\pi/a_{\mathrm{dt}},\, \pi/a_{\mathrm{dt}})$. The Bloch states are delocalized over the whole lattice. Localized solutions are given by the so-called Wannier states and can be constructed from the Bloch functions as follows:

$$\psi_{n,\,i}(x) \equiv \langle x|n,\, i\rangle = \int\limits_{k\,\in\,\mathrm{BZ}} \mathrm{d}k\; \mathrm{e}^{-\mathrm{i}\,k\,(x_0 + i\,a_{\mathrm{dt}})}\, \varphi_{n,\,k}(x) \tag{1.24}$$

where $i \in \mathbb{Z}$ labels the lattice site. They satisify following orthonormality condition

$$\langle n,\, i|m,\, j\rangle \equiv \int \mathrm{d}x\; \psi^{\star}_{n,\,i}(x)\, \psi_{m,\,j}(x) = \delta_{n,\,m}\, \delta_{i,\,j} \tag{1.25}$$

where * denotes the complex conjugate and $\delta_{a,\,b}$ is the Kronecka delta.

I will now analyze the optical lattice potential as defined in equation (1.8) in more detail and ask for the possible quantum states.

1.4.1 One-dimensional harmonic oscillator

A series expansion of the longitudinal lattice potential $U(x)$ – given by equation (1.8) at $\rho = 0$ – around $x = x_0$ leads to the

$$U(x) = -U_0 + \frac{1}{2} M \omega_{\mathrm{ho}}^2 (x - x_0)^2 + \mathcal{O}(x - x_0)^4 \tag{1.26}$$

where M is the cesium mass and the longitudinal trap frequency $\omega_{\mathrm{ho}} = 2\pi\,\nu_{\mathrm{ho}}$ is defined as

$$\boxed{\omega_{\mathrm{ho}} = 2\pi\sqrt{\frac{2\,U_0}{M\,\lambda_{\mathrm{dt}}^2}}}\,. \tag{1.27}$$

The eigenstates are then given by the motional states located on lattice site i and read

$$\psi_{n,i}^{(\mathrm{ho})} \equiv \langle x|n,\,i\rangle_{\mathrm{ho}} = \frac{1}{\sqrt{2^n\,n!}}\sqrt[4]{\frac{M\,\omega_{\mathrm{ho}}}{\pi\,\hbar}}\,\exp\left(-\frac{M\omega_{\mathrm{ho}}\bar{x}^2}{2\,\hbar}\right)\mathrm{H}_n\left(\sqrt{\frac{M\,\omega_{\mathrm{ho}}}{\hbar}}\,\bar{x}\right)\Bigg|_{\bar{x}=x-x_0-i\,a_{\mathrm{dt}}}\,. \tag{1.28}$$

Here $H_n(\zeta) = (-1)^n\exp(\zeta^2)\frac{\mathrm{d}^n}{\mathrm{d}\zeta^n}\exp(-\zeta^2)$ are the Hermite polynomials and n is a non-negative integer number. The associated eigenenergies are given by

$$E_n^{(\mathrm{ho})} = \hbar\,\omega_{\mathrm{ho}}\left(n+\frac{1}{2}\right) \tag{1.29}$$

The total number of bound states for a quantum harmonic oscillator is infinite, which is not physical for an finite-depth optical lattice. Therefore it has to be reduced to the number of states with energy $E_n \leq 0$. The maximum motional state number then reads

$$n_{\mathrm{max}}^{(\mathrm{ho})} = \left\lfloor\frac{U_0}{\hbar\,\omega_{\mathrm{ho}}} - \frac{1}{2}\right\rfloor, \tag{1.30}$$

where $\lfloor . \rfloor$ denotes the floor operator. The harmonic oscillator ansatz is a good approximation for deep lattices and small motional state numbers n.

1.4.2 Anharmonicities

As we will see in chapter 3 and 4 from our experimental results, due to non-perfect cooling, as well as fast transport sequences the atoms populate higher motional states and they, especially in the case of low trap depths, will therefore experience the anharmonicities of our optical lattice. The harmonic approximation then breaks down, which demands for a more exact description of possible atomic states.

Mathieu equation

The static Schrödinger equation for the one-dimensional potential,

$$\left(\frac{p^2}{2\,M} - U_0\,\cos^2\left[k_{\mathrm{dt}}\,(x-x_0)\right]\right)\psi_n(x) = E_n\,\psi_n(x), \tag{1.31}$$

with momentum operator $p = -\mathrm{i}\,\hbar\,\partial_x$ and $n \in \mathbb{N}^{\geq 0}$ numbering the motional states, can be brought into the form of the Mathieu differential equation [47]

$$\boxed{\partial_\eta^2\,\psi_n(\eta) + \left[a_n - 2\,q\,\cos(2\,\eta)\right]\psi_n(\eta) = 0}\,. \tag{1.32}$$

Here I substituted $\eta = k_{\mathrm{dt}}\,(x-x_0) + \pi/2$ and defined

$$a_n = \frac{E_n + U_0/2}{E_{\mathrm{rec}}}, \qquad q = \frac{U_0}{4\,E_{\mathrm{rec}}}\,. \tag{1.33}$$

This equation is well studied in the literature [48, 49] and for fixed q has countably infinite number of solutions. In the case that the coefficients a_n take on characteristic values $a_r(q)$ or $b_r(q)$, labeled by $r \in \mathbb{R}^{\geq 0}$, the solutions are periodic[1], with period π or 2π in the variable η, and can be described

[1] The integral values of r have to be restricted to $r \geq 0$ for solutions, which are even in η and to $r \geq 1$ for solutions being odd.

by the associated special functions – the odd sine elliptical $\mathrm{se}_r(q;\,\eta)$ and the even cosine elliptical $\mathrm{ce}_r(q;\,\eta)$ functions [Q]. Due to the anharmonicity of the lattice potential, the flatness of the Bloch energy bands is lifted and the eigenstates $\varphi_{n,\,k}$ labeled by band index $n \in \mathbb{N}^{\geq 0}$ and quasimomentum $k \in \mathbb{R} \cap [-\pi/a_{\mathrm{dt}}, +\pi/a_{\mathrm{dt}})$ are double degenerate and their energies read

$$E_{n,\,k} = E_{\mathrm{rec}}\, a^{\star}_{r(n,\,k)}(q) - \frac{U_0}{2} \tag{1.34}$$

with q as defined above. The Bloch eigenstates then can be written as

$$\varphi_{n,\,k}(x) = \mathrm{e}^{-\mathrm{i}\,k\,(x-x_0)}\,[\mathrm{ce}_r(q;\,\eta) + \mathrm{i}\,\mathrm{sgn}(r)\,\mathrm{se}_r(q;\,\eta)]|_{\eta = k_{\mathrm{dt}}\,(x-x_0)+\pi/2}\,, \tag{1.35}$$

where one can relate the real valued index of the characteristic Mathieu coefficient r to band index n and quasimomentum k by

$$r(n,\,k) = \begin{cases} k/k_{\mathrm{dt}} + \mathrm{sgn}(k)\,n & ,\, n \text{ even} \\ k/k_{\mathrm{dt}} - \mathrm{sgn}(k)\,(n+1) & ,\, n \text{ odd} \end{cases}. \tag{1.36}$$

The Wannier states can be constructed using equation (1.24).

The characteristic Mathieu coefficients and the associated periodic solutions can be accessed e. g. by the built-in functions of the numerical computing software MATHEMATICA [50].

Fast numerical approach

Under the consideration of the missing built-in support for the Mathieu coefficients in MATLAB [51] – the numerical computing and experimental control software of our choice – and that an own implementation based on the work of Alhargan [52] lacked on stability, in the following I will solve the problem of finding the eigenstates of the anharmonic lattice potential with a more direct approach and numerically diagonalize the Hamiltonian on a grid. By supposing periodic boundary conditions on a grid of 512 points in between $x = x_0 - a_{\mathrm{dt}}/2$ to $x_0 + a_{\mathrm{dt}}/2$, the Hamiltonian can be diagonalized in the fraction of a second on a standard consumer desktop computer.

Characteristics

When comparing the solutions of the harmonic approximation to the exact ones solving the anharmonic, sinusoidal potential, we can confirm that for deep lattices viewing the optical lattice as a quantum harmonic oscillator is a good approximation. In optical lattices with lower trap depths, e. g. $U_0 = 25\,\mu\mathrm{K}$, see figure 1.6, however the harmonic approximation breaks down fast. While eigenenergies and motional states are predicted in good accordance with the exact solutions for low band indices, the exact solution differs extremely for higher excited states, where the spacing of the energy levels becomes non-equidistant and the atoms start to feel the anharmonicities of the potential.

1.4.3 Radial motion

Considering just the radial atomic motion ($x = x_0$), the transverse Gaussian-shaped potential can be again approximated in first order as a harmonic oscillator:

$$U(\rho) = -U_0 \mathrm{e}^{-2\rho^2/w_{\mathrm{dt}}^2} = -U_0 + \frac{1}{2} M \omega_\rho^2 \rho^2 + \mathcal{O}(\rho)^4\,. \tag{1.37}$$

Here the radial trap frequency $\omega_\rho = 2\pi\nu_\rho$ is given by

$$\boxed{\omega_\rho = \sqrt{\frac{4\,U_0}{M\,w_{\mathrm{dt}}^2}}}\,, \tag{1.38}$$

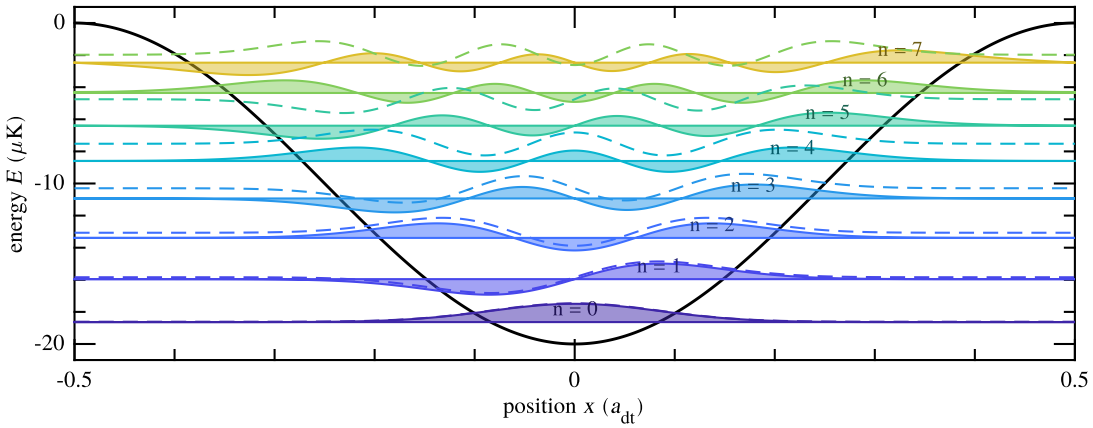

Fig. 1.6: Motional states and corresponding eigenenergies of the one-dimensional lattice potential. The real valued Wannier states (colored, filled) in the one-dimensional sinusoidal potential (black, solid) are shown offset by their respective eigenenergy. Given a trap depth of $U_0 = 20\,\mu\text{K}$, seven motional states are trapped by the optical lattice. The probability density of the Wannier ground state (dark purple, solid, $n = 0$) is in good accordance to the harmonic approximation (dark purple, dashed), but differs strongly for highly excited states. Likewise, the eigenenergies of the bound states in the sinusoidal potential differ from the equidistant spaced harmonic oscillator energies especially for the highly excited states. The eigenstates of the anharmonic potential (solid) were derived from the periodic solutions to the Mathieu differential equation, as well as calculated by numerically diagonalizing the corresponding Hamiltonian on a grid of 512 points with periodic boundary conditions. Due to their nearly perfect accordance, only the numerically obtained solutions are shown. The energies and eigenstates of the harmonic approximation are given by equation (1.28) and (1.29).

which makes the radial energy spacing about two orders of magnitude smaller compared to the longitudial trap,

$$\frac{\omega_\rho}{\omega_{\text{ho}}} = \frac{\sqrt{2}}{2\pi}\frac{\lambda_{\text{dt}}}{w_{\text{dt}}} \approx \frac{1}{87}\,. \tag{1.39}$$

Experimental techniques to further confine the atoms in the radial direction, as well as cooling them to the radial ground state, were applied successfully in the past [14]. Here a donut-shaped, red-detuned dipole trap creates a repulsive potential, which further decreases the radial trap frequency and the atoms are cooled using a pair of Raman beams resonant on the $n_\rho \rightarrow n_\rho - 1$ sideband, which removes motional quanta in the radial direction. Due to the good agreement between the first experimental results of this thesis and the one-dimensional theoretical description, we concluded that the radial confinement is sufficient for our considerations and did not employed these techniques. In the following I will therefore neglect the radial motion of the atom.

1.5 Compensating the dipole trap crosstalk

As we saw in section 1.2, qubit state $|{\downarrow}\rangle$ experiences the potentials created from both the σ^+- and σ^--polarized light field. Assume that we want to transport the atoms along the trajectory

$$x_0^{\uparrow}(t),\; U_0^{\uparrow}(t),\; x_0^{\downarrow}(t),\; U_0^{\downarrow}(t)\,. \tag{1.40}$$

If one would simply modulate the phases and intensities of the two polarized lattice beams such that the optical transport trajectory of the σ^+-polarized lattice perfectly follows the desired $\uparrow$ ramp and the σ^--polarized lattice the desired $\downarrow$ ramp, atoms in state $|{\uparrow}\rangle$ will experience the lattice potential imprinted on the σ^+-polarized dipole trap, but state $|{\downarrow}\rangle$ will experience a crosstalk between the two $\sigma^\pm$-polarized lattices.

However we can solve the problem by adjusting the control parameters of the σ^--polarized lattice. Since equation (1.20) can not be solved analytically for x_0^- and U_0^-, as shown in appendix A.2, we

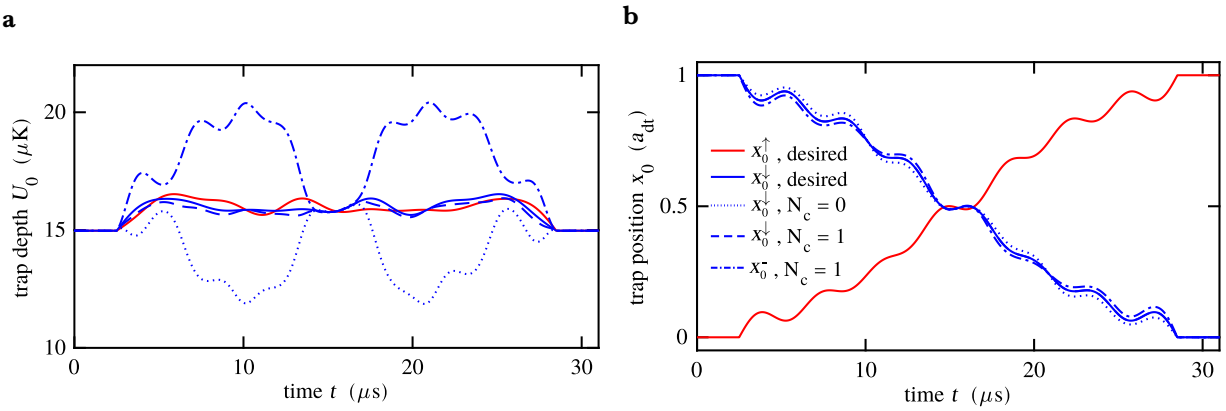

Fig. 1.7: Dipole trap crosstalk compensation for an atomic transport ramp, which brings together the two spin states by transporting them in opposite directions by one lattice site each. Both trap depth $U_0^{\mathcal{S}}$ (figure (a)) and position $x_0^{\mathcal{S}}$ (figure (b)) for $\mathcal{S} = \uparrow, \downarrow$ are varied along trajectories calculated from optimal control theory (solid), which would, if directly applied optically, result in a strong dipole trap crosstalk ($N_c = 0$, dotted). Already after one compensation repetition ($N_c = 1$), following the procedure explained in section 1.5, the effective atomic transport ramp (dashed) resembles more or less the desired ramp. The therefore necessary input ramp $r^-(t)$ (dash-dotted) shows just a small deviation in the trap position, but a strong change for the trajectory of the trap depth. The atomic transport ramps for more than one compensation repetition N_c are not shown, since they overlap perfectly with the desired ramps. The final optical transport ramp establishes a (simulated) transport fidelity of 98 % (see chapter 4 for details).

rearrange equation (1.20) and then solve the set of coupled equations numerically by taking (1.40) as an initial guess and iteratively evaluating:

$$\boxed{\begin{aligned} U_0^- &= \frac{1}{7}\left\{\sqrt{\left(8\,U_0^{\downarrow}\right)^2 - U_0^{+2}\sin^2\left[2k_{dt}(x_0^+ - x_0^-)\right]} - U_0^+\cos\left[2k_{dt}(x_0^+ - x_0^-)\right]\right\} \\ x_0^- &= x_0^{\downarrow} + \frac{1}{2k_{dt}}\arcsin\left\{\frac{U_0^+\sin\left[2k_{dt}(x_0^{\downarrow} - x_0^+)\right]}{7U_0^-}\right\} \end{aligned}} \tag{1.41}$$

The solution converges quite fast after only a few number of repetitions, denoted by $N_c \geq 0$, as shown exemplary in figure 1.7.

Chapter 2

Feedback control

Feedback control describes the methods for controlling a parameter of a dynamical system by a controller which obtains feedback of the current state of the system.

Although control feedback control applications appear since ancient history, its real origin lies in the industrial revolution with the demand for controlling new sources of power and new machines [53]. One simple example is the centrifugal governor, which has been used to control the speed of windmills and steam engines by converting the rotational movement into a control force which depends on the engine speed. Today the majority of feedback control is managed by converting the feedback into an electronic signal and providing response to the system by use of a proportional, integral, derivative (PID) controller circuit [53].

2.1 Steering position and depth of optical lattices

As illustrated in figure 1.3 and figure 2.2 the polarization synthesis and intensity modulation of our lattice beams is achieved via acousto-optical modulators (AOM) combined with an electronic lock loop based on analog PID controllers. A more in-depth explanation of the electronics used for feedback control is given in section 2.2. Here, a short introduction to the AOM-based intensity and phase modulation should be given. Figure 2.1a shows the basic working principle of an AOM.

2.1.1 AOM-based phase and intensity modulation

The AOMs used in the experiment consist of optically transparent Tellurium-Dioxide (TeO_2) crystals, which are connected to piezo-driven ultrasonic transducers. The piezo elements, driven by a radio signal at a operating frequency of $\nu_{\mathrm{aom}} \approx 80\,\mathrm{MHz}$, introduce sound waves at the material specific sound velocity ($\mathrm{v_s} \approx 4.2\,\mathrm{mm\,s^{-1}}$), which propagate as phonons through the crystal. Since the acoustic strain introduces changes in the mass density of the medium inside the crystal, the optical index of refraction is modulated periodically,

$$n(\boldsymbol{x}, t) = n_0 - \Delta n \cos\left(\Omega_{\mathrm{s}}\, t - \boldsymbol{K}_{\mathrm{s}} \cdot \boldsymbol{x}\right), \tag{2.1}$$

where $\boldsymbol{K}_{\mathrm{s}} = 2\pi/\Lambda_{\mathrm{s}}\, \hat{\boldsymbol{e}}_y$ with $\Lambda_{\mathrm{s}} = \mathrm{v_s}/\nu_{\mathrm{aom}}$ is the acoustic wavevector and n_0 the index of refraction in the absence of light [55]. The amplitude of the modulation is given by

$$\Delta n = \sqrt{\frac{1}{2}\, \mathscr{M}\, I_{\mathrm{s}}}\,, \tag{2.2}$$

where I_{s} is the acoustic intensity and $\mathscr{M}$ is a material specific constant, determining the strength of the interaction. This is the elasto-optical effect, first proposed by Raman and Nath in 1935 [56].

The periodic modulation of the refraction index provide a moving phase grating on which a laser beam propagating through the crystal gets refracted and similarly to an optical diffraction grating,

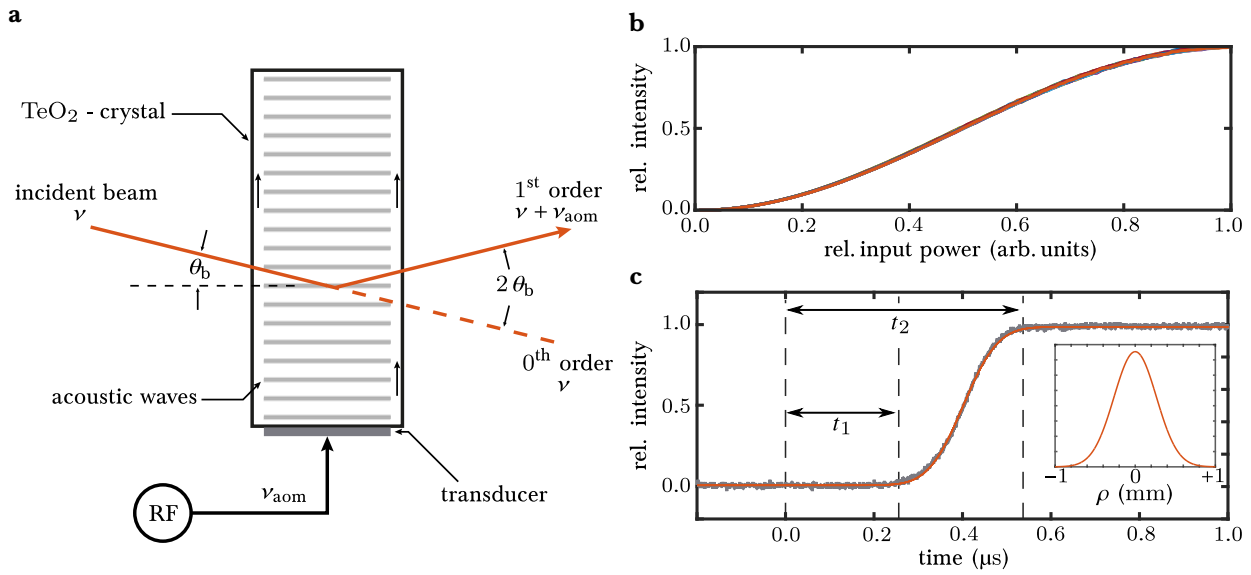

Fig. 2.1: Working principle of the AOM based intensity and phase modulation (b). The incoming light is passed through an optically transparent Tellurium-Dioxide (TeO_2) crystal which is connected to a piezo-driven ultrasonic transducer driven by a radio signal (RF) at a center frequency of $\nu_{\mathrm{aom}} = 80\,\mathrm{MHz}$. The first order diffraction of the incident optical beam at two times the Bragg angle, $2\,\theta_{\mathrm{b}}$, is frequency shifted by the AOM frequency, $\nu \rightarrow \nu + \nu_{\mathrm{aom}}$, and its intensity is modulated dependent on the acoustic RF power, as illustrated in (b). Due to the Gaussian shaped beam profile (inset) the AOM response to a step in acoustic power (c) has the form of an Gaussian error function. The dead time of the AOM, t_1, the time before any response of the AOM and its rise time, t_2, to the reach the 99 % mark of the relative optical intensity depends on the distance between optical beam and transducer, the sound velocity inside the crystal and the size of the optical beam. In this well optimized setup we obtain $t_1 \approx 0.25\,\mu\mathrm{s}$ and $t_2 \approx 0.5\,\mu\mathrm{s}$. The figures and numbers are adapted from [54].

multiple orders of high intensity can be observed. The most interesting case is the so-called Bragg diffraction regime, where the length of the crystal is larger than the acousto-optical interaction length. Given frequency ν and wavevector $\boldsymbol{k} = 2\pi/\lambda \left[\cos(\theta_{\mathrm{in}})\,\hat{\boldsymbol{e}}_x - \sin(\theta_{\mathrm{in}})\,\hat{\boldsymbol{e}}_y\right]$ with $\lambda = c/\nu$ of the incoming laser light, energy and momentum conservation of the elastic collision requires the refracted photons to be shifted both in frequency and momentum:

$$\nu_{\mathrm{r}} = \nu \pm m\,\nu_{\mathrm{aom}}\,, \qquad \boldsymbol{k}_{\mathrm{r}} = \boldsymbol{k} \pm m\,\boldsymbol{K}_{\mathrm{s}}\,. \tag{2.3}$$

where + corresponds to the annihilation and − to the creation of m phonons. In the case of the optical beam absorbing one lattice vibration, this leads to the typical angle relation for diffraction on an optical grating:

$$\Lambda_{\mathrm{s}} \left[\sin(\theta_{\mathrm{in}}) + \sin(\theta_{\mathrm{out}})\right] = \lambda/n\,, \tag{2.4}$$

where the optical wavelengths of the incoming and outgoing beam are approximated to be the same. If the incident light enters the AOM at the Bragg angle, $\theta_{\mathrm{B}} = \arcsin\left[\lambda_0/(2\,\Lambda_a)\right]$, both in- and outgoing angle are the same, $\theta_{\mathrm{in}} = \theta_{\mathrm{out}} = \theta_{\mathrm{B}}$, and the beam is deflected by $2\,\theta_{\mathrm{B}}$.

Assuming the electric field of optical beams to be plane waves, one can show, that in the Bragg limit nearly all outgoing intensity can be found in the principal refraction order [57]. A more rigorous analysis [55] considering the Bragg diffraction as a light-scattering process under the Born approximation shows, that the electric field intensity reflectance at the Bragg angle is given by

$$\mathcal{R} = \sin^2\left(\frac{\pi\,L}{\lambda}\,\Delta n\right) \tag{2.5}$$

where L is width of the AOM crystal. By inserting equation (2.2) the diffracted light intensity, $I_{\mathrm{r}} =$

$\mathscr{R}\, I_{\text{in}}$, can be written as

$$\boxed{I_{\text{r}} = I_{\text{in}} \sin^2\left(\frac{\pi}{2}\sqrt{\frac{I_{\text{a}}}{I_{\text{sat}}}}\right)}, \tag{2.6}$$

where I_{in} is the incoming optical intensity and $I_{\text{sat}} = \lambda^2/(2\,\mathscr{M}\,L^2)$ is defined to be the saturation intensity of AOM. Taking into account that the optical intensity is proportional to the square of the input voltage U_{s} to the transducer, in the RF power regime below the saturation intensity, the first order diffraction intensity is therefore monotonically increasing with the input voltage and shows even a linear behavior for I_{a} around $\sim I_{\text{sat}}/2$, as shown in figure 2.1b. We use this point for effectively modulating the intensity and therefore the trap depth of the optical lattice.

The principle of optical phase modulation can be understood from the formula for the energy conservation (2.3) taking into account that the optical frequency is much larger than the one of the AOM radio signal, $\nu \gg \nu_{\text{aom}}$. In the slowly-varying time limit, this makes the frequency shift introduced by the acoustic optical interaction, $\nu \to \nu + \nu_{\text{aom}}$, be acting as an effective phase shift

$$\boxed{\Delta\phi = 2\pi \left\langle \nu_{\text{aom}}\, t \right\rangle_t}. \tag{2.7}$$

By changing the AOM driving frequency the phase of the optical lattice beams can be varied and controlled. In the experimental setup, each lattice arm is phase modulated by an independent AOM, which imprints a well defined phase onto the beam and allows to control the relative phase between the two optical lattice beams precisely. This however demands for an active stabilization, since e. g.small temperature fluctuations, which might change the relative length of the two optical beam paths, lead to phase shifts. As shown in the next sections using an optical phase lock loop (PLL) the dependence on the input light intensity on the phase control can be suppressed by electronically rectifying the measured beat signal used for phase detection by a limiting amplifier.

System response

Since the AOM is the main part of the phase and intensity lock loop and its system response is therefore worth to characterize. A measurement of the optical response exposed to a step in acoustic power is shown in figure 2.1c. The dead time t_1 arises directly from the speed of sound inside the AOM crystal and the position of the optical beam, since the acoustic wave front needs a finite time to travel the distance from the piezo transducer to the location of the optical beam. As we can see, the rising edge of the RF signal power applied at time $t = 0$ has almost immediate effect on the AOM response which results in a dead time of about $0.25\,\mu\text{s}$ in a well optimized setup. The rise time and the slope of the rise depends mainly on the sound velocity inside the crystal and the size and profile of the optical beam. Since we work with well collimated Gaussian beams, the resulting step response has the form of a Gaussian error function – a convolution of the hard Heaviside-like step with the Gaussian beam profile, which therefore directly determines the shape of the impulse response. The finite response time imposes an upper limit to the bandwidth of our system, which we will discuss in section 2.2.3 and provide a solution in the outlook, section O.2.

2.2 Digital feedback control

As illustrated in figure 1.3, we employ AOMs to control both intensity and phase of the optical lattice beams. A fraction of the laser beam is directly extracted for the intensity feedback loop using a coated pickup plate and an ultrafast photodiode – with a bandwidth of $10\,\text{GHz}$ – picks up the beating signal between the phase controlled lattice beams and a reference signal, which is in phase with the counter-propagating linear polarized lattice beam.

2.2.1 Electronic setup

The electronic setup for the σ^+ polarized optical lattice arm is illustrated in figure 2.2.

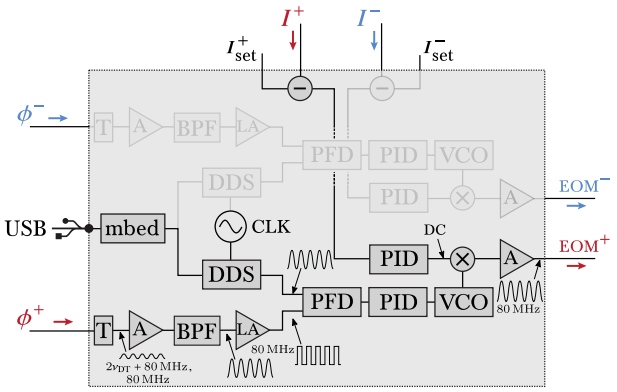

Fig. 2.2: Digital phase and intensity lock electronics. The circuit represents the black box labeled "Phase- & Intensity-Lock" in figure 1.3. For simplicity only the lock for the σ^+-polarized lattice is highlighted. The signal of a fast photodiode measuring the intensity of the beam is compared with a set value, which is controlled using a vector generator, and then fed to a proportional–integral–derivative (PID) controller which actively controls the acoustic power in the AOM using an amplifier (A). The optical beat signal detected by a ultrafast photodiode contains both the sum $2\nu_{\mathrm{dt}} + \nu_{\mathrm{aom}}$ and difference frequency $\nu_{\mathrm{aom}} = 80\,\mathrm{MHz}$ of the optical beams. After getting DC biased (T), amplified (A) and band-pass filtered to extract just the difference frequency, the signal is digitized by a limiting amplifier (LA) and compared to a 80 MHz reference signal generated by a direct digital synthesizer (DDS). The phase difference detected by a phase frequency discriminator (PFD) is then fed to another analog PID lock, which actively controls the frequency using a voltage controlled oscillator (VCO). The two DDS boards are referenced to the same 10 MHz clock and controlled by an embedded microcontroller (mbed) connected to the laboratory computer system.

The beat signal of the σ^+-polarized lattice beam with the reference gives information about the phase ϕ^+ of the associated lattice and contains both the sum and difference of the two frequencies. After adjusting the DC bias point using a bias tee (T) and amplification (A) the signal is bandpass filtered (BPF) and then sent through a limiting amplifier (LA), which minimizes output power variations and provides a constant output over a wide input dynamic range. This digitization makes the phase lock mostly independent of the intensity lock by suppressing any cross-coupling induced intensity fluctuations and also controlled ramping of the trap depth. A small crosstalk between the amplitude and phase lock can not be prevented, however this has no significant impact on the atoms [14]. The phase of the beat signal is then compared with a RF reference signal from a direct digital synthesizer (DDS) at 80 MHz using a digital phase-frequency discriminator (PFD). The PFD – a design developed by Prevedelli [58] – creates a voltage which is, within a limited range, proportional to the phase difference between the two signals. An analog PID controller driving a voltage-controlled oscillator (VCO) creates a RF control signal fed to the corresponding AOM controlling the optical beam. This ensures DDS and beat signal to be locked in phase. Both DDS are referenced to the same 400 MHz clock signal (CLK) and are controlled via an embedded microcontroller (mbed), which is connected to a computer via USB. By mixing the RF signal with the DC signal from a PID lock box, which compares the measured beam intensity (I^+) with a set value (I^+_{set}), both intensity and phase of the optical beam can be controlled.

2.2.2 Compensation of system response

In a simple model, our optical electronic phase and amplitude lock loop can be described by linear response theory [59]. A linear and time-invariant (LTI) system is fully described by the so-called transfer function $H(s)$ in frequency domain. One usually defines the complex frequency $s = 2\pi\,\mathrm{i}\,f + \rho$, where the purely imaginary part describes oscillations with f the standard frequency and the real part ρ describes damping and attenuation. This definition of the frequency relates every function in

frequency domain $F(s)$ with the respective function in time domain $f(t)$ by the Laplace transform

$$F(s) = \mathscr{L}\left[f(t)\right](s) = \int_0^\infty \mathrm{d}t\, f(t)\, \mathrm{e}^{-s\,t}\,, \tag{2.8}$$

instead of the usual Fourier transformation. The transfer function is the ratio of the output signal $Y(s)$ to an input $X(s)$, $H(s) = Y(s)/X(s)$, and in general can be written as the ratio of two polynomials in s,

$$H(s) = \frac{(s-\zeta_1)\,(s-\zeta_2)\,\cdots\,(s-\zeta_{N_\mathrm{z}})}{(s-\rho_1)\,(s-\rho_2)\,\cdots\,(s-\rho_{N_\mathrm{p}})}\,, \tag{2.9}$$

where we here have chosen the factorized representation, where N_p and N_z determine the number of poles, $\{\rho_i\}$, and zeros, $\{\eta_i\}$, of the transfer function respectively.

In time domain our system can be described by the impulse response function, $g(t)$, which describes the system's response to a delta-like signal, $x(t) = \delta(t)$, applied to the set-point of the respective PID controller. Using the fact that for a delta-like input $X(s) = \mathscr{L}\left[\delta(t)\right](s) = 1$ and that $Y(s) = H(s)\,X(s)$, the impulse response function can be directly related to the system transfer function via the inverse Laplace transformation:

$$g(t) = \left.y(t)\right|_{x(t)=\delta(t)} = \left.\mathscr{L}^{-1}\left[Y(s)\right](t)\right|_{X(s)=1} = \mathscr{L}^{-1}\left[H(s)\right](t)\,. \tag{2.10}$$

The impulse response as well as the transfer function therefore fully describes the system and allows to relate any arbitrary input signal $x(t)$ to an output $y(t)$. Since delta-like signals are hard to realize experimentally, the impulse response can also be deduced from the system's response $b(t)$ to a Heaviside-like step input, $x(t) = \Theta(t)$ with $\Theta(t) = 0$ if $t < 0$ and $\Theta(t) = 1$ if $z \geq 0$. The impulse response function is then directly given by its derivative

$$\frac{\partial}{\partial\, t}\, b(t) = \left.\frac{\partial}{\partial\, t}\, y(t)\right|_{x(t)=\Theta(t)} = \left.\mathscr{L}^{-1}\left[s\,H(s)\,X(s)\right](t)\right|_{X(s)=1/s} = \mathscr{L}^{-1}\left[H(s)\right](t) = g(t) \tag{2.11}$$

where we used the relation $\mathscr{L}\left[\partial_t\, y(t)\right](s) = s\,Y(s) - y(0)$ for any continuous $y(t)$, $\partial_t\, y(t)$ of exponential order. Under the assumptions of linear response theory, the system's response function should furthermore scale linearly with the step height.

To determine the impulse response function from a step response measurement, one needs to measure both the intensity and phase of the two optical lattice arms individually. Measuring the response to a step in the amplitude is straight forward to perform, while measuring the phases (positions) of the two lattices is a bit more complicated. However, as we will show in the next paragraph, the possibility to fully synthesize the polarization of one of the lattice beams gives us a versatile tool for measuring the phase via a quadrature measurement.

Quadrature phase measurement

While measuring the intensity of the optical lattices is done really easily, e.g. by picking up a small portion of the polarization synthesized beams and applying only the desired amplitude ramp to the lattice hardware, measuring the optical phase is not so straight forward.

However, by flipping in a linear polarizer with polarization $\hat{\boldsymbol{\epsilon}}_\mathrm{p}$ into the path of the polarization synthesized lattice beam, one can pickup the magnitude of the electric field projection onto this polarization,

$$\begin{aligned} I_\mathrm{p}(\phi^+, \phi^-) &= \frac{1}{2} c\epsilon_0 \left|\boldsymbol{E}_\mathrm{synth}(x,t)\cdot\hat{\boldsymbol{\epsilon}}_\mathrm{p}\right|^2 \\ &= \frac{1}{2} c\epsilon_0 \left|\left(E_0^+\,\hat{\boldsymbol{\epsilon}}_+\,\mathrm{e}^{\mathrm{i}\phi^+} + E_0^-\,\hat{\boldsymbol{\epsilon}}_-\,\mathrm{e}^{\mathrm{i}\phi^-}\right)\mathrm{e}^{-\mathrm{i}(k_\mathrm{DT}x+\omega t)}\cdot\hat{\boldsymbol{\epsilon}}_\mathrm{p}\right|^2 \\ &= I_0\left[\cos\left(\phi^+ - \phi^-\right) + 1\right], \end{aligned} \tag{2.12}$$

where we assumed the two arms to be at same intensity, $I_0 = \frac{1}{2} c \epsilon_0 E_0^{\pm 2}$. Assume that we want to measure the optical phase of the σ^+-polarized lattice, $\phi^+(t)$. By setting $\phi^- = 0$ and $\phi^- = \pi/2$ we obtain the two quadrature components

$$C(\phi^+) = I_\mathrm{p}(\phi^+, 0) = I_0 \left[\cos(\phi^+) + 1\right], \qquad S(\phi^+) = I_\mathrm{p}(\phi^+, \pi/2) = I_0 \left[\sin(\phi^+) + 1\right]. \tag{2.13}$$

When measuring minima and maxima of these signals, $C_\mathrm{min} = \min_{0 \le \phi^+ \le 2\pi} C(\phi^+)$ the phase can then be extracted from

$$\phi^+(t) = \mathrm{unwrap}\left[\arctan\left(\frac{\bar{S}(t)}{\bar{C}(t)}\right)\right] - 2\phi_\mathrm{p} \tag{2.14}$$

where ϕ_p is known, e. g. from the C_min- and C_max-measurements, and the normalized quadrature components are given by

$$\bar{C}(t) = 2\left(\frac{C(\phi^+(t)) - C_\mathrm{min}}{C_\mathrm{max} - C_\mathrm{min}}\right) - 1, \qquad \bar{S}(t) = 2\left(\frac{S(\phi^+(t)) - S_\mathrm{min}}{S_\mathrm{max} - S_\mathrm{min}}\right) - 1, \tag{2.15}$$

which also compensates for constant photodiode offsets. The unwrap function ensures that phases $\phi^+ + 2\phi_\mathrm{p}$, which exceed 2π are not wrapped to the interval defined by the choice of the arctan's principal branch, and does this by looking for 2π multiples that allow smooth increases of the phase.

The same procedure can be applied for measuring $\phi^-(t)$ by ramping $\phi^-(t)$ in time while fixing $\phi^+ = 0$ and $\phi^+ = \pi/2$ respectively.

Determining the system's impulse response

First we apply a Heaviside step signal to either the setpoint of the PID controlling the intensity or to the phase control of the DDS and measure the optical system's response $b(t)$ as well as the digital signal, which triggers the respective phase or amplitude change. For better accuracy the optical signal is averaged 100 times, which is way more than sufficient. After normalization, the input step function and the system's response are fitted using the Matlab Control System toolbox [60]. Good fitting results could be obtained by providing a precise initial guess for the delay between trigger signal and system's response obtained from a simple least-square fit of a Heaviside step function to both trigger signal and step response. While a direct calculation of the system's impulse response via numerical differentiation is really sensitive to noise, the Control System toolbox allows to first fit the step response measurement using a model for the system's transfer function via the position of poles and zeros of the polynomial representation, equation (2.9), which then gives access to the impulse response function by Laplace transformation. By scanning different combinations of number of poles N_p and zeros N_p the best fit model is selected.

The measured step response and calculated impulse response functions for the σ_--polarized lattice arm are shown in figure 2.3. While the shown step response for the phase lock has been optimized for a fast rise time by tuning the proportional, integral and differential gain of the PID controller, the intensity lock exemplary shows the case of a non-optimized, slow rise and settling time. Since we experienced small changes in the system's response over time, the step responses were optimized on a regular basis and the determination of the impulse response was automatized and repeated on a weakly routine.

Deconvolution with impulse response function

We will now make the approximation that the system behaves linearly. Using linear response theory, we can write the systems phase response $\phi(t)$ to an input signal $\phi_\mathrm{in}(t)$ as the convolution with the impulse response function $g^{(\phi)}(t)$

$$\phi(t) = \left[g^{(\phi)} * \phi_\mathrm{in}\right](t) = \int_{-\infty}^{+\infty} \mathrm{d}\tau \; g^{(\phi)}(\tau)\, \phi_\mathrm{in}(t - \tau). \tag{2.16}$$

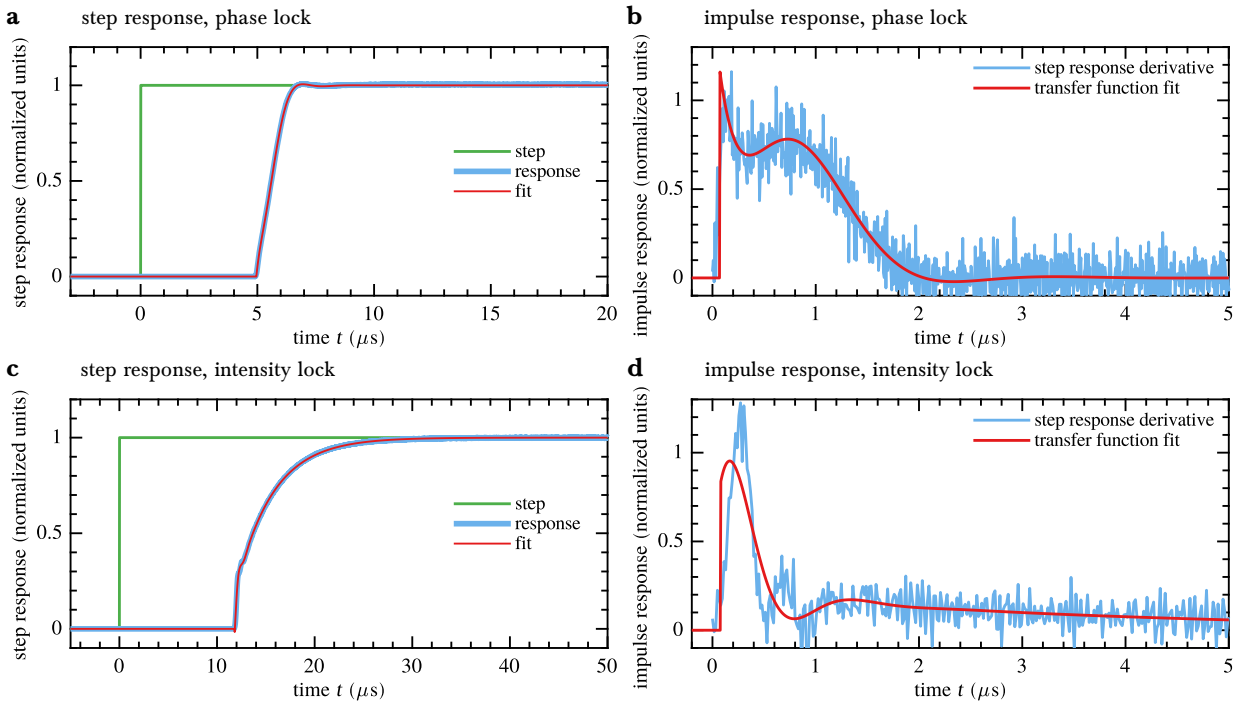

Fig. 2.3: Step and impulse response measurement for both intensity and phase control of the semi-digital phase and intensity lock loop shown exemplary for the σ_--polarized lattice arm. While the impulse response functions (b), (d) are shifted in time for better comparison, the step response measurements (a), (c) also show the delay time τ_d between the trigger and the system's response. The impulse response extracted from the direct differentiation of the step response measurement (right, light-blue) is really sensitive to the noise, but shows a more gentle increase at the beginning. The fit of the step response is in good accordance to the data and reproduces the most dominant features in the associated impulse response function. The best fit could be obtained for a transfer function with $N_\mathrm{p} = 3$ poles and $N_\mathrm{z} = 3$ zeros.

Fourier transforming both sides and with use of the convolution theorem, we can phrase this as follows

$$\phi(t) = \mathcal{F}^{-1}\left\{G^{(\phi)}(\nu) \cdot \Phi^{\pm}_{\mathrm{in}}(\nu)\right\}(t) = \mathcal{F}^{-1}\left\{\mathcal{F}\left[g^{(\phi)}(t)\right](\nu) \cdot \mathcal{F}[\phi_{\mathrm{in}}(t)](\nu)\right\}(t), \tag{2.17}$$

where the Fourier and inverse Fourier transform are given by $\mathcal{F}[f(t)](\nu) = \frac{1}{\sqrt{2\pi}} \int_{-\infty}^{\infty} \mathrm{d}t\ f(t)\, \mathrm{e}^{-2\pi \mathrm{i}\nu t}$ and $\mathcal{F}^{-1}[F(\nu)](t) = \frac{1}{\sqrt{2\pi}} \int_{-\infty}^{\infty} \mathrm{d}t\ F(\nu)\, \mathrm{e}^{2\pi \mathrm{i}\nu t}$. The impulse response function $g^{(\phi)}$ can be extracted from a step response measurement – exemplary shown in figure 2.3 – and is therefore known. This allows inverting equation (2.17) and writing the required input signal $\phi^{\pm}_{\mathrm{in}}$ as the deconvolution of the desired response ϕ with the impulse response function $g^{(\phi)}(t)$, which corresponds to a division of the associated signals in frequency domain:

$$\phi^{\pm}_{\mathrm{in}}(t) = \mathcal{D}\left\{\phi(t);\ g^{(\phi)}(t)\right\} = \mathcal{F}^{-1}\left[\frac{\Phi(\nu)}{G^{(\phi)}(\nu)}\right](t)\,. \tag{2.18}$$

The same holds true for controlling the beam intensity via an input signal $I_{\mathrm{in}}(t)$ with impulse response function $g^{(I)}(t)$. An example for the deconvolution of a linear phase ramp is shown in figure 2.4.

Improving the deconvolution

To increase the interpolation in frequency domain and to ensure that the signals Fourier transform represents a linear instead of circular convolution, the signal is zero-padded before deconvolution. Left and right padding of 20 µs worked more than sufficient for the transport sequence under consideration.

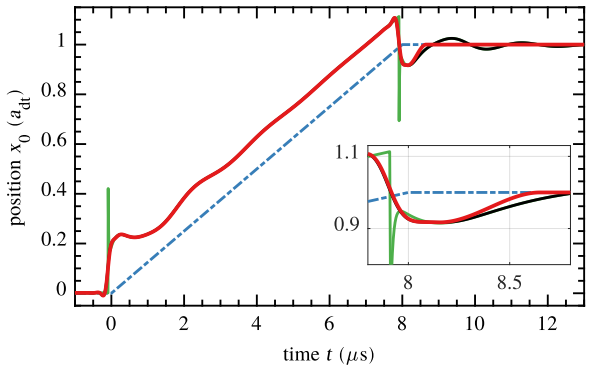

Fig. 2.4: Deconvolution with impulse response function shown exemplary for a linear transport sequence of $T = 8\,\mu s$. Deconvolving the desired position / phase ramp $x_0(t) = a_{dt}\,\phi(t)\,/\,(2\pi)$ (blue, dash-dotted) without low-pass filtering the deconvolved signal in frequency domain leads to high frequencies and strong spikes at the initial and final kink of the linear ramp (green, solid). The deconvolved and low-pass filtered signal (black, solid) still strongly exceeds the desired ramp but is much smoother. Oscillations of the lock set point after the transport can be compressed by correcting the end points of the deconvolution using a spline interpolation (red, solid) – here applied in the time interval of $0.5\,\mu s$ after the transport. To fully reach agreement between optical and desired ramp, iterative optical error correction, as shown in figure 2.5, has to be applied.

As illustrated in figure 2.4 we additionally apply a third order Butterworth low-pass filter to the deconvolution of desired control signal $\Phi^{\pm}(\nu)$ and impulse response $G^{\phi}(\nu)$, so that

$$\phi_{in}^{\pm}(t) = \mathcal{D}\left\{\phi(t);\ g^{(\phi)}(t)\right\} = \mathcal{F}^{-1}\left[\frac{1}{\sqrt{1+\left(\frac{\nu}{\nu_c}\right)^6}}\frac{\Phi(\nu)}{G^{(\phi)}(\nu)}\right](t) \tag{2.19}$$

By choosing an appropriate cutoff frequency ν_c unwanted high-frequency components like aliases of the numerical deconvolution method are strongly suppressed, while the important features of the desired transport ramps do not change.

Furthermore we developed an algorithm to correct the end points of the input phase and amplitude trajectories after deconvolution using a cubic spline interpolation. This suppresses oscillations of the set points of phase and amplitude after transport by smoothly bringing down the set points to the desired value, so that for instance $x_0(t) = d$ and $U_0(t) = U_0(0)$ for all $t \geq T$, as illustrated in figure 2.4.

Iterative optical error correction

The idea to fully describe a system by its impulse response function in time or its transfer function in frequency domain relies on the assumption that the system is linear. As we can detect experimentally, the step response for both amplitude and phase varies for different heights of the step, which is a clear indicator for the nonlinearity of the system. When taking the impulse response for a fixed, medium sized step height, the deconvolution scheme presented in the previous paragraph therefore can only compensate for small deviations between input signal and desired behavior of the optical lattice beams. To compensate for the non-linearity in our system and to fully make optical phase and amplitude to behave as requested, an iterative error correction scheme can be applied.

The desired control signal $\phi(t)$ – we again consider controlling the phase exemplary – is deconvolved with the systems impulse response function $g^{(\phi)(t)}$ and applied as $\phi_{in}(t)$ to the lattice hardware. From an optical measurement of the signal (using the quadrature technique), the deviation between measured and desired signal, $\delta\phi(t) = \phi(t) - \phi_{meas}(t)$, is obtained and judged by calculating the ratio between

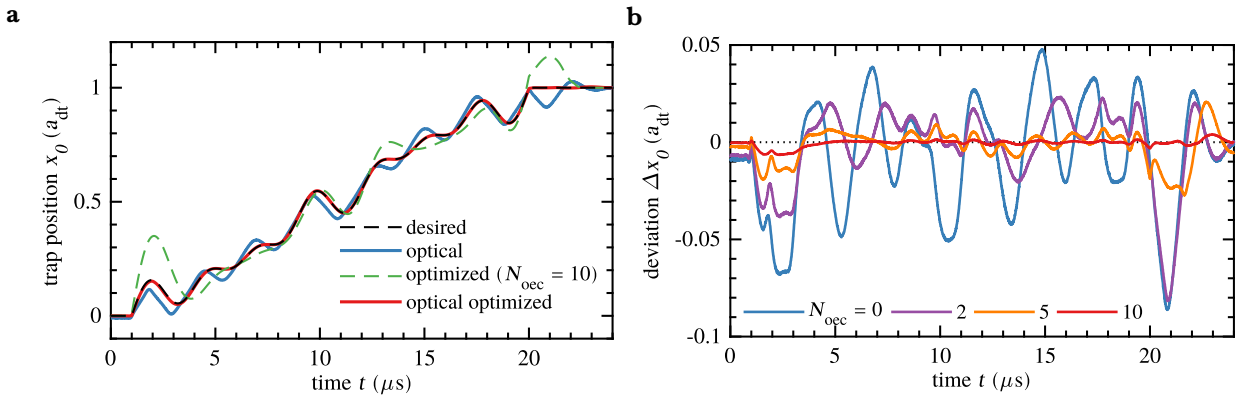

Fig. 2.5: Iterative optical error correction for an (optimal control) transport ramp. Both the ramp (a) and the deviation (b) between measured and desired position ramp are shown. All measured transport ramps (solid) are obtained by the quadrature phase detection technique, averaged over five measurement repetitions. When the desired ramp (black, dashed) is just deconvoled by the system's impulse response function ($N_{oec} = 0$), the optically measured trap position (blue, solid) deviates especially in the regions of strong slopes. The deviation can be strongly reduced by the iterative optical feedback compensation with $p_{gain} = 0.5$ and $N_{dev} = 20$ Fourier components. After $N_{oec} = 10$ feedback corrections, the final transport ramp (green, dashed), which is applied deconvoled as a phase ramp to the lattice hardware, leads to an optical signal (red, solid), which is really close to the desired transport ramp. The absolute deviation between optically measured and desired transport ramp then falls below 1 % of the lattice spacing. This increases the coefficient of determination from $R^2 = 99.92\,\%$ to above $R^2 > 99.99\,\%$.

residual sum and total sum of squares[1],

$$R^2 = 1 - \frac{\sum_{i=1}^{N} \phi(t_i) - \phi_{meas}(t_i)}{\sum_{i=1}^{N} \phi(t_i) - \langle \phi(t) \rangle_t}, \tag{2.20}$$

where N is the number of data samples and $\langle . \rangle_t$ denotes the time average.

The deviation is then fitted with a sum of Fourier components

$$\delta\phi_{fit}(t) = \Theta(T - t_f - t) \sum_{n=1}^{N_{dev}} c_n \sin\left(\frac{\pi\, n}{T}\right) \tag{2.21}$$

using a least-square regression, where T is the (fixed) duration of the transport ramp. The free fit parameters are given by the coefficients c_n and a final hold time t_f, in which the function is allowed to vanish completely. Consistently good fit results could be achieved by estimating a good initial guess for the final hold time in advance and by taking $N_{dev} = 20$ Fourier components.

The fitted deviation is then added to the desired phase ramp $\phi^{\pm}(t)$ with gain $p_{gain} = 0.5$, deconvolved with the system response and the resulting signal,

$$\phi_{in} = \mathcal{D}\{\phi + p_{gain}\, \delta\phi_{fit}(t)\,;\; g^{\phi}(t)\} \tag{2.22}$$

is then applied to the lattice hardware.

This optical error correction is repeated $N_{oec} = 5$ to 10 times to achieve good agreement between the optically measured and desired transport ramp. Unexpected responses from the lock electronics and inexact least-square fits can be successfully dealt with by monitoring the R^2 coefficient and repeating iterations with decreased $p_{gain} \to 0.9 \cdot p_{gain}$ for too strong deviations. An illustrating example of the working principle of the iterative optical feedback correction is shown in figure 2.5.

[1] Also known as the R^2 coefficient of determination in linear regression applications.

2.2.3 Performance and limitations

If we apply the optical error correction in combination with the deconvolution scheme the input ramps strongly overdrive the system. This response of the system however stays reproducible and controlled. The new scheme therefore is a big improvement and extension of the electro-optical phase and intensity lock loop now allowing high-fidelity controlled transport sequences with transport times below $8\,\mu s$, which was already experimentally verified and never reached before. The modulation bandwidth measured from the response function of the polarization synthesizer for both the phase and intensity servo loop [26] lies at about $800\,\mathrm{kHz}$. Together with the high-precision optical phase lock loop, where a polarization purity of $99.99\,\%$ provides us with a rms uncertainty about the relative position between the two standing waves of the polarization-synthesized optical lattice of just about $1.2\,\text{Å}$ [26], the complete setup promises to allow high-precision and ultrafast transport sequences.

Slope constraint

As we will see in chapter 4 optimal control transport sequences in reasonably deep lattices can demand for strong and fast driving of the lattice position. We observe that the main limiting factor for this is the maximum phase slope the combined system of phase frequency discriminator and PID lock can resolve and react to. From empirical observations we obtain

$$\boxed{|\dot{\phi}(t)| \leq \dot{\phi}_{\max} = 0.838\,\mathrm{rad}\,\mu\mathrm{s}^{-1}}\,. \tag{2.23}$$

We will however deal with this limitation by using a constraint optimization algorithm for calculating the optimal control sequences as introduced in section 4.3.1.

Chapter 3

Microwave cooling and state detection

As indicated before, we want the atoms to be cooled to the ground state of the optical lattice. After molasses cooling, the trapped atoms follow a Boltzmann distribution with a temperature of approximate $125\,\mu\mathrm{K}$, which results in a ground state population of less than $10\,\%$ in our deep imagining lattice ($U_0 = 370\,\mu\mathrm{K} \times k_B$). We therefore need to employ an additional cooling technique.

Cooling of atomic motion states is generally achieved by employing absorption and emission cycles of a resonant or near resonant radiation, mostly at optical frequencies. For free particles laser Doppler cooling for instance can iterative reduce the atomic momentum by recoil processes. The motion of atoms trapped in e. g. optical dipole potentials is described by the occupation of it's motional states $|n\rangle$. While trapped atoms can also be approximately described by it's momentum, when the radiation does not spectroscopically resolve the motional states $|n\rangle$, transitions in the resolved-sideband regime – which allow reducing the motional state number by driving e. g. transitions on the first red sideband $|n\rangle \rightarrow |n-1\rangle$ – do not induce an atomic recoil due to the Mössbauer effect. Cooling techniques in optical lattices mostly rely on two-photon Raman sideband transitions, which connect two hyperfine over an intermediate excited state [61–63]. As we will see in the following, state-dependent optical lattices provides us with a unique trick, which also allows the use of sideband resolved Microwave radiation [64, 65], which directly connects our two qubit states and which we will employ for cooling and also for state detection.

3.1 Microwave cooling

The coupling between microwave radiation and the effective atomic two-level quantum system consisting of our selected hyperfine groundstates, $|F = 3,\, m_F = 3\rangle$ and $|F = 4,\, m_F = 4\rangle$, can be described as the interaction between the atomic dipole moment $\boldsymbol{\mu}$ and the magnetic field $\boldsymbol{B}_{\mathrm{mw}}$ induced by the microwave:

$$H_{\mathrm{mw}} = \boldsymbol{\mu} \cdot \boldsymbol{B}_{\mathrm{mw}} \tag{3.1}$$

Taking into account also the motional states, the transition matrix element for the sideband transition $|F,\, m_F;\, n\rangle \rightarrow |F',\, m_F';\, m\rangle$ is given by

$$\langle F',\, m_F';\, m|H_{\mathrm{mw}}|F,\, m_F;\, n\rangle = \langle F',\, m_F'|\boldsymbol{\mu} \cdot \boldsymbol{B}_{\mathrm{mw}}|F,\, m_F\rangle \, \langle m_{F',\, m_F'}|n_{F,\, m_F}\rangle \,, \tag{3.2}$$

where the first part just depends on the coupling between the hyperfine levels and not on the form of the motional states.

Since the linewidth of the electromagnetic transitions, $|F,\, m_F;\, n\rangle \rightarrow |F',\, m_F';\, m\rangle$, between motional states is much smaller than the energetic spacing, $|E_n - E_m|$, between the motional states itselves, microwave radiation can resolve any of these sideband transitions. However, as noted in equation (1.25), distinct motional eigenstates of the optical lattice potential are in general orthogonal to each other, which makes coupling them via microwave radiation impossible, since we can neglect any momentum transfer by the microwave photons, whose wavevector amplitude is about five orders of magnitude smaller compared to optical photons used for Raman transitions.

Non-vanishing Franck-Condon factor

However if we shift the lattices apart by some distance Δx, the motional state overlap from equation (3.2) can be expressed by applying the displacement operator, $\mathrm{T}_{\Delta x} = \mathrm{e}^{\mathrm{i}\, p\, \Delta x}$, to one of the states. The motional state overlap integral, called the Franck-Condon factor in e. g. molecular spectroscopy, illustrated in figure 3.1b, then becomes non-zero and reads:

$$\begin{aligned} F_{m\to n} &\equiv \langle n_{F',\, m'_F} | m_{F,\, m_F} \rangle \\ &\approx \langle n | \mathrm{T}_{\Delta x} | m \rangle = \int \mathrm{d}x\; \psi_n^{\star}(x)\, \psi_m(x - \Delta x), \end{aligned} \tag{3.3}$$

where $\psi_n(x) = \psi_{n,\,i}$ is the Wannier state with vibrational state number n, localized at the respective lattice site i. Shifting the lattices apart, therefore lifts the orthogonality and enables motional state transfer using a direct microwave pulse. This not only allows driving transitions on the carrier, where the motional quantum number does not change ($\delta = n - m = 0$), but also on sideband resonances with $\delta > 0$ on the blue ($E_n - E_m > 0$) and $\delta < 0$ on the red ($E_n - E_m < 0$) side of the carrier. Their frequency spacing is approximately given by multiples of the longitudinal harmonic oscillator frequency ω_{x}.

Here we approximated the trap depths and therefore the corresponding eigenstates of the shifted lattice potentials to be equal. Due to the dipole trap crosstalk, when shifting the two lattices apart, the optical dipole potential acting on $|\downarrow\rangle$ sees also some slight change in the trap depth, which in theory also lifts the orthogonality of the motional states, but for our experimental parameters it can be completely neglected.

Cooling cycle

To cool the atoms to the ground state of the lattice potential, after loading them from the MOT, we first prepare them in the $|\uparrow\rangle$ qubit state by means of optical pumping. By driving a microwave transition resonant on the $|\uparrow, n\rangle \to |\downarrow, n-1\rangle$ sideband, we can lower the motional state number by one. Therefore the lattice is displaced by $\Delta x = 17\,\mathrm{nm}$, which experimentally was determined to maximize the transition amplitude for the cooling sideband transition.

To make the microwave radiation not just inducing a cycle between the two motional states, but to really cool the atoms over time, we complete the cooling cycle, by repumping the atoms from the $|\downarrow\rangle$ to the $|\uparrow\rangle$ ground state after state transfer, without changing their motional state number. This is done by transferring the atoms on the $^2\mathrm{S}_{1/2}$, $F = 3$, $m_F = 3 \to {}^2\mathrm{S}_{1/2}$, $F = F$, $m_F = F$ transition using near-resonant, σ^+-polarized light, from which they then decay to $F = 4$, $m_F = 4$ ground state. This then successively lowers the motional state number and since the motional ground state of the σ^+-polarized optical lattice potential is a dark state of the cooling cycle, the atoms are accumulated in the $|\uparrow, n = 0\rangle$ ground state.

The cooling sequence is illustrated in figure 3.1a and more information about the experimental setup can be found in [14, 65, 66]

3.2 Sideband resolved microwave spectroscopy

To judge the cooling efficiency and measure the temperature of the motional state distribution after cooling, we can effectively measure the transmission of microwave radiation resonant on the red and blue sideband transition. For that, atoms which are prepared in the $|\uparrow\rangle$ are transfered to $|\downarrow\rangle$ by microwave radiation at frequency ν, for which the two lattices are again shifted apart by $\Delta x = 17\,\mathrm{nm}$. Experimentally we use Gaussian microwave pulses, whose spectral width is much smaller than the sideband frequency displacement and therefore allows to neglect any induced contribution for transitions on the carrier or higher sidebands. After the microwave transfer all atoms remaining in the $F = 4$ ground state are pushed out by a strong laser beam near-resonant on the $^2\mathrm{S}_{1/2}$, $F = 4 \to {}^2\mathrm{P}_{3/2}$, $F = 5$ transition. The radiation pressure, which originates from the photon scattering, is σ^+-polarized and due to the hyperfine selection rules does only effect atoms in the $|\uparrow\rangle$ spin state, while the

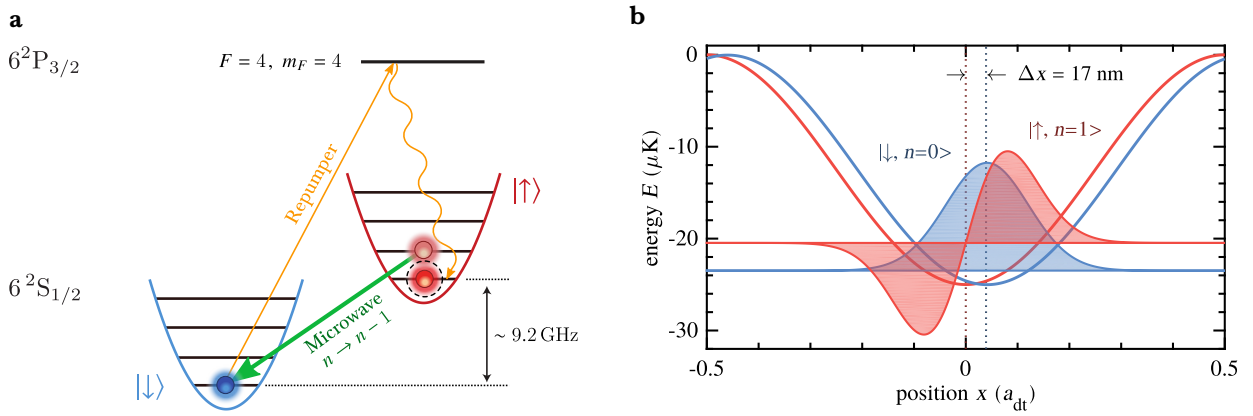

Fig. 3.1: Experimental sequence (a) and underlying principle (b) of the microwave cooling technique. By shifting the potentials with respect to each other, the Franck-Condon factor, determined by the overlap integral of distinct motional states in the two spin states, becomes non-zero, which allows to drive a microwave transition resonant on the $|\uparrow, n\rangle \rightarrow |\downarrow, n-1\rangle$ sideband transition. By repumping the atoms to the $|\uparrow\rangle$ ground state, this successively lowers the motional state number and cools the atoms to the ground state of the σ^+-polarized optical lattice potential, which is a dark state of the cooling cycle. Figure (b) shows the displaced lattice potentials, as well as the motional states corresponding to the transition shown in (a) offset by their eigenenergies. We only show the real part of the motional eigenstates, since we chose their phases so that the imaginary part vanishes.

$|\downarrow\rangle$ is a dark state. The pushout efficiency is about 99 %, which is mainly restricted due to off-resonant photon scattering on the $^2S_{1/2}$, $F = 3 \rightarrow {}^2P_{3/2}$, $F = 4$ transition. The number of remaining atoms is detected via fluorescence imaging by collecting the scattered photons of the atoms with an EMCCD camera[1].

A direct indication for the cooling efficiency is the peak height at the first blue sideband, which we also call cooling transition. When the atoms are hot and therefore populate motional states with $n > 0$, microwave radiation resonant to the $|\uparrow, n\rangle \rightarrow |\downarrow, n-1\rangle$ transition can induce cooling, but if the atoms are cooled to the ground state, they are located in a dark state and the cooling sideband disappears. This phenomena is illustrated in figure 3.2, showing a sideband spectrum before and after microwave cooling, taken at a trap depth of $U_0 = 80\,\mu K$. We here scanned the microwave frequency around the atomic carrier resonance of $\omega_0/(2\pi) \sim 9.2\,GHz$ and restricted the scan to the first blue and red sideband, which are displaced by approximately the harmonic trap frequency relative to the carrier. The Gaussian shaped envelope directly results from the spectral shape of the microwave pulses, which are normal distributed as well.

3.2.1 Thermal distributions in quadratic potentials

After molasses and microwave cooling we can approximate the atoms to follow a thermal distribution. The population of the vibrational levels is then described by a Boltzmann distribution with temperature $\mathcal{T}$ and the probability to find an atom in motional state $|n\rangle$ reads

$$p_n = \frac{\exp\left(-\frac{E_n}{k_B \mathcal{T}}\right)}{\sum_m \exp\left(-\frac{E_m}{k_B \mathcal{T}}\right)}. \tag{3.4}$$

If we consider the limit of deep lattices, where the harmonic approximation, equation (1.29), holds true, then one can calculate the ground state population p_0 directly from the measured sideband

[1] All experimentally determined atom numbers are always normalized to a reference measurement – the pure survival. We therefore run the exact same exerimental sequence without employing any pushouts and measure the fraction of atoms remaining in the optical lattice. This allows taking into account all non-intended processes which lead to the loss of atoms such as noice-induced heating over time or decoherence.

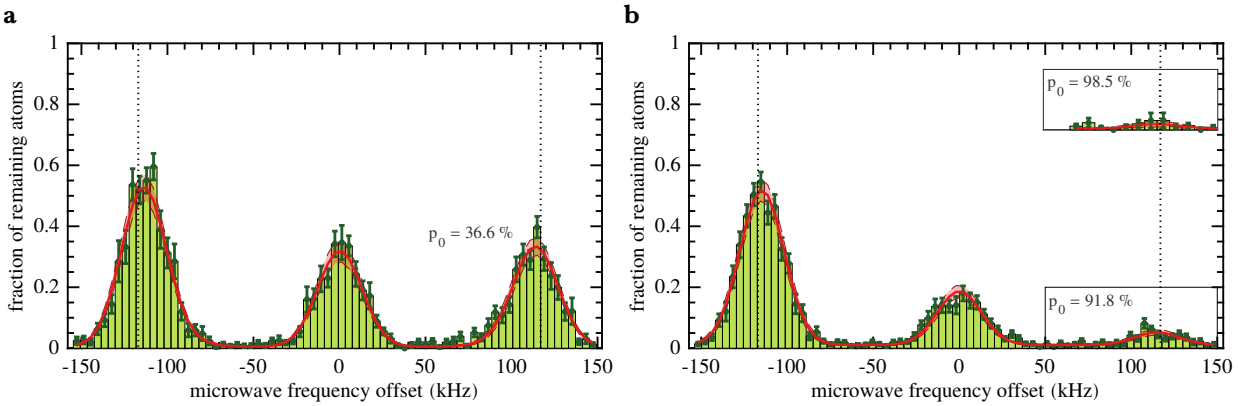

Fig. 3.2: Sideband-resolved microwave spectra (green) before (a) and after microwave sideband cooling (b). The height of the first blue sideband – the cooling sideband – decreases for cooled atoms. A least-square fit (red) given by equation (3.10) gives information about the motional state population of the atoms as well as the trap depth. Assuming a thermal Boltzmann distribution the associated temperatures are calculated to be $\mathcal{T} = (11.7 \pm 1.3)\,\mu\mathrm{K}$ before and $\mathcal{T} = (2.2 \pm 0.1)\,\mu\mathrm{K}$ after microwave cooling. With a trap depth of $U_0 = (82 \pm 1)\,\mu\mathrm{K}$ – the depth seen both by spin $|\uparrow\rangle$ and $|\downarrow\rangle$ in the perfectly overlapped, unshifted lattice – we can numerically relate these temperatures to $p_0 = (36.7 \pm 3.6)\,\%$ for the uncooled and $p_0 = (91.9 \pm 1.0)\,\%$ for the cooled case. The harmonic oscillator frequencies – the trapping frequency – corresponding to the estimated trap depth reads $\nu_x = (123.6 \pm 0.9)\,\mathrm{kHz}$ and its position is indicated by a black dashed line. The inset in (b) shows the cooling sideband after optimization of the microwave cooling parameters, which results in a ground state population of about 99 %. The red shaded areas around the adapted curves indicate the 1σ confidence intervals of the corresponding fits, which hold 68 % of the values drawn from a normal distribution.

height. Following [67], the areas Σ_{+1} and Σ_{-1} under the first blue and red sideband respectively are directly proportional to the corresponding cross sections of the transition and the fraction of atoms in the ground state regardless of the microwave induced line shape is then given by

$$p_0 = 1 - \frac{\Sigma_{-1}}{\Sigma_{+1}}\,. \tag{3.5}$$

While this method works quite nicely for deeper lattices [14], the relatively low trap frequency and spectrally broad microwave pulses in the microwave spectrum, shown in figure 3.2, make it hard to mark out the two areas corresponding to the blue and red sideband precisely. By fitting the three peaks with a superposition of Gaussian curves, we obtain $p_0 \approx (36.6 \pm 0.5)\,\%$ for the uncooled and $p_0 \approx (91.8 \pm 0.8)\,\%$ for the cooled case.

3.2.2 Anharmonicities and decoherence

The harmonic approximation only holds true under the assumption of deep lattices. Atoms in shallow optical lattices, which are subject to fast transport sequences will however feel the anharmonicities of the lattice potential.

The main effect of the anharmonicity of the trapping potential onto the microwave sideband spectroscopy results from the non-equidistant spacing of energy levels, which results in a shift of the transition frequencies for excited atoms. Given a general resonant microwave transition on the mth sideband, $|F, m_F; n\rangle \rightarrow |F', m_F'; n + m\rangle$, not only the associated Franck Condon factor, $F_{n\rightarrow n+m}$, and therefore the transition probability, but also the transition frequency, $\nu_{n\rightarrow n+m}$, itself changes when considering different initial motional states n. This effect is illustrated in figure 3.3 for a trap depth of $25\,\mu\mathrm{K}$. While the carrier position nearly stays constant, the sideband positions shift with increasing motional state n drastically closer to the carrier. For precise measurement of the atoms temperature, as well as the trap depth we need to consider these effects.

Furthermore we observe even for microwave pulses well optimized close to a π-condition a reduction of the sideband and carrier heights, which can be explained by the duration of Gaussian shaped

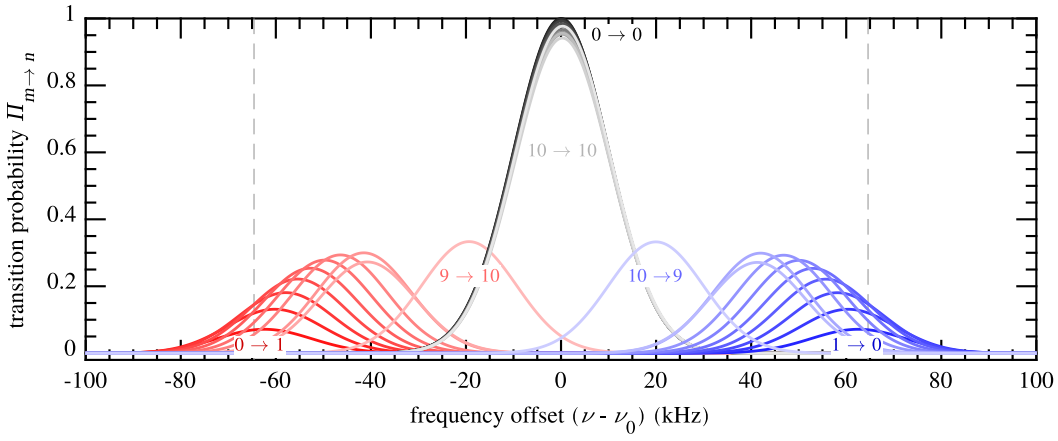

Fig. 3.3: Shift of the transition frequencies due to the anharmonicity and crosstalk of the two lattice potentials illustrated for driving the transitions with a Gaussian microwave pulse at an trap depth of $U_0 = 25\,\mu\text{K}$. We show the heating $n \to n+1$ (red), the cooling $n \to n-1$ (blue) and the carrier transition $n \to n$ (black) for the 11 bounded states $|n\rangle$, $n \in [0, 10]$. The transition probabilities are given by equation (3.11) with $p_n = \delta_n$ chosen to be peaked at the associated motional state level and Rabi frequency and pulse length chosen such, that the microwave pulse satisfies a π-condition on the carrier. The dashed, gray line indicates the trap frequency $\pm\nu_x$ given by the harmonic approximation, equation (1.27).

microwave pulses and the limited coherence time. The two main limiting factors are environmental induced spin-flips, which are described by the population relaxation time T_1 and pure dephasing of the spin coherences described by the coherence relaxation time T_2. In the current state of the setup we are limited to $T_1 \approx 90\,\text{ms}$ and $T_2 \approx 51\,\mu\text{s}$, which can can be obtained experimentally by measuring the fraction of remaining atoms after letting initially prepared atoms relax and pushing out the $F = 4$ states and by means of Ramsey spectroscopy [14]. A comprehensive list of the physical origin of decoherence in our experimental apparatus can be found in [46].

Effective two-level system

Here we consider the two states coupled by each individual transition as an effective two-level system, which allows to describe the problem by Rabi oscillations. The interaction between ground state $|g\rangle$ and excited state $|e\rangle$ with a near resonant microwave pulse with (angular) frequency $\omega = 2\,\pi\,\nu$ and Rabi frequency $\Omega(t)$ is governed by the time-dependent Hamiltonian

$$H_{\text{eff}}(t) = \hbar\,\omega_0\,\sigma^\dagger\,\sigma + \frac{\hbar\,\Omega(t)}{2}\left(\sigma\,\mathrm{e}^{\mathrm{i}\,\omega\,t} + \sigma^\dagger\,\mathrm{e}^{-\mathrm{i}\,\omega\,t}\right), \tag{3.6}$$

where $\hbar\,\omega_0$ is the energy spacing between the two atomic states and $\sigma = |g\rangle\langle e|$. In the rotating frame the Hamiltonian – given by the unitary transformation $H_{\text{eff}} \to R(t)\,H_{\text{eff}}\,R(t)^\dagger + \mathrm{i}\,\hbar\,(\partial_t\,R(t))\,R(t)^\dagger$ with $R(t) = \mathrm{e}^{\mathrm{i}\,\omega\,t|e\rangle\langle e|}$ – can be simplified by the rotating wave approximation and then reads

$$\tilde{H}_{\text{eff}}(t) = \hbar\,\Delta\,|e\rangle\langle e| + \frac{\hbar\,\Omega(t)}{2}\left(\sigma + \sigma^\dagger\right), \tag{3.7}$$

where $\Delta = \omega - \omega_0$ is the detuning between microwave field and atomic resonance.

Since we are interested in the effect of the decoherence induced non-unitary time evolution we have to describe the quantum state in terms of a density matrix $\rho(t)$. The time evolution is then given by the corresponding Liouville-von Neumann equation

$$\boxed{\frac{\partial}{\partial\,t}\,\tilde{\rho}(t) = -\frac{\mathrm{i}}{\hbar}\left[\tilde{H}_{\text{eff}},\,\tilde{\rho}(t)\right] + \Gamma\,\mathcal{L}[\sigma]\,\{\tilde{\rho}(t)\} + \gamma_\perp\,\mathcal{L}[\sigma_z]\,\{\tilde{\rho}(t)\}} \tag{3.8}$$

with the longitudinal decay rate $\Gamma = 1/T_1$ and transversal decay rate $\gamma_\perp = 1/T_1 - 1/(2T_2)$. Here $\tilde{\rho}(t) = R(t)\,\rho(t)$ is the density operator in the rotating frame, $\sigma_z = |e\rangle\langle e| - |g\rangle\langle g|$ and the Lindblad superoperator $\mathscr{L}$ is defined as

$$\mathscr{L}[A]\{\rho\} = A\,\rho\,A^\dagger - \frac{1}{2}\left(A^\dagger A\,\rho + \rho\,A^\dagger A\right). \tag{3.9}$$

We will now assume that an atom is prepared in state $|F,\, m_F\rangle$ occupying the associated motional state $|m\rangle$ and ask for the transfer probability to the other hyperfine state $|F',\, m'_F\rangle$ and motional state $|m\rangle$ induced by a microwave pulse $\Omega(t)$ at frequency ν, $\Pi_{m\to n}(\nu)$. We obtain this number by numerically integrating the differential equation (3.8) for given pulse shape $\Omega(t)$ and detuning $\Delta = 2\pi(\nu - \nu_{m\to n})$ with the atoms initially prepared in state $|g\rangle = |F,\, m_F;\, m\rangle$ to state $|e\rangle = |F',\, m'_F;\, n\rangle$. Here $\nu_{n\to m}$ is the resonance frequency corresponding to the considered transition and the Rabi frequency is given by the transition matrix element, $\Omega_{m\to n}(t) = \langle F',\, m'_F;\, m\,|H_{\mathrm{mw}}(t)|\,F,\, m_F;\, n\rangle / \hbar$ and therefore proportional to the associated Franck Condon factor $F_{m\to n}$.

If we assume the initial motional states $|m\rangle$ to be occupied given a probability distribution p_m, the full sideband spectrum – the fraction S of transferred atoms after applying a microwave pulse at frequency ν – is then obtained by summing over all possible transitions $|m\rangle \to |m + i_{\mathrm{sb}}\rangle$ with $i_{\mathrm{sb}} \in \mathbb{Z}$:

$$\boxed{S(\nu) = \sum_{i_{\mathrm{sb}}} \sum_m p_m\,\Pi_{m\to m+i_{\mathrm{sb}}}(\nu)}, \tag{3.10}$$

where the sum $\sum_m$ runs over possible bound states which are allowed for the given transition.

In our experiment microwave sideband spectra are obtained using a Gaussian shaped microwave pulse, $\Omega(t) \propto \gamma(t) \equiv \exp\left[-t^2/(2\sigma_t^2)\right]$, which provides us – compared to the sinc^2 distribution associated to a square pulse – with a relatively small spectral width of the sidebands and therefore allows to resolve the different vibrational sidebands [65] even in shallow lattices. For fitting purposes numerically solving equation 3.8 repetitively is computationally very demanding. A simpler, phenomenological model can be obtained by replacing

$$\Pi_{m\to m+i_{\mathrm{sb}}}(\nu) = A\,\sin^2\left(\frac{\alpha}{2}\,\frac{F_{m\to m+i_{\mathrm{sb}}}}{F_{0\to 1}}\right)\exp\left[-\frac{(\nu - \nu_{m\to m+i_{\mathrm{sb}}})^2}{2\,\sigma_\nu^2}\right] + b \tag{3.11}$$

where A is a global amplitude which approximately resembles the effect of decoherence, b describes the noise floor and α determines the microwave pulse condition on the first blue sideband transition $|0\rangle \to |1\rangle$ generally optimized for $\alpha \approx 1$ which corresponds to a π rotation in the Bloch sphere.

If we assume that the population of the vibrational levels is Boltzmann distributed with temperature $\mathcal{T}$, a least-square fit using equation 3.10 gives us information about the trap depth, as well as the motional state distribution for the two microwave spectra shown in figure 3.2. Since we now take into account the anharmonicities, in comparison to the simple Gaussian fits as used in section 3.2.1, the fitted trap frequency is not exactly coinciding with the sideband position anymore but is slightly corrected to larger values. For the two spectra in figure 3.2 we obtain $\nu_x = (123.6 \pm 0.9)\,\mathrm{kHz}$. For shallower lattices this deviation increases further. From the spectrum after molasses cooling we obtain a temperature of $\mathcal{T} = (38.9 \pm 6.9)\,\mu\mathrm{K}$ corresponding to $p_0 = (13.8 \pm 2.2)\,\%$ ground state population while the spectrum after microwave cooling gives $\mathcal{T} = (1.8 \pm 0.1)\,\mu\mathrm{K}$ which corresponds to $p_0 = (92.8 \pm 1.9)\,\%$ ground state population. Well optimized microwave cooling sequence let us reach about $99\,\%$ ground state population, as illustrated in the inset in figure 3.2b.

Both the numerical solution of equation (3.8) as well as our empirical model also explain the reduced carrier height in the cooled spectrum. Due to the anharmoncity of the lattice potential the Franck Condon factor varies for the different carrier transitions $|n\rangle \to |n\rangle$. When the atom populates more the low energy levels, the effective Rabi frequency increases slightly and the atom experiences more than a π-rotation which then reduces the associated transition probability and therefore the carrier height.

3.2.3 Limitations

Both methods – the sideband fit taking into account the anharmonicities, as well as the ratio estimate based on the harmonic approximation – are reliable methods for obtaining the temperature and a rough measure for the ground state population when dealing with thermally distributed atomic ensembles in deep lattices and were used successively over years to judge for instance the microwave cooling efficiency. However, as the main indicator – the cooling sideband height – decreases with higher ground state population, it becomes more and more difficult to determine the ground state population to good accuracy. Additionally, taking a whole sideband spectrum takes time, and as we saw in the previous paragraph, restricting the spectroscopy to the peak of the cooling sideband is nearly impossible when considering shallow traps, where anharmonicities play a role. This makes the previous analysis routine nearly unusable, especially when considering excitations to arbitrary motional state populations, which we will experience in the context of fast atom transport, see chapter 4.

Although our group recently developed a method [68] to approximately determine the ground state population just from the heights of the first blue and red sideband by making assumptions about the motional state distribution and choosing appropriate fitting models, we will here employ an alternative approach, which will allow us to quantify the ground state population directly for arbitrary distributions of motional state populations in arbitrary shallow lattices. Furthermore it provides a simple way to extend the scheme to a full tomography of all motional states.

3.3 Motional state tomography

The basic idea for measuring the amount of ground state population is to remove all atoms except the ones that occupy the ground state. This can be done by first preparing the atoms in $|\uparrow\rangle$ qubit state, where the motional state distribution p_n can be arbitrary and transferring them to the $|\downarrow\rangle$ level by a fast rectangular microwave π-pulse at the carrier frequency. When applying the microwave pulse in the unshifted lattice, the transfer does not change the motional state population and experimentally reached efficiencies of about $97\,\%$ when using fast rectangular shaped microwave pulses [14]. After shifting the lattice apart, the combination of a high resolution Gaussian microwave pulse resonant on the $|\downarrow, n\rangle \rightarrow |\uparrow, n-1\rangle$ sideband transition, followed by a pushout of all the atoms in $F = 4$ effectively removes all atoms except the ones in the ground state $|\downarrow, n = 0\rangle$ as illustrated in figure 3.4a.

Due to the limited efficiency of the Gaussian microwave pulse, which also varies between the different motional states due to the anharmonicities of the lattice potential, not all atoms are transferred and the transition prefers specific motional state $|n\rangle$ for which the associated To increase and equalize the efficiencies for all motional states, both the Gaussian microwave transfer as well as the pushout can simply be repeated multiple times. Given N_{mst} combined microwave transfer and pushout repetitions, the efficiency for removing all excited atoms in motional state $|n\rangle$ is approximately given by

$$\mathscr{E}_n = 1 - (1 - \epsilon_n)^{N_{\mathrm{mst}}}, \tag{3.12}$$

where ϵ_n is the efficiency of a single application. This exponential scaling brings $\mathscr{E}_n$ close to 1 after just a few repetitions. A more careful analysis is presented in the following section. This detection scheme was first introduced in Belmechri et al. [65].

3.3.1 Spectroscopy of motional state distributions

We will consider the experimental cycle in terms of a rate equation considering just the transition probabilities of the different elements forming the whole sequence and thereby neglecting any of the accumulated quantum phases. The microwave transition probabilities however will be treated by the individual numerical integration of equation (3.8) which allows to consider the real quantum evolution including dephasing within the microwave cycles itself.

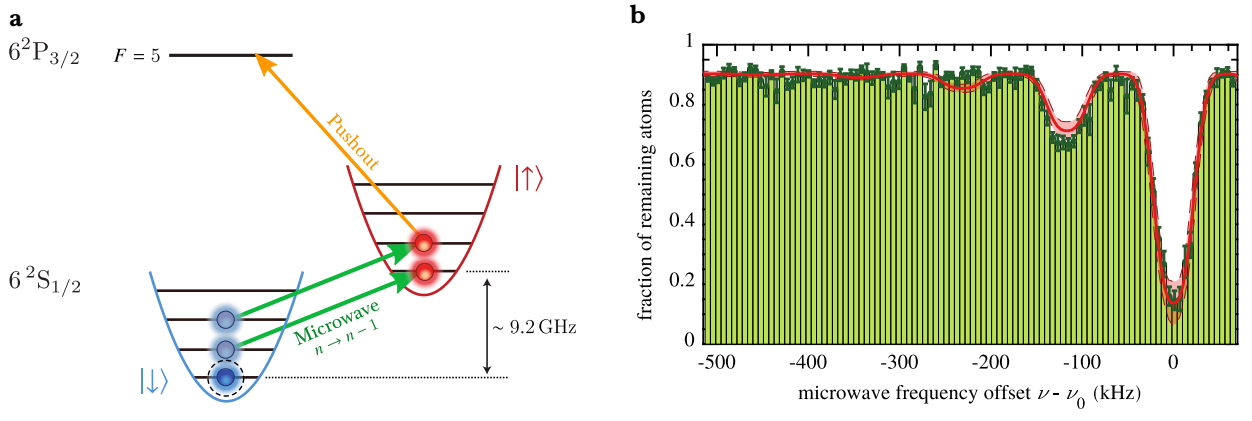

Fig. 3.4: Experimental scheme for the motional state tomography (a). After preparing the atoms in $|\downarrow\rangle$ a Gaussian shaped microwave pulse resonant with the i_{sb}-th red sideband transfers all atoms from state $|\downarrow, n\rangle$ with $n \geq i_{\mathrm{sb}}$ to $|\uparrow, n\rangle$ where the transferred atoms are then pushed out of the lattice. This scheme is repeated N_{mst} times to compensate for low and uneven microwave efficiencies. The fraction of remaining atoms is directly proportional to the cumulative sum of motional state populations $\sum_{n=0}^{i_{\mathrm{sb}}-1} p_n$, which can be identified from a spectrum, where the microwave frequency is swept over multiples of the trapping frequency. A fit of equation (3.17) to the carrier and first four red sidebands (red line) of the experimentally measured spectrum (b) for $N_{\mathrm{mst}} = 10$ repetitions assuming a thermal Boltzmann distribution gives a temperature of $\mathcal{T} = (4.0 \pm 0.2)\,\mu\mathrm{K}$. The red shaded area indicates the 3σ confidence interval associated to the fit.

We represent the initial atomic state populations as a vector

$$\boldsymbol{p}_{\mathrm{init}} = \sum_{\mathcal{S}=\uparrow,\downarrow} \sum_{n=0}^{n_{\mathrm{max}}} p_n^{(\mathcal{S})} |\mathcal{S}, n\rangle \equiv \left(p_0^{(\uparrow)}, p_0^{(\downarrow)}, p_1^{(\uparrow)}, p_1^{(\downarrow)}, \ldots p_{n_{\mathrm{max}}}^{(\uparrow)}, p_{n_{\mathrm{max}}}^{(\downarrow)}\right)^{\mathsf{T}} \tag{3.13}$$

with populations $p_0^{(\uparrow)} = 0$ and $0 \leq p_n^{(\downarrow)} \equiv p_n \leq 1$. The 1-norm of a given 'state' $\boldsymbol{p}$, $\|\boldsymbol{p}\|_1 \equiv \sum_{\mathcal{S}} \sum_n p_n^{(\mathcal{S})}$, provides us with the fraction of atoms relative to the initial state. This allows to phrase the individual elements of the detection sequence as matrices describing the transition from one population distribution to another. The pushout pulse then can be simplified written as the block diagonal transition matrix P with elements

$$\mathrm{P}_{m,n} = \begin{bmatrix} 1 - \epsilon_{\mathrm{push}}^{(\uparrow)} & 0 \\ 0 & 1 - \epsilon_{\mathrm{push}}^{(\downarrow)} \end{bmatrix} \tag{3.14}$$

where we assume that the pushout efficiency for atoms in $F = 4$ $\epsilon_{\mathrm{push}}^{(\uparrow)} \approx 1$ and the pushout efficiency for atoms in $F = 3$ and $\epsilon_{\mathrm{push}}^{(\downarrow)} \approx 0$. The microwave square pulse transfer as well as the Gaussian microwave pulse transitions can be approximated by adapting equation (3.11) for the respective pulse shape and relative lattice shift[1]. While the square pulse M_{square} is always performed at the fixed carrier frequency ν_0 (which only slightly changes for higher motional states), the Gaussian microwave transition matrix M_{gauss} depends on the scanned microwave frequency ν. For N_{mst} repetitions of the combined application of Gaussian microwave pulse at frequency ν and pushout, the fraction S of remaining atoms after the experimental sequence is then given by

$$S(\nu) = \left\| \left[\mathrm{P} \cdot \mathrm{M}_{\mathrm{gauss}}(\nu)\right]^{N_{\mathrm{mst}}} \cdot \mathrm{P} \cdot \mathrm{M}_{\mathrm{square}}(\nu_0) \cdot \boldsymbol{p} \right\|_1 . \tag{3.15}$$

The measured fraction of remaining atoms in the proximity of the red sideband positions $\nu \approx -i_{\mathrm{sb}}\,\nu_x$ with $i_{\mathrm{sb}} \in \mathbb{N}^{>0}$ for high N_{mst} is approximately given by the sum over all motional states $|n\rangle$ with

[1] The square pulse is always performed in the unshifted lattice, $\Delta x = 0$, to suppress any contributions from sideband transitions, while we the Gaussian microwave pulses for resolving the sidebands is always applied at the lattice shift of $\Delta x = 17\,\mathrm{nm}$.

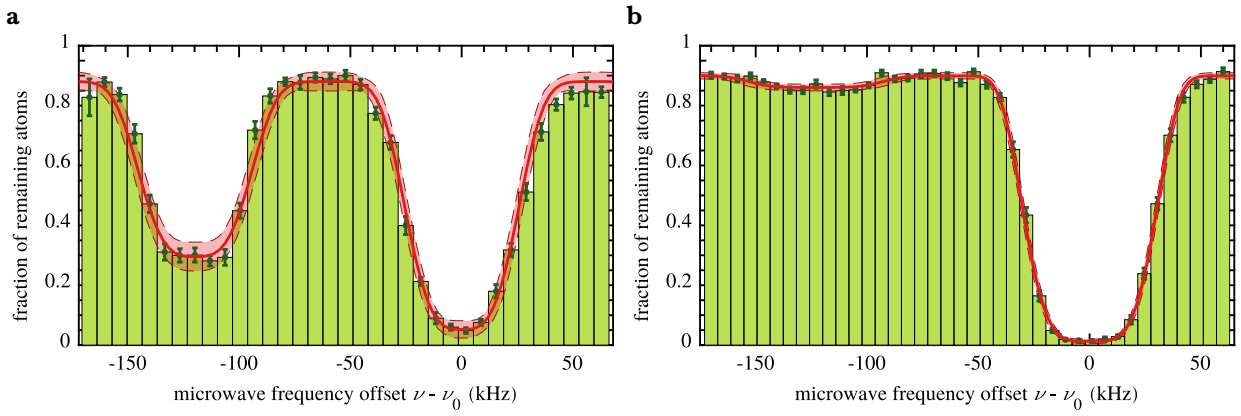

Fig. 3.5: Motional state tomography for atoms before (a) and after microwave cooling (b) detected at a trap depth of about $U_0 \approx 89\,\mu\mathrm{K}$. A fit of equation (3.17) to the carrier and the first red sideband (red line) for a thermal Boltzmann distribution shows good agreement with the data. The red shaded area indicates the 3σ confidence interval associated to the fit.

$n \leq i_{\mathrm{sb}} - 1$:

$$\boxed{P(-i_{\mathrm{sb}}\,\nu_x) \approx B \sum_{n=0}^{i_{\mathrm{sb}}-1} p_n}, \tag{3.16}$$

where the factor B which takes into account the baseline resulting from decoherence induced spin flips, not perfectly efficient pushouts and microwave pulses as well as off-resonant microwave transitions. We numerically confirmed this simple model given reasonable experimental parameters and motional state distributions by comparing it to sideband spectra extracted from equation (3.15), where the individual microwave transfer matrices were obtained by numerically solving equation (3.8). This does not only now allow to extract the ground state population p_0 by measuring the first red sideband $n \to n-1$, but also to extend this scheme to higher sideband transitions and allowing to extract the full distribution of motional states. For both applications the baseline B is measured by employing the same sequence but without triggering the Gaussian microwave pulses. This way we effectively measure the fraction of remaining atoms after the transport for far red detuned microwave transfers, which also includes losses and decoherence induced spin flips and therefore provides us with a value for the baseline.

Fast detection of ground state population

For the fast detection of the ground state population we just apply the presented scheme on the transition frequency of the first red sideband $\nu_{0\to1}$ and measure the corresponding baseline. As we saw in section 3.2.2 the anharmonicity of the lattice potential can shift the effective sideband frequency when exciting the atom to higher motional levels. For the majority of excitation analyzed in the context of fast atomic transport, chapter 4, it is however sufficient to compensate the anharmonicity induced sideband shift by a reasonable high number of microwave and pushout repetitions N_{mst}, which automatically leads to a flattening of the sideband plateaus, as shown in figure 3.5.

Motional state tomography spectra

If we instead measure a whole spectrum by scanning the microwave frequency over one or more sideband transitions we can directly use equation 3.17 to extract the motional state distributions. If we assume that both initial state preparation by the square pulse as well as the pushout efficiency is nearly perfect, a simpler fit model for $N_{\mathrm{mst}} \gg 1$ and in the case of a thermal Boltzmann distribution is given by a superposition of generalized Gaussian curves with width σ weighted by the corresponding

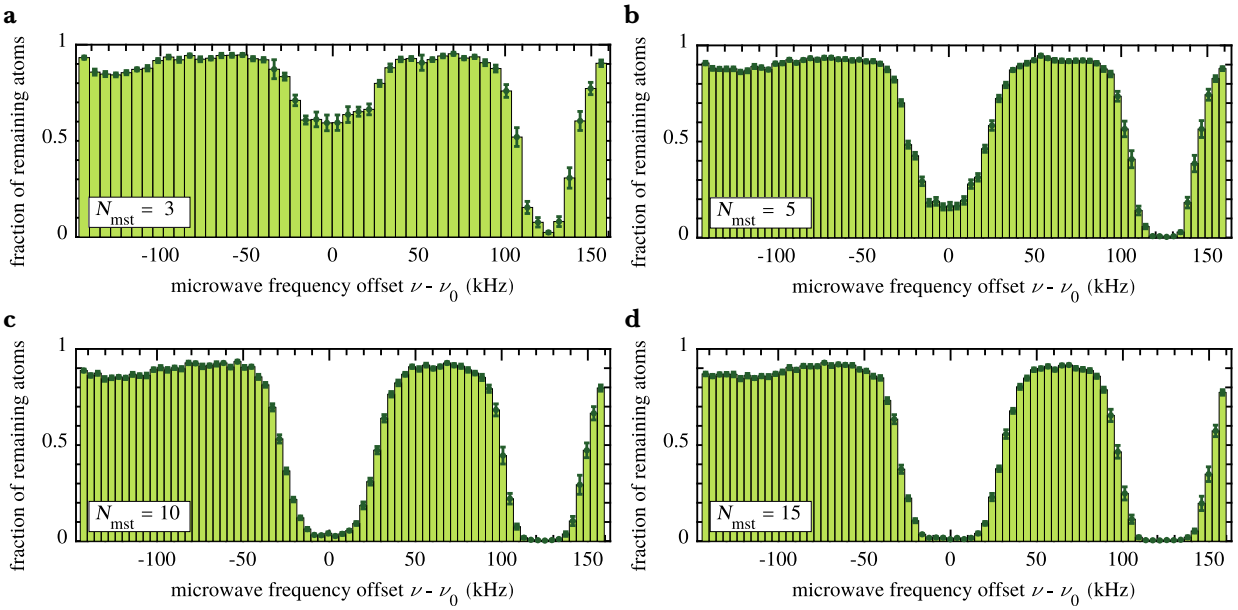

Fig. 3.6: Dependency of the motional state spectroscopy on the number of repetitions N_{mst} shown for ensembles of cooled atoms detected at a trap depth of about $80\,\mu\mathrm{K}$. Both the first red $n \rightarrow n-1$ (left) and blue sideband $n \rightarrow n+1$ (right) as well the carrier transition $n \rightarrow n$ (center) are shown. The Gaussian microwave pulse which is scanned over the whole range of frequencies is optimized for the sideband transition $n \rightarrow n-1$. The resulting microwave efficiency for the carrier is quite small as can be seen from (a) with $N_{\mathrm{mst}} = 3$ and the pulse is therefore not able to remove all atoms. While the red sideband height stays approximately constant for increasing number of microwave and pushout repetitions as expected, the carrier decreases strongly until for $N_{\mathrm{mst}} = 15$ nearly all atoms are removed. The blue sideband behaves similarly to the carrier – since we here allow to transfer all motional states except the highliest excited one – and shows nicely the expected flattening in the valleys.

motional state populations:

$$S(\nu) = B\left\{-\sum_{i_{\mathrm{sb}}}\left(1-\sum_{m=0}^{i_{\mathrm{sb}}-1} p_m\right)\exp\left[-\left(\frac{|\nu-\nu_{i_{\mathrm{sb}}}|}{|\sqrt{2}\,\sigma|}\right)^{\beta}\right]\right\}, \tag{3.17}$$

where the scaling factor β reproduces a simple Gaussian curve for $\beta = 2$ and mimics the flattening of the sidebands for $\beta > 2$. Figure 3.4b shows a broad scan with $N_{\mathrm{mst}} = 10$ repetitions which covers the first four red sidebands and represents a thermal Boltzmann distribution of atoms after microwave sideband cooling with a temperature of $\mathcal{T} = (4.0 \pm 0.2)\,\mu\mathrm{K}$, which does not represent perfect cooling but is in good agreement to the temperature estimated from standard microwave sideband spectroscopy. A direct comparison of the ground state population before and after microwave cooling can be seen from the two spectra shown in figure 3.5. A least square fit of equation (3.17) gives us $\mathcal{T} = (15.8 \pm 1.4)\,\mu\mathrm{K}$ before and $\mathcal{T} = (1.9 \pm 0.1)\,\mu\mathrm{K}$, corresponding to $p_0 = (19.4 \pm 2.5)\,\%$ and $p_0 = (96.1 \pm 1.1)\,\%$ for the estimated trap parameters.

The dependency of the recorded spectrum on the number of repetitions N_{mst} is shown in figure 3.6 for ensembles of microwave cooled atoms. While the microwave pulses on both carrier and blue sidebands allow to fully remove all atoms with the repeated pushout application, the red sideband heights saturate at a level given by the respective motional state populations. For reliably detecting of the motional ground state population we empirically estimated $N_{\mathrm{mst}} = 15$ as a good balance between efficient pulses and limited decoherence as well as off-resonant microwave transitions. Similar to the reduced carrier height observed in the standard microwave sideband spectrum, when comparing the spectra of cooled and uncooled atoms the carrier in the motional state detection scheme also changes its height. Again, the increase of the effective Rabi frequency leads to a decreased transition efficiency which limits the maximum fraction of removed atoms and also narrows the corresponding peak.

Chapter 4

Fast atom transport

As motivated before, atomic interferometry applications like discrete time quantum walks or Hong-Ou-Mandel interference strongly rely on the indistinguishability of particles which demands for transport operations, where the motional state of the atom is not changed. Since we are working with atoms prepared in the motional ground state of the lattice potential, we require transport sequences to not excite the atoms to higher motional states and the final atomic quantum state to be equivalent to the initial one up to a global phase factor. Transport sequences which satisfy this absence of vibrational excitations at the target position are described as 'faithful' or frictionless [69].

One way to achieve frictionless transport operations is by adiabatically ramping the lattice position and dragging the atom slowly along the optical dipole trap. The theorem of adiabaticity [70] ensures, that the system follows at all times the instantaneous eigenvalues and eigenstates of the time-dependent Hamiltonian. Therefore, if we initially prepare the atom in the motional ground state, it ensures that the system also remains in it. Unfortunately this process is intrinsically slow and the long transport times make this method experimentally impractical, since they often exceed times much longer than the coherence time of the quantum system, which is the main limitation for long experimental sequences.

Shortcuts to adiabaticity

One way to overcome these limitations is the so called 'bang-bang' transport scheme [36, 71, 72] which exploits the fact that single optical lattice sites can be approximated to first order by a harmonic oscillator potential. Abruptly accelerating and decelerating the lattice by two delta-like kicks, where the time between the kicks is exactly an integer multiple of the harmonic oscillation period, promises to leave the atom in the coherent ground state of the moving lattice potential. This shortcut to adiabaticity allows us to transport atoms over single lattice sites without creating nearly any excitation and was successfully used in numerous experiments over many years [22, 42, 73–75]. Due to the anharmonicities of the lattice the kick induced momentum transfer to the atoms has to be limited strongly, so that the required times for a faithful single lattice site transport is about two to three times the longitudinal oscillation period. We will analyze the linear transport scheme in detail in section 4.2.

The more general approach to the problem of fast atom transport which also takes into account the anharmonicity of the lattice potential and therefore should allow even shorter transport times is provided by quantum optimal control theory [76]. Here we allow arbitrary lattice shaking and find high-fidelity solutions by means of mathematical optimization methods, like Pontryagin maximum principle [77]. The methods of optimal control theory will be applied to the problem at hand in section 4.3.

When employing a general framework for the derivation of optimal transport sequences it is also very interesting to ask for the minimum transport time allowed for frictionless transport. We will see in section 4.4 that every quantum system has an intrinsic speed limit resulting from the energy time uncertainty relation. We will analyze this quantum speed limit by using a numerical quantum

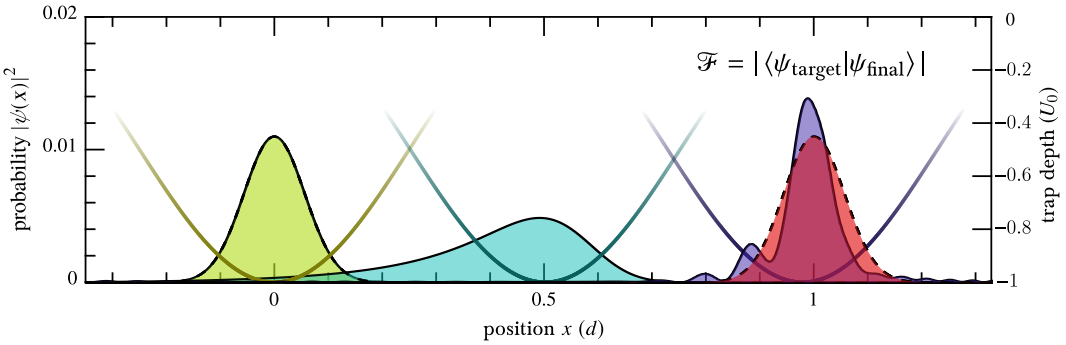

Fig. 4.1: Judging the quality of atomic transport sequences by the transport fidelity $\mathcal{F}$. The figure shows three snapshots of the spatial probability density $|\psi(x)|^2$ of the atomic wave function for a transport sequence connecting two motional ground states displaced by a distance $d = a_{\text{dt}}$ reaching a transport fidelity of 60.3 %. The time evolution is obtained from a numerical quantum simulation introduced in section 4.3.1.

simulation and explore it experimentally for the single site transport of single atoms.

To experimentally verify the numerical solutions presented in the following, we need a measure for the transport fidelity, which reliably tells the difference between a good and a bad transport sequence independent of the initial or final state. The here employed detection scheme is based on the motional state detection presented in chapter 3 and is discussed in the following section.

4.1 Transport fidelity

To judge the quality of an atomic transport, we introduce the transport fidelity $\mathcal{F}$, which is the absolute value of the overlap of the atomic wavefunction after transport $|\psi_{\text{final}}\rangle$ with the target state $|\psi_{\text{target}}\rangle$:

$$\boxed{\mathcal{F} = \left|\langle\psi_{\text{target}}\,|\,\psi_{\text{final}}\rangle\right| = \left|\langle\psi_{\text{target}}\,|\,\mathcal{U}_{0\to T}\,|\,\psi_{\text{init}}\rangle\right|}\,. \tag{4.1}$$

Here $\mathcal{U}_{0\to T}$ is the unitary time evolution operator, which describes the atomic motion determined by the time-dependent Schrödinger equation from an initial state $|\psi_{\text{init}}\rangle$ to a final state $|\psi_{\text{final}}\rangle$. For the time-dependent driven Hamiltonian $H(t)$ is is given by

$$\mathcal{U}_{t_1\to t_2} = \exp\left(-\frac{\mathrm{i}}{\hbar}\int_{t_1}^{t_2}\mathrm{d}\,t\;\; H(t)\right) \tag{4.2}$$

for any times $t_2 \geq t_1$ and contains the dependency on the the transport time T directly and the dependency on the transport sequence as well as the distance d through the time-dependent Hamiltonian $H(t) = H\,[x_0(t), U_0(t)]$. For transferring a localized atom from position x and motional state m to position $x + d$ and motional state n we specify the transition matrix elements of the transport fidelity as

$$\mathcal{F}_{m\to n}(d) = |\langle x + d,\, n\,|\,\mathcal{U}_{0\to T}\,|\,x,\, m\rangle| \tag{4.3}$$

In this thesis we will mostly focus on transport sequences interconnecting two localized motional ground states, so that $m = n = 0$.

Experimental measurement of the fidelity

Due to limited optical resolution it is impossible to precisely measure the spatial distribution of the atomic wave function after transport, as done in [78] for example, neither it is possible to detect the overlap with the target state in position basis. To judge the transport fidelity we however can rely on the methods of motional state detection, which were introduced in the previous chapter, to project the

atomic wavefunction on the longitudinal vibrational states of the lattice potential. If we assume that the atom is initially prepared in the motional ground state by means of microwave sideband cooling this allows to determine the transition matrix elements $\mathcal{F}_{0\to n}$ as given by equation (4.3).

Non-perfect cooling

If we however start with a not perfectly prepared ground state, meaning that the distribution of motional states $|n\rangle$ is for instance given by a Boltzmann distribution $p_n^{(init)}$ at finite temperature $\mathcal{T}$, the measured ground state population after the transport does not directly provides us with the transport fidelity $\mathcal{F}$. If we however make the assumption, that the initial state can be viewed as an statistical mixture of motional states, the population of the target ground state is approximately given by the sum of individual transition probabilities connecting the initial motional state $|n\rangle$ with the final state $|0\rangle$:

$$p_0^{(\text{final})} = \sum_{n=0}^{N-1} p_n^{(init)} \mathcal{F}_{n\to 0}\,, \tag{4.4}$$

where N is the number of bound states. We can then express the fidelity $\mathcal{F} = \mathcal{F}_{0\to 0}$ as the ratio of the measured ground state population before and after transport plus an additional correction term:

$$\boxed{\mathcal{F} = \left(\frac{p_0^{(\text{final})}}{p_0^{(\text{init})}}\right) - \sum_{n=1}^{N-1} \frac{p_n^{(init)}}{p_0^{(\text{init})}} \mathcal{F}_{n\to 0}}\,. \tag{4.5}$$

The initial temperature $\mathcal{T}$ and therefore also the initial excited state distributions p_n with $n \geq 1$ can be easily calculated by numerically solving the Boltzmann equation (3.4) given p_0. The transition probabilities $F_{n\to 0}$ for $n \geq 1$ can be theoretically estimated by employing a numerical quantum simulation. For all the experimentally measured transport sequences considered in this thesis the corresponding correction term however was derived to be always below $3\,\%$ and in most cases even below $0.3\,\%$. Compared to the usual uncertainties of the measurements we can therefore neglect this term without any concern and extract the transport fidelity just from the ratio of the ground state population before and after transport.

Transport survival

A second indicator for the success of the transport sequence is the transport survival. While it is not possible to distinguish between slight changes in the quality of the transport, the ratio of the number of atoms before and after the transport sequence can give a rough estimate on the amount of strongly excited and therefore lost atoms.

4.2 Linear transport in harmonic potentials

Until now transport sequences in the experiment used the so-called 'bang-bang' transport scheme, which relies on the harmonic approximation of the lattice potential for deep lattices. As illustrated in figure 4.2a it consists of a linear ramp of the lattice position over a distance d,

$$\boxed{x_0(t) = \begin{cases} 0 & t < 0 \\ \frac{d}{T}\,t & 0 \leq t \leq T \\ d & t > T \end{cases}}\,, \tag{4.6}$$

while the trap depth U_0 is kept constant during transport. The atom therefore exhibits two momentum kicks at time $t = 0$ and $t = T$, one accelerating the atom and one stopping the atom at its destination. If

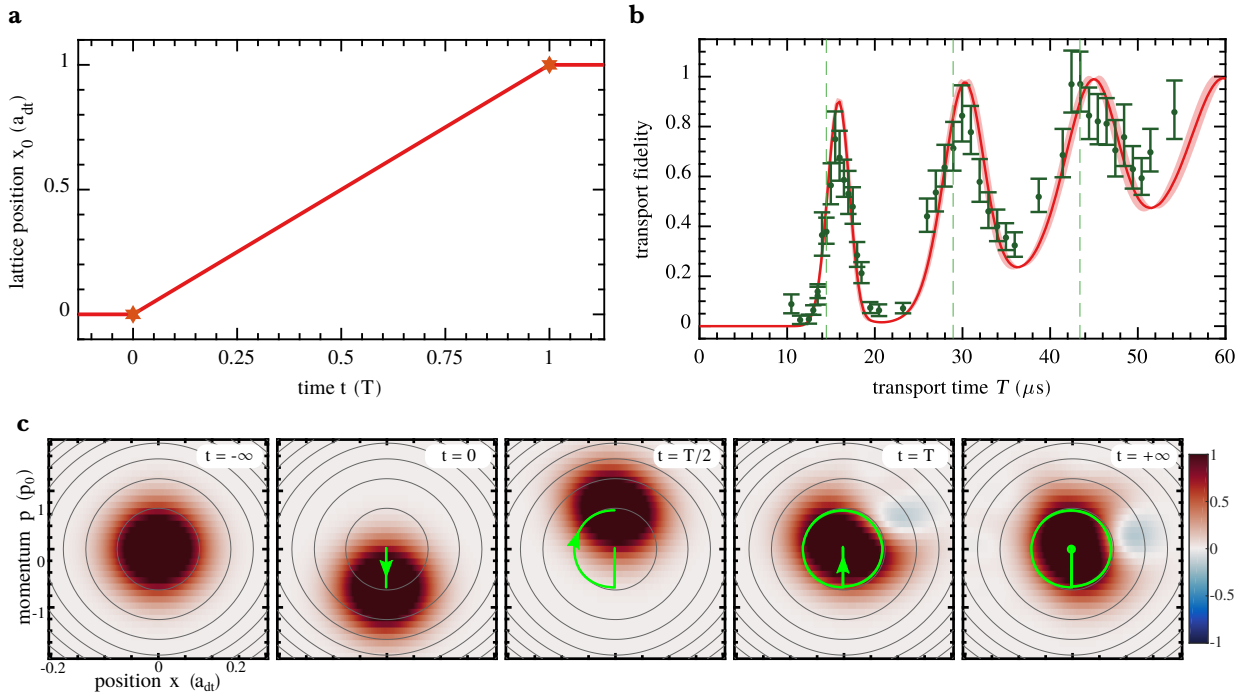

Fig. 4.2: Linear 'bang-bang' transport sequence (a) and corresponding measured transport fidelity (b) for different transport times T. The peaks of high-fidelity are separated by approximately multiples of the harmonic oscillator period $T_{\mathrm{ho}} = 14.5\,\mu\mathrm{s}$ (dashed green lines). The small deviation results from the strong anharmonicity of the optical lattice. The trap depth is obtained by fitting the transport fidelity using a numerical quantum simulation of the atomic motion (red line) and reads $U_0 = (28.62 \pm 0.24)\,\mu\mathrm{K} \times k_B$. The red shaded area indicates the $3\,\sigma$ confidence interval of the fit and the dashed gray lines multiples of the associated harmonic oscillator frequency. The simulated time evolution of the transport sequence for the second fidelity peak at $T = 30.39\,\mu\mathrm{s}$ is shown in Wigner phase space (c).

we choose the transport time T to be a integer multiple of the harmonic oscillator period $T_{\mathrm{ho}} = 1/\nu_{\mathrm{ho}}$, the transport sequence promises to reach a high transport fidelity.

We verified the transport fidelity experimentally by preparing atoms – optically pumped into the $|\uparrow\rangle$ spin state – in the motional ground state $|n = 0\rangle$ of their respective lattice site potentials and transporting them using the linear transport scheme over a distance $d = a_{\mathrm{dt}}$ while varying the transport time T. After the transport, the fidelity is determined from a measurement of the ground state population employing our new motional state detection scheme. The measured ground state populations are normalized by the ground state population without transport, which amounts just to $(83.5 \pm 8.9)\,\%$ due to non-perfect sideband cooling and slight vibrational heating, which was present in this particular run of the detection sequence. The estimated transport fidelity is shown in figure 4.2b. A least-square fit employing a numerical simulation of the quantum system taking into account the anharmonicities of our lattice potential, as introduced in section 4.3.1 shows a perfect agreement with the experimentally obtained data and allows to precisely determine the trap depth and associated harmonic oscillator period. We estimate $U_0 = (28.62 \pm 0.24)\,\mu\mathrm{K} \times k_B$ corresponding to a harmonic oscillator period of $T_{\mathrm{ho}} = (14.4 \pm 0.1)\,\mu\mathrm{s}$.

4.2.1 Coherent states

The 'bang-bang' transport relies on the harmonic approximation of the potential. The oscillating motion of a quantum particle confined in a harmonic oscillator is best described by the framework of coherent states, which closely resemble the oscillatory dynamics of a classical harmonic oscillator. A displacement of the motional ground state $|n = 0\rangle$ from the origin of the system can be described by

application of the displacement operator $D(\alpha) = \exp(\alpha\, a^\dagger - \alpha^*\, a)$, where

$$a = \frac{1}{\sqrt{2\, M\, \omega_{\mathrm{ho}}\, \hbar}}\, (M\, \omega_{\mathrm{ho}}\, x + \mathrm{i}\, p)\,, \qquad a^\dagger = \frac{1}{\sqrt{2\, M\, \omega_{\mathrm{ho}}\, \hbar}}\, (M\, \omega_{\mathrm{ho}}\, x - \mathrm{i}\, p) \tag{4.7}$$

are the annihilation and creation operator of the harmonic oscillator number states $|n\rangle$ and $\alpha \in \mathbb{C}$ is a measure of the displacement. Using the fact we can express any number state as $|n\rangle = (a^\dagger)^n/\sqrt{n!}\, |0\rangle$ the resulting coherent state can be written as a Poissonian distribution of number states,

$$|\alpha\rangle = D(\alpha)\, |0\rangle = \mathrm{e}^{-|\alpha|^2/2} \sum_{n=0}^{\infty} \frac{\alpha^n}{\sqrt{n!}}\, |n\rangle\,, \tag{4.8}$$

with mean $\langle n\rangle$ and variance $\Delta n^2 = \langle n^2\rangle - \langle n\rangle^2$ both equals to $|\alpha|^2$. The free time evolution of coherent states governed by the time independent Schrödinger equation is given by

$$\boxed{|\alpha(t)\rangle = \mathrm{e}^{-\mathrm{i}\,\omega_{\mathrm{ho}}\, t/2}\, D\left(\alpha\, \mathrm{e}^{-\mathrm{i}\,\omega_{\mathrm{ho}}\, t}\right)\, |0\rangle}\,. \tag{4.9}$$

The coordinate representation in position space therefore can be directly related to the harmonic ground state wave function given by equation (1.28) and the spatial probability density is given by a Gaussian with width $\sigma_x = \sqrt{2\,\hbar/(M\,\omega_{\mathrm{ho}})}$. The mean position and momentum of the wave packet are oscillating in phase space just like a classical pendulum,

$$\langle x(t)\rangle = \sqrt{\frac{2\,\hbar}{M\,\omega_{\mathrm{ho}}}}\, |\alpha|\, \cos(\kappa - \omega_{\mathrm{ho}}\, t)\,, \qquad \langle p(t)\rangle = \sqrt{2\, M \hbar\, \omega_{\mathrm{ho}}}\, |\alpha|\, \sin(\kappa - \omega_{\mathrm{ho}}\, t) \tag{4.10}$$

with phase $\kappa = \arg(\alpha)$. Furthermore it can be shown that the coherent states $|\alpha\rangle$ of the quantum harmonic oscillator satisfy the equality of the position and momentum Schrödinger uncertainty relation $\Delta p\, \Delta x = \hbar/2$ with $\Delta O = \sqrt{\langle O^2\rangle - \langle O\rangle^2}$ independent of α and therefore exhibit minimum uncertainty in position x and momentum p and keeps this even during time evolution.

To describe the principle of the 'bang-bang' transport sequence, we will therefore consider the potential to be harmonic and further assume that the transport sequence couples the ground states $|x,\, n = 0\rangle$ and $|x + d,\, n = 0\rangle$. To describe the full quantum dynamics in terms of coherent states, we transform to the reference frame moving with the lattice minimum position $x_{\mathrm{ref}}(t) = x_0(t)$.[1] The first momentum kick applied to the atom can then be understood as a displacement $D(\alpha_v)$ and the atom therefore is brought from $|n = 0\rangle$ into a coherent state $|\alpha_v\rangle$ with

$$\boxed{\alpha_v = \mathrm{i}\sqrt{\frac{M\, v^2}{2\,\hbar\,\omega_{\mathrm{ho}}}}}\,, \tag{4.11}$$

where $v = [x_0(T) - x_0(0)]\,/\,T$ is the (constant) velocity of the optical lattice during transport. During the linear part of the transport sequence, no force acts on the quantum system and from equation (4.10) we conclude that the coherent atomic state processes freely around the phase space origin with radius $\propto\ |\alpha_v|$ and its round-trip time given by the harmonic oscillator period T_{ho}. A second, opposite momentum kick at time $T = N\, T_{\mathrm{ho}}$ with integer N, corresponding to the displacement $D(-\alpha_v)$, brings the atom back to the ground state $|n = 0\rangle$.

4.2.2 Phase space representation

The Wigner function describes the distribution both in position and momentum space and is related to the position space wave function $\psi(x,\, t)$ by

$$W(x,\, p;\, t) = \int_{-\infty}^{\infty} \mathrm{d}\, y\ \ \psi^*(x + y,\, t)\, \psi(x - y,\, t)\, \mathrm{e}^{2\,\mathrm{i}\, p\, y/\hbar}\,. \tag{4.12}$$

[1] This transformation to a non-inertial reference frame will be discussed in the following chapter and a more detailed description is given in appendix A.3.

The harmonic oscillator ground state is represented by a two-dimensional Gaussian distribution with width $\sqrt{\hbar/(2\,M\,\omega)}$ in position and $p_0 \equiv \sqrt{2\,\hbar\,M\,\omega}$ in momentum space.

Figure 4.2c shows the simulated time evolution of an atom in a $U_0 = 25\,\mu\mathrm{K}\times k_B$ deep sinusoidal optical lattice subject to a 'bang-bang' linear transport sequence in Wigner phase space. The equipotential lines shown in the plot indicate the solutions $(x,\,p)$ of the classical particle energies

$$E(x,\,p) = \frac{p^2}{2\,M} + U_0\,(1 - \cos^2(k_{\mathrm{dt}}\,x)) \stackrel{!}{=} E_n \tag{4.13}$$

given the eigenenergies E_n of the motional states for all bound states $|n\rangle$. The here shown transport sequence brings the initially completely localized atom to a non-zero coherent state, which corresponds to an excitation of about one motional quanta. The coherent state propagates in Wigner phase around the origin $(x,\,p) = (0,\,0)$ as described by equation (4.10) with its orbital period approximately given by the harmonic oscillator period T_{ho}. After two full round trips, the second kick brings the atom back to the ground state.

Anharmonicities

Due to the strong anharmonicity of the lattice potential – only 11 motional states are totally bound – the required time for the atom to make a full cycle in phase space deviates slightly from the harmonic oscillator period. During the transport the wave packet undergoes furthermore a excursions of about $0.1\,a_{\mathrm{dt}}$ out of the potential minimum. Here, exposed to higher anharmonic contributions, the shape of the wave packet disperses which results in slight vibrational excitation and a reduced transport fidelity of $\mathcal{F} \approx 98\,\%$, while the harmonic counterpart would be completely lossless. This limits the application to higher multiples of the harmonic oscillator period, where the required momentum kick is much lower so that the excited atom does barely feel the anharmonicity of the lattice potential. Experimental applications in the past relied on non-perfect linear transport at two and nearly perfect transport at three times the harmonic oscillator period.

However, the linear transport approach is a good initial guess and reference for the optimization approach presented in the following section. To enable fast comparison over the reached transport times of the different transport approaches we like to give an overview over the intrinsic time scales at the here considered trap depths:

trap depth U_0	$15\,\mu\mathrm{K}\times k_B$	$25\,\mu\mathrm{K}\times k_B$	$30\,\mu\mathrm{K}\times k_B$	$80\,\mu\mathrm{K}\times k_B$
harmonic oscillator period T_{ho}	$19.98\,\mu\mathrm{s}$	$15.48\,\mu\mathrm{s}$	$14.13\,\mu\mathrm{s}$	$8.65\,\mu\mathrm{s}$

4.3 Optimal control transport

Optimal control theory

Optimal control describes the methods used to find a control feedback which minimizes or maximizes a specific performance criterion of a control system overcoming the iterative trial-and-error attempt of classical control system design [27]. Optimal control theory has its mathematical origin in the calculus of variations in the 17th century [79] and one of the probably most famous problems of optimal control theory is the Brachistochrone problem formulated by Johann Bernoulli in 1696 [80]. As a challenge "to the most acute mathematicians of the entire world" he asked for the path connecting two points on a plane in different heights which allows the fastest decent of a friction-less object only under the influence of gravity. With the formulation of the Euler-Lagrange equations, the work of Adrien-Marie Legendre and Karl Weierstrass and the maximum principle by Lev Pontryagin the foundations for the methods of modern optimal control theory were laid [81].

Quantum optimal control

Due to quantum interference of paths in the Hilbert space, optimization of quantum dynamics can not be directly formulated in the sense of classical optimal control theory [82]. Instead, a cost functional which describes the probability of reaching a defined target state is defined as a function of one or more control parameters, which can then be varied to minimize the cost. Additional constraints and costs associated with specific experimental conditions, like fixed maximum amplitudes or maximum overall power of control pulses, limited time resolution or limited feedback control bandwidth can either be included into the cost or handled directly by choosing appropriate mathematical optimization routines.

Optimal control atomic transport

Optimal control transport of atoms and atomic clouds trapped by optical tweezers, segmented dipole trap arrays or optical lattices has been analyzed in the past with both analytic as well as numerical attempts and mainly rely on the harmonic approximation of the considered trap potential.

Many analytic approaches are based on dynamical invariants, like the quadratic in momentum Lewis-Riesenfeld invariant, and are combined with methods to inverse engineer the optimal control solutions from classical particle solutions [83]. These methods were applied for example to atoms in displaced harmonic potentials realizing arbitrary fast transport sequences [84] and sequences robust against changes in the trap frequency [85]. Furthermore fast bang-bang and throw-catch optimal control transport sequences for single ions in a displaced harmonic oscillator were proposed to be applied in a real experimental setup [86]. Attempts for anharmonic potentials were made by estimating the fidelity drop of harmonic optimal control solutions for anharmonic distortions [84] or by bounding the relative displacement between trap center and classical particle trajectories [87]. By assuming a bounded displacement velocity, bang-bang like optimal control solutions for a displaced harmonic oscillator based on Pontryagin's maximum principle were found [69]. Another attempt to countervail anharmonicities can be made by the introduction of additional compensation forces allowing invariant-based inverse engineering solutions even for anharmonic distortions [88], which was also proposed for the experimental realization for transporting Bose-Einstein condensates under the influence of experimental noise [89].

Numerical attempts using steepest descent gradient search algorithms were used to find optimal control solutions for the transport of single ions in segmented Paul traps allowing high-fidelity transport in roughly two oscillation periods [90] Numerical optimization approaches mostly rely on special tailored optimization algorithm, like the Krotov algorithm [91] or Gradient-Ascent Pulse Engineering (GRAPE) [92] and often combined with a chopped random basis (CRAB) approach [93, 94] to minimize the solution space. These approaches were successfully applied to transport of single ions in segmented Paul traps [36, 95] Furthermore they realized fast quantum gates for atoms trapped in an optical double-well potential [96], improved engineering of phase transitions and loading of ultracold atoms in optical lattices [97] as well as counterdiabatic optimal control transport of trapped ions in an optical dipole trap in phase space [98]. To compensate bad performance of numerical optimization strategies even attempts to let humans solve the quantum optimal control problem of transporting ions in optical tweezers through a computer game [37] were made. However they were still being outperformed by the computer [38].

Roadmap

We will here attempt an numerical optimization approach based on a convenient basis selection and an rather usual, but high-performance interior point optimization algorithm. This algorithm will be applied to a numerical quantum simulation of the atomic motion taking into account the exact form of the anharmonic one-dimensional optical lattice potential. The extracted optimal control solutions will be then tested experimentally, which makes this ansatz an open loop control approach. We will

focus on the experimental verification of the numerically calculated optimal control sequences in section 4.4.

We will furthermore focus our search for optimal control transport ramps on atoms in spin state $|\uparrow\rangle$, since the dipole trap crosstalk compensation, as shown in section 1.5, allows us to construct optimal control transport ramps for spin state $|\downarrow\rangle$ directly from the solutions for spin $|\uparrow\rangle$. The successful application of this adaption is presented in [68].

4.3.1 Numerical optimization approach

If we limit the quantum system to an one-dimensional optical lattice, the atomic motion is described by the time-dependent Schrödinger equation. In the laboratory reference frame it is given by

$$\boxed{\mathrm{i}\,\hbar\,\frac{\partial}{\partial\,t}\,\psi(x,\,t) = H(x,\,t)\,\psi(x,\,t) = \left(\frac{p^2}{2\,M} - U_0(t)\,\cos^2\left[k_{\mathrm{dt}}\,(x - x_0(t))\right]\right)\psi(x,\,t)}, \tag{4.14}$$

where $p = -\mathrm{i}\,\hbar\,\partial_x$ is the momentum operator and $\psi(x,\,t)$ the atomic wave function. For arbitrary driving of lattice position $x_0(t)$ and trap depth $U_0(t)$ the general solutions of this equation are non-trivial and analytically not within reach.

To predict the dynamics for a given transport trajectory we therefore employ a numerical quantum simulation of the Schrödinger equation using a split-step method as introduced in appendix A.4. Therefore the atomic wave function is discretized on a finite position grid and its time evolution is obtained by approximating the Hamiltonian to be constant for small time steps of size δt. The expected accuracy is in the order of $\mathcal{O}(\delta t)^3$ and was tested and benchmarked extensively. For the considered transport times and spatial extensions of the wave function we choose 2^9 points for the discretization of one lattice site and about 2^{12} points for the discretization of time. This corresponds to a spacing of about $\delta x = 0.8\,\mathrm{nm}$ in position and a spacing of $\delta t = 2\,\mathrm{ns}$ to $5\,\mathrm{ns}$ in time domain and turned out to be more than sufficient.

To further increase the accuracy of the optimization algorithm and to be also able to have different viewpoints to analyze the transport sequences in detail we generalized the quantum simulation to arbitrary reference frames. Besides the laboratory frame we also consider the transport sequence in the reference frame co-moving with the lattice, which was already employed for the Wigner phase-space analysis in section 4.2.2, as well as the reference frame associated to the trajectory of a classical particle of mass M which is exposed to the same transport sequence. The latter is defined by the solution $x_{\mathrm{cl}}(t)$, $\dot{x}_{\mathrm{cl}}(t)$ to the classical Newtonian equation of motion

$$\boxed{M\,\ddot{x}_{\mathrm{cl}}(t) = \frac{\partial}{\partial\,x}U_0\,\cos^2\left[k_{\mathrm{dt}}\,(x - x_0(t))\right]\Big|_{x=x_{\mathrm{cl}}(t)} = -k_{\mathrm{dt}}\,\sin\left[2\,k_{\mathrm{dt}}\,(x_{\mathrm{cl}}(t) - x_0(t))\right]}. \tag{4.15}$$

The corresponding transformation to a non-inertial reference frame as well as the form of the transformed Hamiltonians is presented in more detail in appendix A.3.

The optimal control problem

For allowing arbitrary modulations of the transport trajectories we need to find an mathematical expression for any possible transport sequence. We choose a Fourier basis and write a general transport ramp as a superposition of a linear ramp and some sinusoidal modulations:

$$\boxed{\begin{aligned} x_0(t) &= x_0(0) + \frac{x_0(T) - x_0(0)}{T}\,t + \sum_{n=1}^{N_x} x_n^{(f)}\,\sin\left(\frac{\pi\,n}{T}\,t\right) \\ U_0(t) &= U_0(0) + \frac{U_0(T) - U_0(0)}{T}\,t + \sum_{n=1}^{N_U} U_n^{(f)}\,\sin\left(\frac{\pi\,n}{T}\,t\right) \end{aligned}}, \tag{4.16}$$

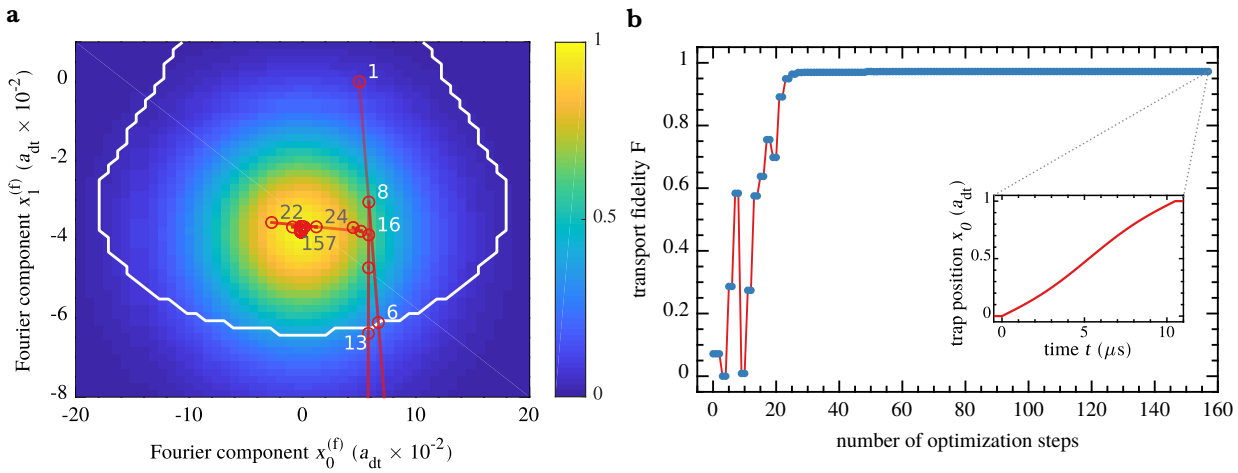

Fig. 4.3: The working principle of the interior point algorithm exemplary shown for a single-site transport optimization at a fixed trap depth of $U_0 = 80\,\mu\text{K} \times k_B$ and a transport time of $T = 10.5\,\mu\text{s}$ restricted to two trap position Fourier components (a). The transport fidelity is color-coded. The white line indicates the outer boundary of the feasible region as restricted by the phase slope constraint (2.23) and the red circles show the path of the optimization algorithm through the solution space with the numbers indicating the number of function calls. Figure (b) shows the corresponding transport fidelity in dependency on the number of optimization steps as well as the optimized transport sequence as an inset.

which directly takes care of the boundary conditions $x_0(t < 0) = x_0(0)$, $x_0(t > t) = x_0(T)$, $U_0(t < 0) = U_0(0)$ and $U_0(t > T) = U_0(T)$ for trap position and depth. Due to the constraint modulation bandwidth of both trap depth $U_0(t)$ and trap position $x_0(t)$, we can limit the number of Fourier components N_x, N_U to a finite number. However, as we will see in the following the intrinsic time scales of the quantum system itself decreases the number of effectively required Fourier components to a finite and numerically manageable number.

This now allows phrasing the optimal control problem for transporting an atom from state $|\psi_{\text{init}}\rangle$ over a distance d (in lattice sites) to state $|\psi_{\text{target}}\rangle$ in a given transport time T as a numerical minimization problem of the transport infidelity with respect to the Fourier components:

$$\min_{\{x_n^{(f)}\},\,\{U_n^{(f)}\}} \quad 1 - \mathcal{F}(x_0(t), U_0(t)) \,, \tag{4.17}$$

where the trajectories $x_0(t)$ and $U_0(t)$ are given by (4.16) with boundary conditions $x_0(0) = 0$, $x_0(T) = d$ and $U_0(0) = U_0(T) = U_0$ for all practical purposes. The minimization problem therefore also depends on the fixed transport time T. Now given some initial guess for the set of Fourier parameters we can employ an numerical minimization algorithm to solve the problem and optimize the transport fidelity. We will focus on also minimizing the transport time in section 4.4.

For experimental realization of the transport ramps we also like to introduce additional constraints on the Fourier components $\{x_n^{(f)}\}$, $\{U_n^{(f)}\}$. Due to limited laser power and to reduce the scattering rate of lattice photons during transport we like to restrict the trap depth to some range $U_0(t) \in [U_0^{(min)}, U_0^{(max)}]$. To allow for a reproducible phase lock response we also want to be able to limit the change of trap position $\dot{x}_0(t)$ to a finite interval as discussed in section 2.2.3. From equation (2.23) we conclude $|\dot{x}_0| \leq \dot{x}_0^{(\text{lim})} = 0.133\, a_{\text{dt}}\,\mu\text{s}^{-1}$. We can either add these constraints in terms of a cost functional to the transport infidelity and choosing suited weights or by adding hard constraints to the solution space in which the optimization algorithm searches for an optimum. After testing out both variants we chose the latter because of improved performance.

Choice of the optimization algorithm

In general given more than five or ten parameters which determine the cost functional, the optimization landscape is highly dimensional. We are furthermore confronted with a nonlinear programming problem in which the objective function and constraints are nonlinear functions of the optimization parameters. While linear or quadratic programming optimization problems allow to deduce a set of rules the solver can follow when determining gradients for determining the direction of search in the optimization landscape, nonlinear problems generally require an iterative procedure to scan the current surrounding of the optimization landscape at each major iteration.

The interior point algorithm [99–101] is a solver designed for a nonlinear programming problem with cost functional $c(x)$ subject to a set of in general nonlinear constraints. It is a large-scale optimization algorithm based on the repeated application of quadratic programming algorithms and uses barrier functions and trust region steps to ensure robustness. It can furthermore work with arbitrary nonlinear functions (which are convex) without providing any analytic gradients. The minimization problem can be phrased as

$$\min_x c(x) \quad \text{subject to} \quad u(x) \leq 0 \ \wedge \ v(x) = 0\,, \tag{4.18}$$

where $x \in \mathbb{R}^{N_x}$ is the in general multidimensional optimization parameter, $\{u_i(x)\}_{i=1}^{N_g}$ the set of inequality and $\{v_i(x)\}_{i=1}^{N_h}$ the set of equality constraints. In our case x is given by the set of Fourier components, which define the transport ramp as given by equation (4.16) and therefore $N_x = N_x + N_U$. If consider an optimization of both the trajectory in trap depth and lattice position and want to constrain both the maximum of the absolute trap velocity as well as the trap depth, we can phrase this in terms of the nonlinear inequality functions $u_i(x)$ and write

$$\begin{aligned} u_1(x) &= -\left(\min_t [U_0(t)] - U_0^{(\min)}\right), & u_2(x) &= +\left(\max_t [U_0(t)] - U_0^{(\max)}\right), \\ u_3(x) &= -\left(\min_t [\dot{x}_0(t)] + \dot{x}_0^{(\lim)}\right), & u_4(x) &= +\left(\max_t [\dot{x}_0(t)] - \dot{x}_0^{(\lim)}\right). \end{aligned} \tag{4.19}$$

We use the interior-point algorithm implementation provided by the numerical optimization toolbox of MATLAB [102].

Fidelity landscape

The working principle of the optimization algorithm is illustrated in figure 4.3 showing the fidelity landscape for a single-site transport optimization at a fixed trap depth of $U_0 = 80\,\mu\mathrm{K}\times k_B$ and transport time of $T = 10.5\,\mu\mathrm{s}$. For graphical purposes we restrict the number of Fourier components to $N_x = 2$ (and $N_U = 0$). With a transport time of 1.2 times the harmonic oscillator period at the given trap depth the linear bang-bang ramp is expected to be not of high fidelity and we therefore set the initial guess for the optimization parameter $x = (x_1^{(\mathrm{f})}, x_2^{(\mathrm{f})})$ to some random position in the optimization landscape. The size of the feasible region in which the algorithm is allowed to search for an optimal solution for the problem is limited by a hard boundary given by the constraints added to the system. We here choose an experimentally feasible setting and limit the maximum phase slope as described before which makes the boundary constrained region a drop shaped area. Starting from the initial guess the interior-point algorithm starts to traverse through the transport fidelity landscape by first scanning the bounds of this feasible region. When it finds a point which violate the constraints, it decreases the step size until it ends up back in the feasible region. It therefore scans the landscape from the 'interior' of the allowed area. After around 25 function calls the optimization already finds the relatively big peak of high fidelity and the last steps just slightly correct the position to its absolute maximum. The maximum transport fidelity of $\mathcal{F} = 97.23\,\%$ is reached at $x/a_{\mathrm{dt}} = (-0.1542, -3.8167) \times 10^{-2}$ after about 160 optimization steps, as shown in figure 4.3b. Larger solution spaces for $N_x \geq 15$ and $N_y \geq 15$ are traversed in similar order of step numbers, not exceeding 5000 function calls, which

makes the optimization of a single lattice site transport last from just a few seconds to maximum five minutes. With an relative fidelity increase of about one order of magnitude compared to the bang-bang solution at that specific transport time ($\mathcal{F} = 10.00\,\%$) even this simple optimization setup could already strongly improve the transport fidelity. With a comparable transport fidelity reached by the bang-bang solution at $T = 17.9\,\mu\text{s} \approx 2\,T_{\text{ho}}$ the optimal control solution could also decrease the the required time to about $60\,\%$. Additionally the required transport trajectory, as shown in the inset in figure 4.3b, is slightly smoother compared to linear ramp and with the limited bandwidth of out phase lock loop also experimentally easier to apply.

In the here considered setting with just two Fourier components to vary, the solution space is rather simple and just consists out of a single optimal control solution indicated by a strong fidelity peak close to the point $x/a_{\text{dt}} \approx (0, -4) \times 10^{-2}$ lying inside the restricted region. When increasing the solution space by adding more Fourier components or by removing the constraints, the fidelity landscape shows in general much more than one optimum solution. This raises the question whether the numerical optimization algorithm might get stuck in local but non-global minima. The question whether unconstrained optimal control problems can exhibit local traps in their fidelity landscape is subject to a controversial discussions in quantum optimal control theory. While there exists a lot of theoretical arguments for trap-free optimal control landscapes [82, 103], it is also easy to provide simple counterexamples of quantum systems which experience these sub-optimal extrema [104, 105]. However, local traps in the landscape are expected to be generally trivial to detect by standard optimization algorithms, which makes the search for optimal controls generally stable and robust against noise [106]. In the case of contrained optimal control landscapes local traps are proven always to exist, in practice however become for fixed control times also easy to escape [107]. In the analysis of the optimal control landscape associated to the transport fidelity we could confirm the existence of local traps in the presence of constraints like phase slope or amplitude limitations. In the small subset of the high-dimensional solution space which we scanned, the here used interior-point optimization algorithm however was mostly capable of escaping these traps. This was also confirmed by randomizing the initial guess of the optimization and obtaining the same or equally good optimal control solution. Only for really short transport times the optimization algorithm was getting stuck easily also in the absence of any constraints. We however believe that this could be circumvented by allowing for more optimization steps, as well as by tweaking the settings of the chosen optimization algorithm more carefully. A simple solution for reaching small transport times is provided in section 4.4.

4.3.2 Comparison to linear transport

For better comparison of the optimal control solutions to the ones predicted by the harmonic bang-bang transport scheme we consider two transport sequences of different duration at a relatively low lattice depth of $U_0 = 25\,\mu\text{K} \times k_B$, as shown in figure 4.4a. Both ramps reach a (simulated) transport fidelity of $\mathcal{F} \geq 99.99\,\%$. We here increase the number of Fourier components to $N_x = 15$, which as we will later find out is a good upper bound and believed to cover the full bandwidth of the quantum system. The initial guess is chosen to be an linear ramp with all Fourier components equal to zero. If not noted otherwise, this is the default setting for the following analysis.

While the slower transport sequence at $T = 2.2\,T_{\text{ho}} = 34.1\,\mu\text{s}$ looks relative smooth, the fast solution at $T = 1.5\,T_{\text{ho}} = 34.1\,\mu\text{s}$ relies on two hard kinks at $t = 0$ and $t = T$ comparable to the bang-bang solution as well as strong oscillations of the lattice potential during the transport sequence. We can also confirm this behavior by looking at the time evolution of the atomic wave function in Wigner phase space, as shown in figure 4.4. The longer optimal control solution just slightly excites the atom to less than a single motional quantum and keeps the atom always close to the trap center. Both the uncertainty in position as well as in momentum stay approximately constant during the transport sequence, making the atom always remain in a coherent-like state. The transport trajectory in phase space therefore just performs a small closed loop cycle in phase space.

The fast transport sequence in comparison strongly excites the atom with the initial kick close to the boundary of possible and bound momenta, where we can already conclude an approximate

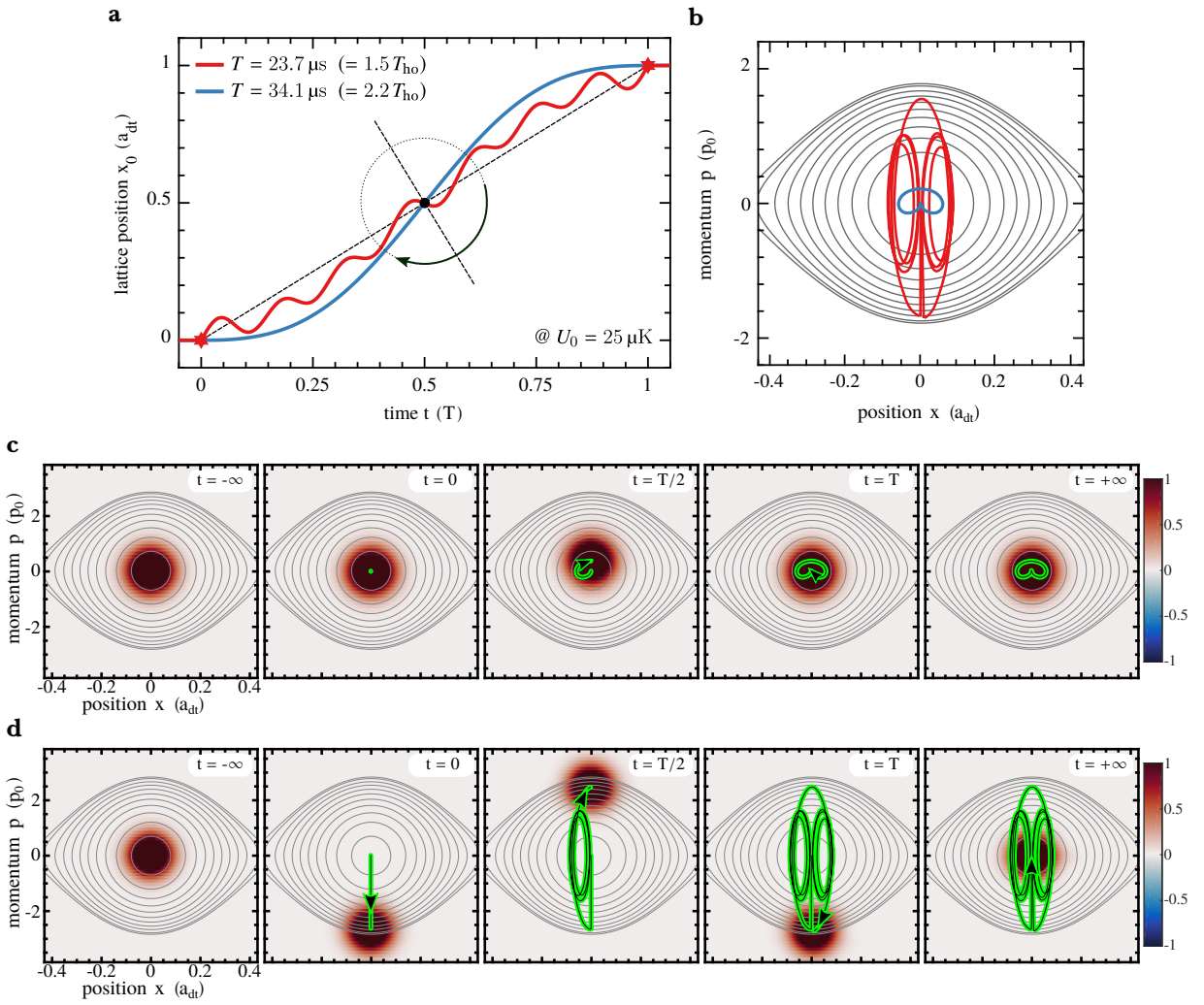

Fig. 4.4: Two optimal control transport sequences for different transport times (a) and the comparison of their trajectories in Wigner phase space (b), (c), (d) shown in the co-moving reference frame of the trap position. The trap depth is fixed at $U_0 = 25\,\mu\mathrm{K} \times k_B$ and the ramps are obtained by the numerical optimization with $N_x = 15$ Fourier components. Both the slow (blue line) as well as the fast transport sequence (red line) reach a transport fidelity of above $99.99\,\%$.

time limit for this type of control, since for even faster transport sequences this amount of excitation increases furthermore. The energy transferred to the atom is mainly converted into kinetic energy of the atom making it oscillate strongly through nearly all possible momenta. By however keeping the atom also always close to the trap center and therefore limiting the potential energy strongly, the atom is protected by the strong anharmonicity of the relatively shallow lattice and instead stays in a coherent-like state during the whole time evolution. Instead of being forced to let the system freely evolve in between the momentum kicks, the optimal control solution is able to modulate the trap in a way, that the state can jump between the circular energetic levels of the respective coherent states. These modulation induced shortcuts in phase space makes the optimal control ramp beat not only the adiabatic approach by far, but also improves strongly over the simple linear bang-bang solution, which can just shorten the path at the initial and and final momentum kick.

We can furthermore see clearly, that the optimization algorithm tends to symmetrize both the transport ramp as well as the time evolution in phase space. The former shows a rotational symmetry round the half time point $t = T/2$, $x_0(T/2) = a_{\mathrm{dt}}/2$ and the latter is mirror symmetric around the $x = 0$ axis in phase space. We will analyze this symmetry in the next section.

4.3.3 Symmetries

As discussed before, the periodicity of the lattice potential implies a discrete translational symmetry of the Hamiltonian. We will now show that the system exposed to an optimal control transport sequence also exhibits a time-reversal symmetry, which we will relate to the rotational symmetry of the transport trajectory as observed in figure 4.4a.

Time reversal symmetry

We consider an optimal control transport sequence $x_0(t)$, $U_0(t)$ for transporting $|x,\, n\rangle$ to $|x+d,\, n\rangle$ in time T with $d = N\, a_{\mathrm{dt}}$ ($N \in \mathbb{Z}$) a multiple of the lattice constant and assume that the transport fidelity reaches $\mathcal{F}_{n,\,n}(d) = 1$. Given that $x_0(0) = 0$, $x_0(T) = d$, as well as $U_0(0) = U_0(T)$, the initial and final state can then be related to each other by employing the discrete translational invariance $x \to x + a_{\mathrm{dt}}$ represented by the shift operator $\mathrm{T} \equiv \mathrm{T}(a_{\mathrm{dt}}) = \exp(-\mathrm{i}\, a_{\mathrm{dt}}\, p/\hbar)$. Except an additional dynamical, constant phase α, the final state is directly given by the initial state displaced by N lattice sites:

$$|\psi(x,\, T)\rangle = \mathrm{e}^{i\,\alpha}\, \mathrm{T}^N\ |\psi(x,\, 0)\rangle = \mathrm{e}^{i\,\alpha}\ |\psi(x + N\, a_{\mathrm{dt}},\, 0)\rangle \tag{4.20}$$

For the specified optimal control transport sequence the Hamiltonian of the driven quantum system therefore should therefore be symmetric under the effect of time reversal Θ and discrete translation T^N:

$$\left[H(t), \Theta\, \mathrm{T}^N\right] = 0 \tag{4.21}$$

If we employ the commutator and anticommutator relations for the anti-unitary operator Θ of time reversal and the unitary operator T of the discrete translational symmetry with respect to momentum operator p and position operator x,

$$[\Theta,\, x] = \{\Theta,\, p\} = [\mathrm{T},\, p] = 0\,, \qquad [\mathrm{T},\, x] = a_{\mathrm{dt}}\, \mathrm{T}\,, \tag{4.22}$$

the symmetry condition, equation (4.21), leads after a lengthy but straight-forward calculation to a condition on the optimal control trajectory $x_0(t)$, $U_0(t)$:

$$x_0(T-t) = d - x_0(t)\,, \qquad U_0(T-t) = U_0(t)\,, \tag{4.23}$$

which shows exactly the expected behavior. By substituting $t \to t + T/2$ the condition on the trajectory can also be viewed as a 2-fold rotational symmetry of the trap position $x_0(t)$ around the point $x_0(T/2) = d/2$ and a mirror symmetry of the trap depth trajectory $U_0(t)$ around $t = T/2$:

$$x_0(T/2 + t) - d/2 = -x_0(T/2 - t) + d/2\,, \qquad U_0(T/2 + t) = U_0(T/2 - t)\,. \tag{4.24}$$

We can confirm this symmetry by our unconstrained optimization algorithm, which prefers these symmetries intrinsically.

This also provides us with an recipe for the inverse optimal control sequence transporting $|x + d,\, n\rangle$ back to $|x,\, n\rangle$ in time T reaching a again transport fidelity of $\mathcal{F}_{n,\,n}(-d) = 1$. We tested this numerically by reversing (constraint-free) optimal control sequences in time and direction and estimating the resulting transport fidelity by our quantum simulation. We could also confirm this behavior for unconstrained optimized transport sequences with transport fidelities below $100\,\%$. Time reversal symmetry is therefore one of the key elements enabling fast optimal control transport. It does allow the wave function to spread out during the fast transport sequence until the reversal point at $t = T/2$ is reached, from where it then contracts back to the motional ground state.

Symmetries of the time-evolution operator

Given a optimal control solution $x_0(t)$, $U_0(t)$ we take look at the properties of the time evolution operator $\mathcal{U}_{t_0 \to t_1}$, which relates the state $|\psi(t_1)\rangle$ at time $t = t_1$ to some state $|\psi(t_0)\rangle$ previous in time

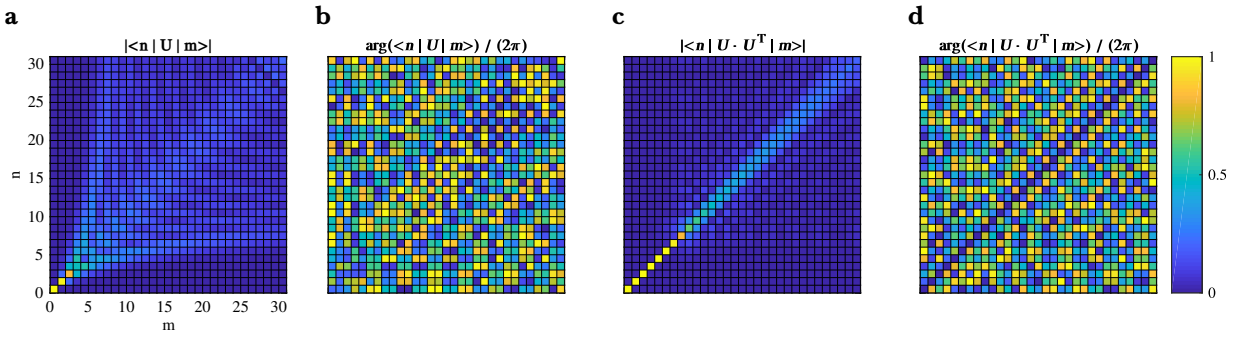

Fig. 4.5: Matrix elements of the time evolution operator $U \equiv U_{0\to T}$ associated to a optimal control transport sequence for a deep lattice with 32 bound motional states. The amplitude (a) of the transition matrix element $\langle m|U|n\rangle$ is symmetric in $n \leftrightarrow m$, while the phase (b) shows this symmetry only approximately. The optimal control sequence at the trapping frequency of $\nu_{\mathrm{ho}} = 200\,\mathrm{kHz}$ reach a fidelity $\geq 99.99\,\%$ for transporting $|n = 0,\, x\rangle$ to $|n = 0,\, x + 1\rangle$ in $T = 5.5\,\mu\mathrm{s}$. The transport fidelity decreases with increasing initial and final motional state number n, while transitions $|m,\, x\rangle$ to $|n,\, x + 1\rangle$ with $m \neq n$ are strongly suppressed. Both amplitude (c) and phase (d) of the transition matrix elements $\langle m|U \cdot U^{\dagger}|n\rangle$ indicate, that U is unitary for small m, n.

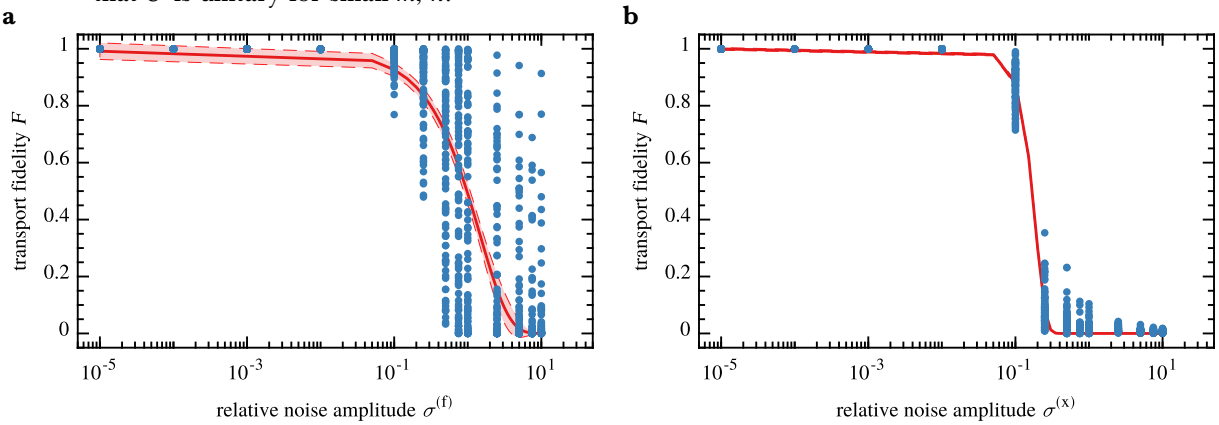

Fig. 4.6: Optimal control transport sequence affected by noise in the the Fourier components (a) and direct noise added to the lattice trajectory (b). The red line indicates a simple fit with a Gaussian error function.

$t_0 \leq t_1$ and for a time-dependent Hamiltonian $H(t)$ is given by the matrix exponential

$$\mathcal{U}_{t_0\to t_1} = \mathbb{T}\,\exp\left(-\frac{\mathrm{i}}{\hbar}\int_{t_0}^{t_1}\mathrm{d}\,t\,H(t)\right), \tag{4.25}$$

where $\mathbb{T}$ denoted the operator of time-ordering.

We calculate the matrix elements of $\mathcal{U}_{0\to T}$ and $\mathcal{U}_{0\to T}\cdot\mathcal{U}^{\dagger}_{0\to T}$ for an optimal control transport sequence of T = with a deep and fixed trap depth which gives rise to the interconnection of 32 bound motional states. We can can not only extract the individual transition probabilities $\mathcal{F}_{m\to n} = |\langle n|\mathcal{U}_{0\to T}|m\rangle|$, but also the corresponding phases $\arg\left(\langle n|\mathcal{U}_{0\to T}|m\rangle\right)$. We also analyzed the unitarity condition $\langle n|\mathcal{U}_{0\to T}\cdot\mathcal{U}^{\dagger}_{0\to T}|m\rangle = \delta_{m\,n}$. The results are shown in figure 4.5.

4.3.4 Robustness

For experimental applications like atomic interferometry, we would also like the transport fidelity to be robust against a non-perfect preparation of initial state, timing imperfections and against small deviations of the transport trajectory as well as noise. The former was already confirmed numerically with the absolute matrix elements of the time-evolution operator corresponding to a optimal control

solution for $|n=0\rangle \rightarrow |n=0\rangle$ decreasing just slowly for interconnecting the two lattice sites with increasing initial and final motional state number n. Therefore not perfect cooled atoms are expected to be transported nearly as good as perfectly cooled ones, even when we optimize the transport sequence just for coupling the two ground states.

To simulate experimental noise affecting the transport trajectory we replace

$$x_0(t) \rightarrow x_0(t)\,[1+\eta(t)] \tag{4.26}$$

for an optimal control solution $x_0(t)$. Here $\eta(t)$ is drawn from a normal distribution of zero mean and standard deviation $\sigma^{(x)}$ for each simulated time t. We scan the width $\sigma^{(x)}$ from 1×10^{-5} to 10 and always draw 100 corresponding random trajectories $\eta(t)$ for which we then simulate the corresponding transport trajectory numerically. The extracted fidelity, shown in figure 4.6b, shows a relatively wide plateau close to $\mathcal{F}=1$ for relative noise fluctuations below 1×10^{-1} which confirms the generally predicted robustness of optimal control transport sequences.

Small deviations from the desired transport trajectory can be induced by the limited efficiency of the iterative optical error correction or non-perfect deconvolution. We can simulate this type of changes by modulating the Fourier components $\{x_n^{(f)}\}$ of some optimal control ramp $x_0(t)$. We therefore write

$$x_0(t) = \frac{d}{T}\,t + \sum_{n=1}^{N_x} x_n^{(f)}\,(1+\eta_n)\sin\left(\frac{\pi\,n}{T}\,t\right) \tag{4.27}$$

with η_n being drawn from a normal distribution with mean $\sigma^{(f)}$. We again scan $\sigma^{(f)}$ from 1×10^{-5} to 10 and calculate and simulate for each point 100 transport trajectories. The results are shown in figure 4.6a. While the fidelity drop at a relative fluctuation of 1×10^{-1} is much stronger than the one before, the transport fidelity shows a really similar behavior indicating strong robustness against small deviations in the transport trajectory.

As we saw in the previous section, really fast optimal control transport sequences rely on two momentum kicks which are well spaced in time. The most severe deviations from the desired trap trajectory originate therefore in timing imperfections of these two kicks. We therefore calculated a optimal control transport sequence for fixed time ($T=14\,\mu s$) and fixed trap depth ($U_0\approx 80\,\mu K\times k_B$) and checked the transport fidelity of the ramp with same Fourier components but changed transport time T both numerically and experimentally. Apparently the experimental data was taken before we implemented the new motional state detection technique. We therefore rely on the transport fidelity extracted from the cooling and heating sideband height detected by standard microwave sideband spectroscopy. Since we work here with a much deeper lattice the expected anharmonicity-induced sideband shift is expected to be not so severe. The transport fidelity is extracted from the sideband heights and the transport survival by fitting equation (3.10) and employing the quantum simulation to predict a good initial guess for the strongly restricted number of free parameters. More details to this approach can be found in [68]. The experimentally obtained ground state population is then normalized by the ground state population without transport and the extracted transport fidelity is shown in figure 4.7a together with the simulated time evolution of the stretched transport ramp at three different times in Wigner phase space in figure 4.7b. The optimal control solution at $T=14\,\mu s$ reaches a transport fidelity of $(97.85\pm2.31)\,\%$ which is in good agreement with the simulation. The corresponding trajectory in phase space shows the nearly vanishing excitation of the final state by a small dot at the origin. When stretching the transport ramp the fidelity is relatively robust against small timing uncertainties. When increasing the timing deviation to a few microseconds the imprecise timing of the final momentum kick leaves the final state oscillating around the origin. The increased radius of the final state trajectory for the shown time stretch of $1\,\mu s$ and $2\,\mu s$ indicates the excitation induced by the timing uncertainty. The experimentally measured transport fidelity corresponding to these two transport ramp deformations is $\mathcal{F}=(77.41\pm3.87)\,\%$ for a stretched transport time of $T=15\,\mu s$ and drops down to $\mathcal{F}=(48.94\pm4.11)\,\%$ for $T=16\,\mu s$.

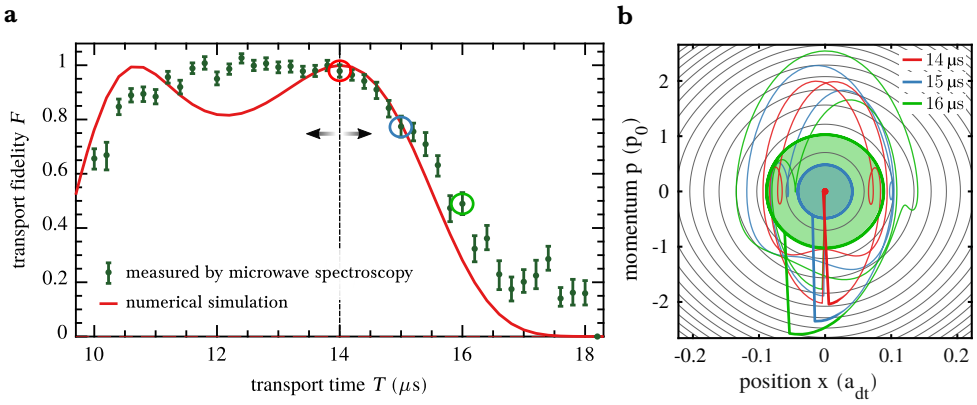

Fig. 4.7: Optimal control transport sequence affected by timing uncertainties. The optimal control solution at $T = 14\,\mu s$ at a trap depth of about $80\,\mu K \times k_B$ is stretched in time (a) and the resulting transport fidelity is simulated (red line) and experimentally measured (green errorbars). The phase space evolution shown for $T = 14\,\mu s$, $15\,\mu s$ and $16\,\mu s$ (b) shows the residual excitations.

4.4 Quantum speed limit

The quantum speed limit is the fundamental upper bound on the speed of any quantum evolution and determines how fast quantum states can evolve. It originates in the Heisenberg uncertainty relation of energy and time,

$$\boxed{\Delta E\,\Delta t \geq \frac{\hbar}{2}}\,. \tag{4.28}$$

This energy-time relation represents a special case, since the Heisenberg uncertainty principle generally makes a statement about the precision at which two observables can be measured at the same time, which does not make much sense when trying to consider time as one of those observables, since it generally can not be expressed as a Hermitian operator. The quantum speed limit gives therefore more an intrinsic time scale of the quantum dynamics, which was first rigorously shown by Mandelstam and Tamm [108]. We will analyze their results in section 4.4.3 in more detail. The quantum speed limit therefore limits "the maximal rate with which quantum information can be communicated, the maximal rate with which quantum information can be processed, the maximal rate of quantum entropy production, the shortest time-scale for quantum optimal control algorithms to converge [and] the best precision in quantum metrology" [39].

In the past years, the quantum speed limit has been extensively analyzed for a variety of quantum systems and it is believed to be an intrinsic limit to any quantum system . It has been generalized for non-unitary dynamics of open quantum systems [109–111] extending to non-Markovian dynamics [112] like leakage or decoherence [113]. Recent work also showed that the quantum speed limit is not an intrinsic property of quantum systems but a universal dynamical property of any Hilbert space [114]. The classical speed limit is set by a given norm of the generator of time evolution, which allows to also analyze the speed limit for the across the quantum-to-classical transition [115].

In the following section we will analyze the intrinsic speed limit of our quantum system by means of optimal control theory and our numerical simulation. In section 4.4.2 we will present the results of our attempt to measure the quantum speed limit at a fixed trap depth experimentally. We will compare the obtained limits with theoretically predicted bounds as well as analytically obtained solutions in section 4.4.3.

4.4.1 Optimal control approach

In the context of this work, the quantum speed limit is given by the minimum time, T_{qsl}, for which the transport fidelity is still one. We will here mostly restrict the analysis to lattice shift induced coupling between two motional ground states separated by some distance d and just have a brief insight into

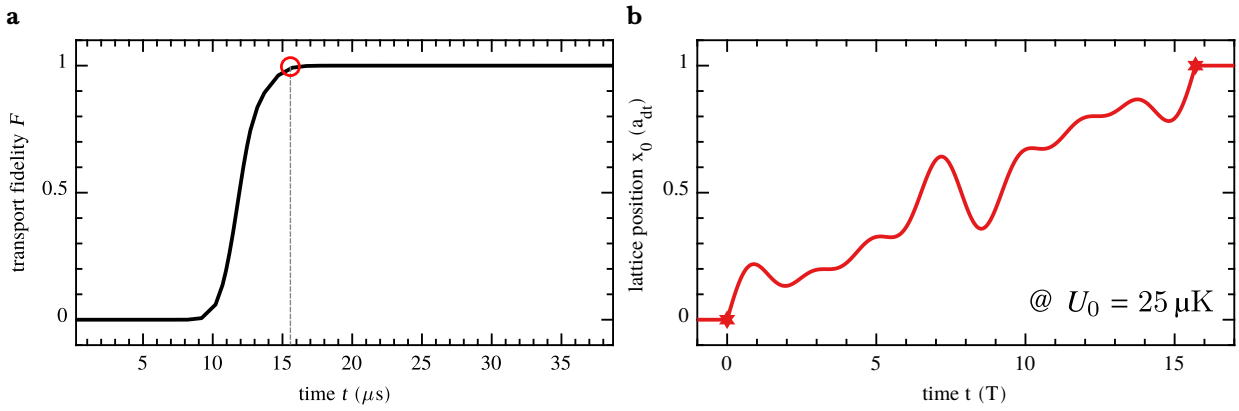

Fig. 4.8: Numerically obtained transport fidelity from the decreasing time approach (a) and the corresponding optimal control ramp at the identified quantum speed limit of $T \approx 15.5\,\mu s$ (b). The trap depth is fixed at $U_0 = 25\,\mu K \times k_B$. The dashed line indicated the harmonic oscillator period.

the case of additionally allowed trap depth modulations at the end. To consider uncertainties of our numerical quantum simulation as well as of our experimentally obtained data we will relax the conditions a little bit and consider the quantum speed limit as the minimum time for which the simulated or experimentally obtained quantum speed limit is $\geq 99\,\%$:

$$\boxed{T_{\text{qsl}} \equiv \min\left(\{T \mid \mathcal{F} \geq 0.99\}\right)}. \tag{4.29}$$

Decreasing time approach

To obtain this quantum speed limit numerically we have to decrease the fixed transport time T constantly until the optimization algorithm can no longer improve the transport fidelity to above $99\,\%$. With decreasing time it however becomes harder and harder to find a good initial guess for the transport sequence. As we saw from our analysis before, the considered optimal control solutions possess a relative strong robustness against small timing uncertainties and optimal control transport sequences for small transport time differences are therefore expected to be quite similar. The initial guess for the calculation is therefore chosen to be a linear transport ramp at ≥ 2 times the harmonic oscillator period which provides always a relative high transport fidelity. When decreasing the transport time by small amounts we then take the previous optimal control solution as the initial guess for the next point in time. Non the less we have to note that this approach might restrict the scan of the solution space to a specific region of the fidelity landscape and therefore biases the form of the optimal control transport trajectory. From the obtained optimal control solutions we can however observe that while the solutions do not differ much for small transport time changes, but show strong changes over longer times. While optimal control ramps for short times exhibit strong oscillations as well as a strong initial and final momentum kick, long time solutions are much smoother, as already discussed in section 4.3.2. We also tested to optimize the transport time starting from randomized Fourier components and different times. While this method did not worked reliably for short transport times below 1.5 times the harmonic oscillator period, when strongly increasing the number of allowed optimization steps the algorithm was for longer transport times usually able to obtain the same transport fidelity and similar optimal control solutions as our decreasing time approach.

An example for a numerically obtained quantum speed limit and the corresponding transport sequence at $T = T_{\text{qsl}}$ for a (fixed) trap depth of $25\,\mu K \times k_B$ is shown in figure 4.8. We can indicate he quantum speed limit by a drop of the transport close to $T_{\text{qsl}} = 15.5\,\mu s$. Below this point the unconstrained optimization algorithm was not able to increase the transport fidelity to above $99\,\%$ even when decreasing the time steps or starting from an other initial guess for longer times. We note, that while the transport fidelity steadily drops below the quantum speed limit, the optimized transport sequence are still optimal control solutions and no transport protocols with higher fidelity

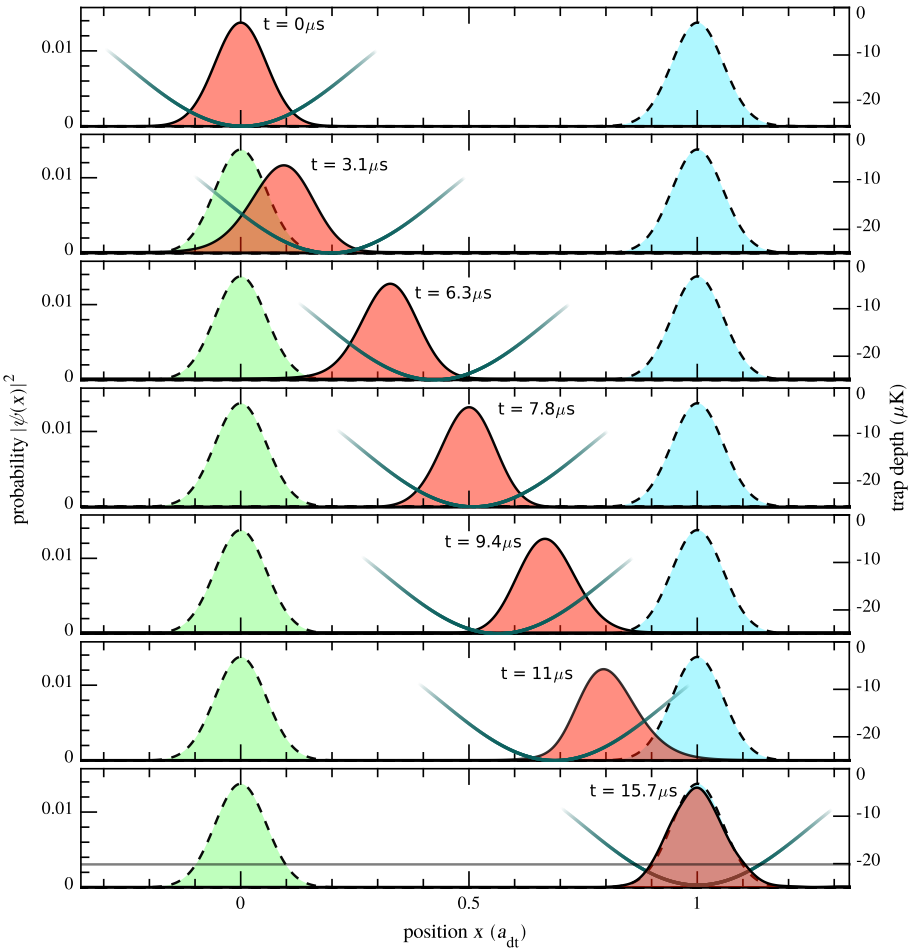

Fig. 4.9: Simulated time evolution of the optimal control transport sequence shown in figure 4.8b. We show the time evolution of the absolute norm of the wave function $\psi(x, t)$ in the laboratory reference frame for seven different points in time.

are expected to exist. We can also understand this by looking at the corresponding time evolution of the wave packet at the identified quantum speed limit. The transport sequence, figure 4.8b, shows strong kinks at the initial and final time. While during transport the atomic wave function is not pushed to the spatial boundary of the moving potential well, as illustrated in figure 4.9, the phase space analysis shows that the initial kick however excites the atom to the maximum of classically allowed momentum. The here shown optimization was performed allowing the algorithm to vary $N_x = 15$ Fourier components for modulating the transport trajectory.

Dependency on the number of Fourier components

The dependency of the numerically obtained speed limit on the number of used Fourier components when modulating the lattice position in time is shown exemplary in figure 4.10 for a trap depth of $U_0 = 80\,\mu\mathrm{K} \times k_B$. By taking a linear ramp as the initial guess, the non-optimized fidelity curve in figure 4.10a resembles the characteristic peak structure of the bang-bang transport method with peaks of high fidelity spaced in time by multiples of the harmonic oscillator period. The estimated speed limit lies at about 5 times the harmonic oscillation frequency. If we allow the optimization algorithm to vary just the lowest frequency Fourier component the fidelity in between the bang-bang maxima slightly increases and the $\mathcal{F} \geq 0.99$ condition is fulfilled already at $T \approx 4\,T_{\mathrm{ho}}$. With increasing N_x the optimal control solutions become more and more robust against changes in the transport time. For $N_x \geq 3$ Fourier components the fidelity for $T \gg T_{\mathrm{ho}}$ already becomes a plateau and high fidelities ≥ 0.99 down to the hard boundary of the quantum speed limit $T_{\mathrm{qsl}} = T_{\mathrm{ho}}$ are obtained for $N_x \geq 7$.

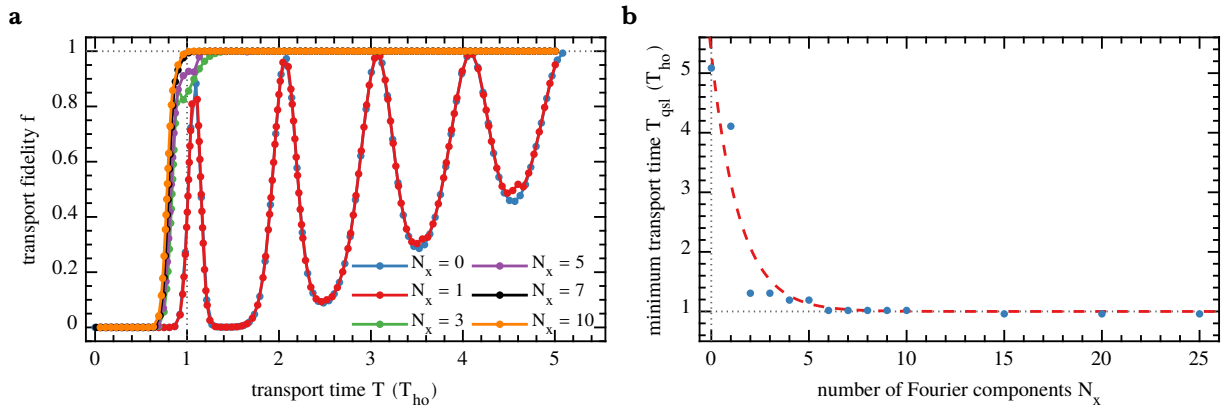

Fig. 4.10: Dependency of the numerically obtained quantum speed limit on the number of Fourier components. The trap depth is fixed at $U_0 = 80\,\mu\mathrm{K} \times k_B$ for a transport of the motional ground state over a single lattice site. The initial guess is set to a linear transport sequence, so that for $N_x = 0$ without optimization the characteristic peak structure of the bang-bang transport is visible (blue curve in (a)) and the minimum time for a transport fidelity of $\mathcal{F} = 0.99$ is achieved at about five times the harmonic oscillator period T_{ho} as shown in (b). With $N_x = 1$ (red curve in (a)) the optimization can just slightly improve the fidelity in-between the maxima, but brings the speed limit to the fourth bang-bang peak. With increasing $N_x > 1$ the optimization quickly explores the hard boundary given by the harmonic oscillator period. The red dashed line in (a) indicates the approximately exponential saturation behavior for large N_{x}.

This behavior slightly changes with the given trap depth and required number of Fourier components slightly increases for shallower lattices. For all here considered trap depths, the minimum transport time however could not be lowered when increasing the number of Fourier components to above $N_x = 10$ to 15. We therefore empirically found a good compromise between computational effort and reliable performance for all considered parameters by setting $N_x = 15$ for the rest of the analysis. Only when imply the transport ramps in trap depth or lattice position to be symmetric, the number of Fourier components could be reduced for improved performance without loosing reliability.

Trap depth dependency

As shown in figure 4.11a the quantum speed limit time shows a strong $\propto (U_0)^{-1/2}$ behavior for the whole range from quite shallow to really deep lattice potentials, which reminds of the scaling behavior of the harmonic oscillator period. Indeed the numerical results reveal, that the quantum speed limit time for transporting over a single lattice site is exactly given by the harmonic oscillator period:

$$\boxed{T_{\mathrm{qsl}}\big|_{d=a_{\mathrm{dt}}} = T_{\mathrm{ho}} = \sqrt{\frac{M\,\lambda_{\mathrm{dt}}^2}{2\,U_0}}}\,. \tag{4.30}$$

The numerically obtained speed limits for experimentally reasonable trap depths as well as the data points for much deeper lattices all nearly perfectly coincide with this model.

Scaling for longer transport distances

The dependency of the quantum speed limit on the transport distance is shown in figure 4.11b for a trap depth of $U_0 = 80\,\mu\mathrm{K} \times k_B$. The numerically calculated data nearly perfectly agrees with the simple model

$$\boxed{T_{\mathrm{qsl}} = T_{\mathrm{ho}} \sqrt{\frac{d}{a_{\mathrm{dt}}}}} \tag{4.31}$$

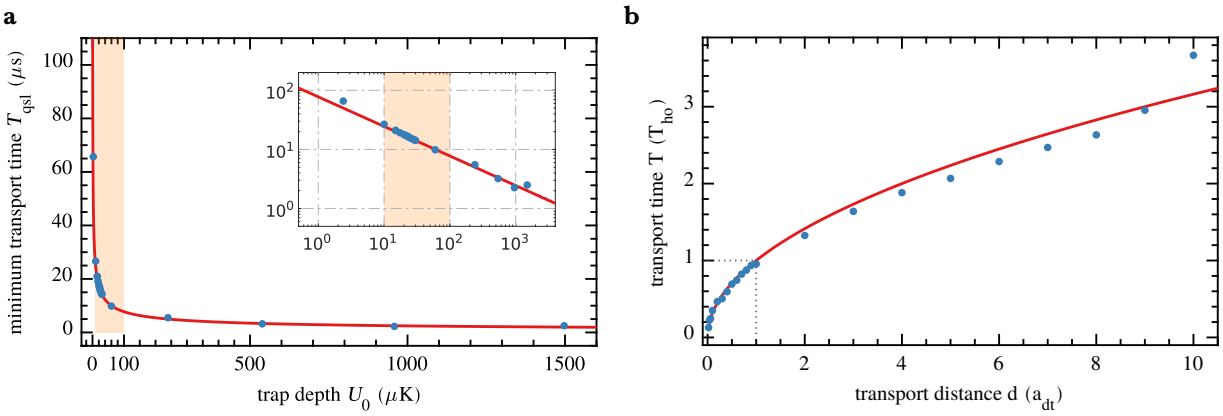

Fig. 4.11: Trap depth (a) and transport distance dependency (b) of the quantum speed limit as extracted from numerical optimization. For the scan of the trap depth dependency the transport distance is fixed at $d = a_{\mathrm{dt}}$, while when varying the transport distance we set $U_0 = 80\,\mu\mathrm{K} \times k_B$.

with T_{ho} the harmonic oscillator period. This scaling behavior could also be verified for a broad range of different trap depths. The square-root scaling shows the strong benefit of the optimal control solutions over an adiabatic approach, which naturally is expected to scale linearly in the transport distance. For the case of a driven harmonic oscillator, the adiabaticity condition reads $\left|\dot{x}_0(t)\sqrt{M\,/\,(2\,\hbar\,\omega_{\mathrm{ho}})}\right| \leq 1$ [116], which gives the expected scaling for the minimum time $T_{\mathrm{min}}^{(ad)} = d\sqrt{M\,/\,(2\,\hbar\,\omega_{\mathrm{ho}})}$.

A similar square-root dependency of the quantum speed limit for both trap depth and transport distance was found for the transport of single atoms in optical tweezers as numerically analyzed by Sels [38]. An identical scaling behavior could also be identified by considering a harmonic oscillator subject to anharmonicities in form of a quartic distortion [116]. By constraining the absolute distance between the trap position $x_0(t)$ and the classical particle trajectory $x_{\mathrm{cl}}(t)$ to a finite value, δ, Zhang et. al. showed that an inverse engineering approach based on a Lewis-Riesenfeld invariant optimal control solution minimizes the anharmonic contributions to the particles mean energy for transport times[1]

$$T \geq T_{\mathrm{min}}^{(ZB)} \equiv \frac{2}{\omega_{\mathrm{ho}}}\sqrt{\frac{d}{\delta}} = \frac{T_{\mathrm{ho}}}{\pi}\sqrt{\frac{d}{\delta}}\,. \tag{4.32}$$

Allowing trap depth modulation

When also allowing for trap depth modulations during the transport sequence, the minimum time can strongly undercut the quantum speed limit of the transport sequence at constant depth. Figure 4.12a shows the results of an optimization for an initial and final trap depth of $15\,\mu\mathrm{K} \times k_B$ allowing trap depth variations between $U_0^{(\mathrm{min})} = 5\,\mu\mathrm{K} \times k_B$ and up to $U_0^{(\mathrm{max})} = 300\,\mu\mathrm{K} \times k_B$. While the optimal control solutions for long times show only slight changes in the trap depth – the constant depth approach still allows high fidelities –, solutions for short times show strong modulations especially at the initial and final time of the transport sequence, as shown for transport sequence at $T = 5\,\mu\mathrm{s}$ in figure 4.12b. We can furthermore identify the symmetry of the trap depth trajectory as predicted in section 4.3.3. The initial increase in trap depth confines the atomic wave function strongly and the anharmonic contributions to the dynamical evolution can therefore be almost neglected. Allowing the trap depth to increase furthermore could theoretically make the possible minimum time infinitely small. However this scheme does not require the trap depth to be always constant at its maximum allowed value during the transport sequence. While the optimal control transport sequence at fixed $U_0 = 300\,\mu\mathrm{K} \times k_B$ promises a minimum transport time at about half of the here predicted time ($T_{\mathrm{min}} \approx 9.4\,\mu\mathrm{s}$), the here derived solution amounts in comparison just to $\approx 40\,\%$ of integrated laser

[1] We were however unable to apply the suggested transport sequences to our system, since both the trajectory of the classical particle trajectory and therefore also the trap trajectory given in equation (27) and (28) in reference [116] are complex valued for times $t \in [0, T]$.

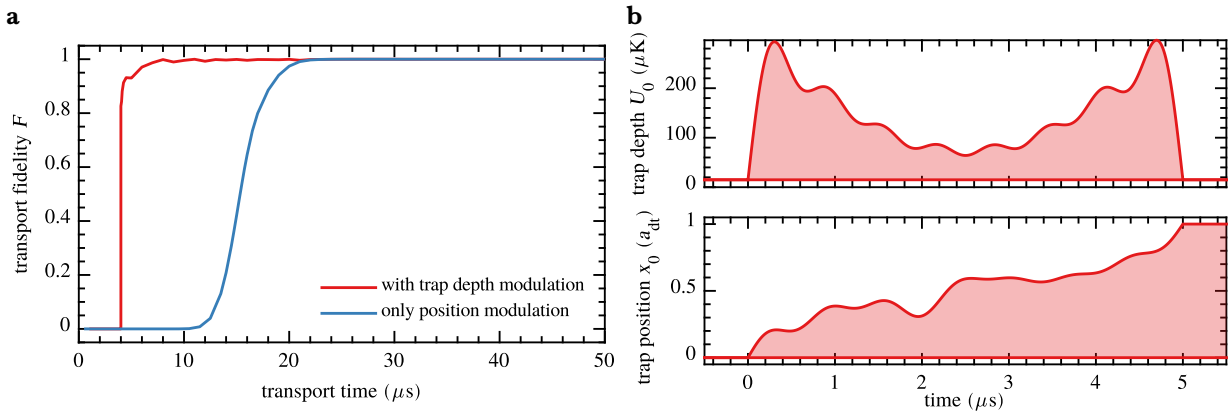

Fig. 4.12: Reachable optimal control transport times (red line) when allowing for (reasonable) trap depth modulation (a). The initial and final trap depth is fixed at $15\,\mu\mathrm{K} \times k_B$ and the optimization algorithm is allowed to increase it to $300\,\mu\mathrm{K} \times k_B$ during the transport sequence. The blue line shows the optimal control fidelity for a fixed trap depth of $U_0 = 15\,\mu\mathrm{K} \times k_B$. The speed limits are given by $9.4\,\mu\mathrm{s}$ with and $20.9\,\mu\mathrm{s}$ without allowed trap depth modulation. The transport ramp at $T = 5\,\mu\mathrm{s}$ reaching a transport fidelity of $93.02\,\%$ is shown in (b).

power and therefore would reduce the amount of scattered photons and the associated decoherence rate. The comparison to the constant depth optimization however also indicates the limitation of this optimization ansatz. With just $N_U = 15$ Fourier components for the amplitude modulation and a constant initial guess, the optimization algorithm is also not able to increase the trap depth to the maximum value for the whole transport time, which probably lets it miss high-fidelity solutions with even lower transport times. A more rigorous analysis of trap depth modulated optimal control transport will be task of future research. For this, we suggest to implement the integrated photon scattering rate as a direct constraint to the optimization problem.

4.4.2 Experimental results

To test the quantum speed limit experimentally we choose a relatively low trap depth, so that the transport times close to the limit do not exceed the limits of our phase lock loop electronics. Given a fixed laser power the trap depth is determined by fitting a sideband-resolved microwave spectrum taking into account the anharmonicities of the lattice potential as shown in section 3.2.2. We obtain $U_0 = (27.7 \pm 0.5)\,\%$. An numerical optimization using the decreasing time approach provides with the expected fidelity curves and corresponding transport sequences. To be able to execute the transport ramps experimentally the optimization is constrained in the slope of the trap position as explained before and the ramps are optically optimized by employing our iterative error correction and deconvolution scheme. The finally optimized transport trajectory is detected by a quadrature measurement and saved for the later analysis. By employing our motional state detection scheme before and after the transport provides us with the baseline and sideband height for each individual transport sequence and transport time. The raw data is shown in figure 4.13. Both the drop in the sideband height as well as the drop in the baseline – which is mainly induced by the reduced survival – indicate the speed limit close to the expected boundary. The transport survival as well as the from sideband and baseline height extracted transport fidelity is shown in figure 4.14 together with the simulated, expected fidelity of both the constraint as well as unconstrained optimal control solution. We additionally simulated the optically measured transport sequence and extracted the corresponding transport fidelity, which cleary indicates the performance of our optical feedback correction. We can furthermore observe a good accordance of the data for most of the times. However we find a big deviation for really short times and a drop of fidelity close to the quantum speed limit, which is much stronger than the expected drop due to the constrained optimization. The estimated minimum time (for $\mathcal{F} \geq 0.99$) of $20.5\,\mu\mathrm{s}$ is therefore much longer than the theoretical expectation.

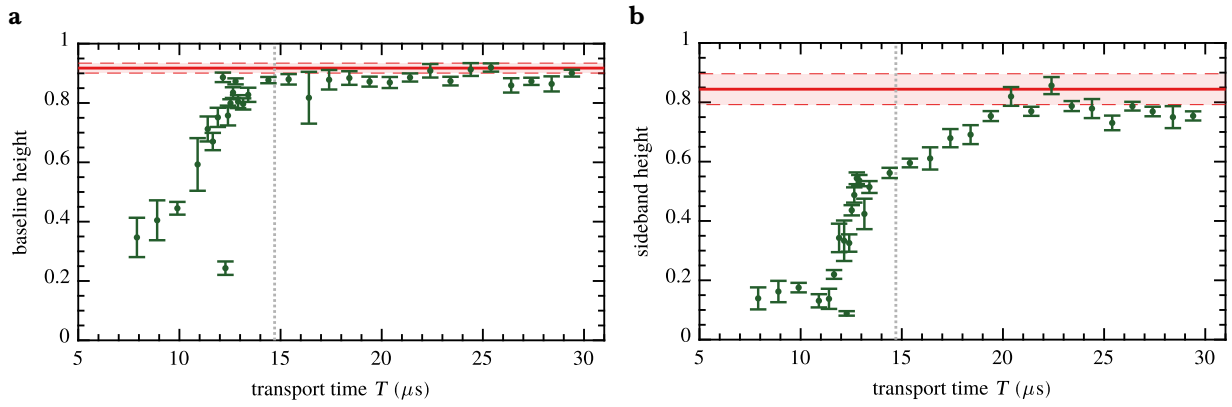

Fig. 4.13: Baseline (a) and sideband height (b) measured by employing the motional state detection scheme after transporting the atoms along optimal control trajectories quantum speed limit. The red solid line indicates the respective value obtained before the transport sequence and the dashed line shows the harmonic oscillator period.

Trap depth deviation

The deviation between experimentally detected and theoretically expected transport fidelity close to the quantum speed limit can be easily explained by an unexpected trap depth change. A correction from $U_0 = 27.7\,\mu\text{K} \times k_B$ to $25\,\mu\text{K} \times k_B$ for the simulated transport fidelity, as shown in figure 4.15a, shows a much better accordance.

Unfortunately we experience these drifts over hours and especially between day and night time, which makes it hard to precisely measure the trap depth by means of microwave sideband spectroscopy or by fitting a bang-bang transport time scan, to then calculate the corresponding optimal control ramps for probing the quantum speed limit and finally detecting the transport fidelities by means of motional state tomography without observing a trap depth change over time. The here shown data is just one out of multiple attempts, where we seemed to struggle in detecting the correct trap frequency. We can not exclude thermal drifts of our optics, but suspect the power meter used for calibrating the intensity of the dipole trap arms to malfunction and therefore replaced it with a high quality photo diode recently. A rigorous elimination of these drifts is the most important step for future experiments.

From our numerical and also experimental analysis of multiple optimal control transport sequences we conclude that the optimal control ramps are generally robust against small deviations in the trajectories and strongly robust against experimental noise, as shown before. The relatively strong sensitivity to small trap depth changes for some of the optimal control transport ramps could be practically removed by varying the trap depth and looking for more robust optimal control solutions also accepting slightly longer transport times as a trade-off. Since the optimal control landscape provides us with a large number of optimal solutions, an adapted optimization algorithm like ROME [117] which under user defined criteria directly attempts to find the robust solutions might speed up this process. An analytic approach for finding these protocols robust against trap frequency fluctuations is presented in [85] for the case of a perfect harmonic oscillator.

Sideband shift

As we already saw in section 3.2.2 the anharmonic potential can induce sideband shifts when populating higher motional levels. While due to the flattening of the sidebands induced by the repeated microwave and pushout application, the new motional state detection scheme is much more robust against small shifts compared to the standard sideband spectroscopy, transport ramps with a transport fidelity $\mathcal{F}_{0\to0}$ close to zero however strongly excite the atoms to high vibrational levels. Even though our motional state detection scheme measuring just at a fixed frequency is relatively fast compared to a full

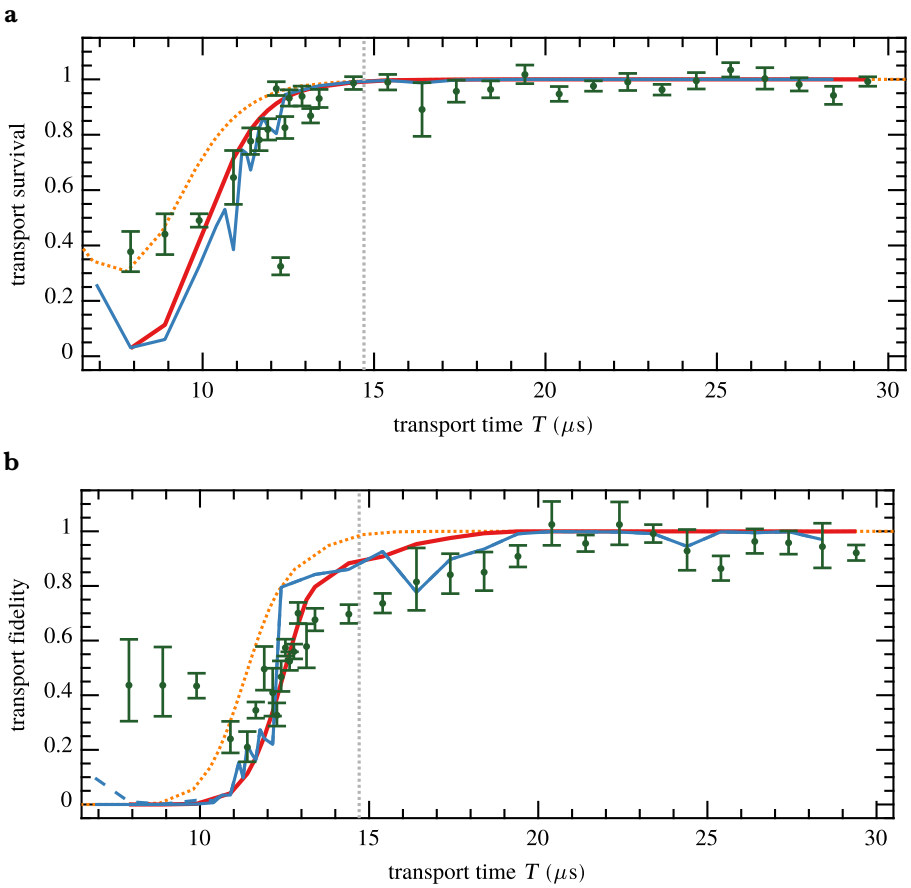

Fig. 4.14: Experimentally measured quantum speed limit shown by the transport survival (a) and transport fidelity (b). The dashed gray line indicates the theoretically expected quantum speed limit, the red line the unconstrained and the orange, dotted line the constraint optimization results. Together with the optically measured and simulated transport fidelity (blue, solid) we also show the sum of simulated ground state populations for all simulated lattice sites, which therefore takes into account the super fast transport sequences which might leave part of the wave packet remain in the initial lattice site. However the small correction does not explain the strong sideband increase for transport times around $T = 9\,\mu s$.

spectrum, we detect too high sidebands for really fast transport sequences, as we can clearly confirm from our measurement as shown in figure 4.13b. To avoid this problem we already implemented a new scheme, were we do not only measure at a fixed microwave frequency ν but scan the microwave around the expected sideband position preferring frequencies closer to the carrier. By either taking just the minimum point or extracting the minimum from a simple fit, we should be able to precisely measure also the motional state populations for really strong excitations. Due to technical problems in the lab the data shown in this thesis however was taken before we were able to fully apply this adapted method. We can however correct our data qualitatively by a phenomenological model. If we measure the sideband height S_{meas} at frequency $\nu_{\text{meas}} = \nu_{1\to0}$ and if we assume that the real sideband position is approximately given by the weighted sum $\nu_{\text{real}} = \sum_{n=0}^{N-1} p_n \nu_{n\to n-1}$, where p_n are the motional state populations, we can approximate the spectrum $S(\nu)$ around ν_{real} as an inverted generalized normal distribution with baseline $B \leq 1$ and width σ and therefore write

$$S(\nu_{\text{meas}}) = B - (B - S_{\text{real}}) \exp\left[-\left(\frac{|\nu_{\text{meas}} - \nu_{\text{real}}|}{|\sqrt{2}\,\sigma|}\right)^{\beta}\right] = S_{\text{meas}}\,, \tag{4.33}$$

where $\beta = 2$ would correspond to $N_{\text{mst}} = 1$ and a therefore Gaussian distribution and $\beta > 2$ mimics the flattening for higher N_{mst}. A least square fit of the first red sideband shown in figure 3.5a gives

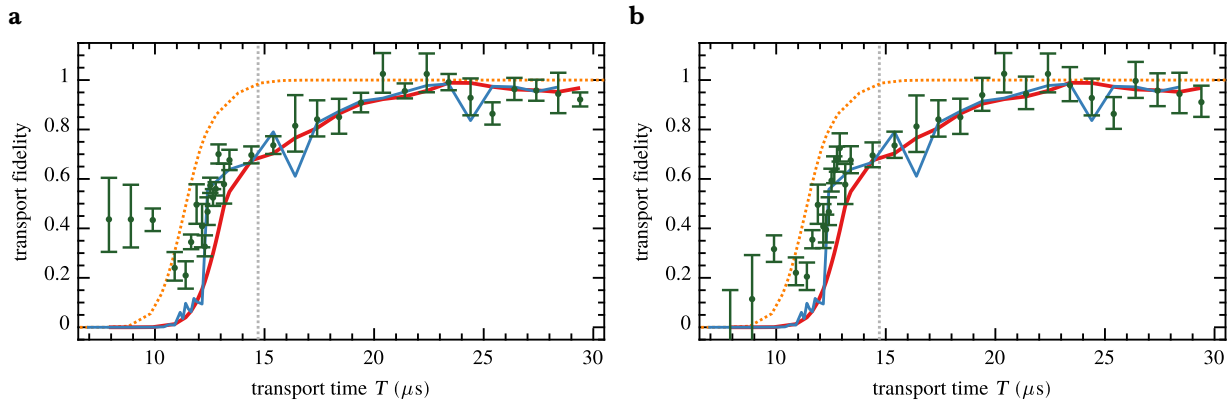

Fig. 4.15: Experimentally measured and corrected transport fidelity close to the quantum speed limit, indicated by a gray dashed line. (a) shows the effect to the numerically obtained expectation of a trap depth correction from $U_0 = 27.7\,\mu\text{K} \times k_B$ to $25\,\mu\text{K} \times k_B$ and (b) indicates both the trap depth as well as the sideband height change, which is induced by the anharmonic spacing of the energy levels of the lattice potential.

$\beta = 4.2 \pm 0.3$ and $\sigma = (18.4 \pm 0.3)\,\text{kHz}$. By estimating the motional state populations p_n and transition frequencies from the numerical quantum simulation, we can estimate qualitatively the shift induced sideband height change, as shown in figure 4.15b, which only shows minor correction for our high-fidelity transport sequences, but effectively brings the estimated transport fidelities for transport times $\leq 10\,\mu\text{s}$ closer to the theoretical expectation.

4.4.3 Theoretical bounds

The mathematical description of the quantum speed limit for any quantum system always rely on the the choice of a measure of distinguishability of quantum states, like the Bures angle [118], the quantum Fisher information [111] or even measures related to the quantum coherence [110]. This finally enables to relate the fundamental time-energy uncertainty relation to a minimum time by using some kind of triangle inequality for the selected measure – like the Cauchy-Schwarz inequality –, which however only allows to give a lower bound for the quantum speed limit and not the fundamental tight bound itself. Recent investigations [39] promise to have generalized these measures by considering the Schatten p-norm of the generator of quantum dynamics, $(\text{tr}(|\dot{\rho}|^p))^{1/p}$, and therefore predict a universal generalization of the quantum speed for any quantum dynamics. A rigorous analysis and prediction of the tight quantum speed limit bound would go beyond the scope of this study. We will focus our analysis here on the bound predicted by Margolus, Levitin, Mandelstam and Tamm.

Mandelstam-Tamm & Margolus-Levitin bound

The first rigorous analysis of the quantum speed limit was provided by Igor Tamm together with his supervisor Leonid Mandelstam in 1991 [108]. They showed that the minimal time for evolving between orthogonal states is bounded from below by the variance of the energy, $\Delta E = \sqrt{\langle H^2 \rangle - \langle H \rangle^2}$:

$$T_{\text{qsl}} \geq T_{\text{min}}^{(MT)} \equiv \frac{\pi\,\hbar}{2\,\Delta E}\,. \tag{4.34}$$

Since the variance of an operator is generally not viewed as a precise measure of quantum uncertainty [119, 120], Margolus and Levitin derived a second lower bound for the quantum speed limit in 1998 [121]:

$$T_{\text{qsl}} \geq T_{\text{min}}^{(ML)} \equiv \frac{\pi\,\hbar}{2\,\bar{E}}\,, \tag{4.35}$$

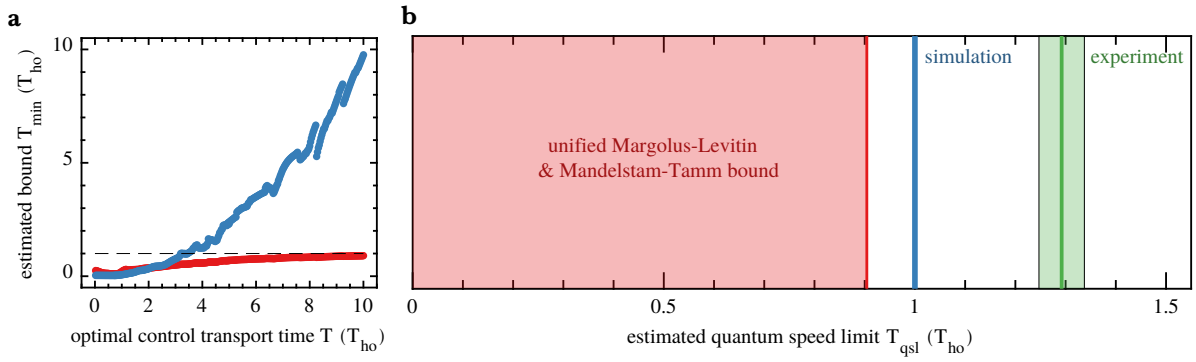

Fig. 4.16: Mandelstam-Tamm (blue dots) & Margolus-Levitin (red dots) bound for the quantum speed limit extracted from numerically computed optimal control sequences at a trap depth of $U_0 = 25\,\mu\mathrm{K} \times k_B$ (a). The different transport times T give rise to differences in energy spread and mean energy. The maximum of the unified bound (red line) together with the quantum speed limits obtained from the numerical simulation (blue) as well as the experimental one (green) is shown in (b). The experimental speed limit is obtained from the minimum time for which the transport fidelity curve in figure 4.15b exceeds $\mathcal{F} \geq 99\,\%$.

which is based on the average energy, $\bar{E} = \langle H \rangle - E_0$, with respect to the ground state energy E_0. Later Levitin furthermore showed [122] that these two bounds are not independent of each other and therefore only the unified bound,

$$\boxed{T_{\mathrm{qsl}} \geq \min\left(T_{\mathrm{min}}^{(MT)}, T_{\mathrm{min}}^{(ML)}\right) = \min\left(\frac{\pi\,\hbar}{2\,\Delta E}, \frac{\pi\,\hbar}{2\,\bar{E}}\right)}, \tag{4.36}$$

is tight.

Numerical estimation of the bound

We like to estimate this unified bound for our quantum optimal control problem. Since both the average energy as well as the energy variance depends through the time average $\langle\,.\,\rangle = (1/T)\int_0^T \mathrm{d}\,t\ \langle\psi(t)|\,.\,|\psi(t)\rangle$ on the time evolution of the wave function and there is no exact analytical solution to the time-dependent Schrödinger equation, we estimate the bounds using our numerical quantum simulation. Since the limit is most tight for maximum energy spread or average energy respectively, we calculate the time average along optimal control solutions close to the quantum speed limit. For a trap depth of $U_0 = 25\,\mu\mathrm{K} \times k_B$ we obtain the results shown in figure 4.16. The comparison to the numerically and experimentally obtained speed limits shows a good agreement. However the theoretical bound still lies about $0.1\,T_{\mathrm{ho}}$ below the speed limit obtained from our optimal control approach. A more rigorous analysis of this deviation answering the question whether the here estimated bound is tight, should be focus of future analysis.

Outlook

By letting an numerical optimization algorithm optimize both the spatial trajectory of the optical lattice potential in an open loop, where a computer simulation is judging the fidelity, we could identify and experimentally confirm fast high-fidelity transport sequences which prevent any motional excitation. Optimal control sequences allowing single site transport of atoms in the oscillation period of the trapping potential are believed to reach the fundamental quantum speed limit of our system.

On the road we were able to successfully exploit the limits of our electro-optical feedback control system. With the help of the newly developed deconvolution routine and being now able to extract the transport trajectories optically by a component measurement, we were able to successfully overdrive the lock electronics in a controlled and reproducible way.

The here presented work enabled single-site transport sequences with transport times two to three times shorter than our previous used linear 'bang-bang´ transport scheme allowed, while keeping or even improving over its fidelity and it will therefore replace the 'working horse´ of future experiments. By also optimizing for robustness instead of just transport time, optimal control promises more stable and reliable atomic transport.

The identified transport sequences did not only touched the fundamental limits of the quantum system, but also the limits of our lock electronics and our numerical quantum simulation and optimization. To solve the problem of limited computation power a proposal for an alternative, closed-loop optimization approach and preliminary experimental results are presented in section O.1. The speed limits of the lock electronic will be solved in the future by implementing a feed-forward control scheme on a new controller based on a field-programmable gate array, which we introduce in section O.2.

O.1 Live feedback optimization

The numerical approach for solving the the time-dependent Schrödinger equation over long distances takes a lot of computational effort [90]. The calculation of the quantum speed limit for $d = 10\, a_{\mathrm{dt}}$ for instance – as shown in figure 4.11b – took about two full days of computation while stressing out all four cores on a consumer desktop CPU[1]. Since we are interested in even higher transport distances up to 50 to 100 lattice sites for atomic interferometer applications, this is a rather inconvenient setup. Allowing the numerically calculated position grid to move with the position of the wave function, as used in [36], would provide less computational effort for long distance transport simulation, but also requires extra care on the optimization strategy, since the optimal control attempts have to be constraint to trajectories, which do not spread the atomic wave function over the limits of the reduced size grid.

The approach of letting a computer simulate and optimize the transport sequences, which are then tested experimentally can be categorized as an open loop approach. It fully relies on the agreement between experiment and numerical quantum simulation, the latter being based on a major simplification of the problem. Even though optimal control solutions are in general robust against noise and small imperfections, the open loop optimization scheme is limited by these discrepancies. A closed loop optimization approach, were we directly connect experimental apparatus and optimization algorithm has direct access to the real quantum system and therefore would allow the experimental apparatus to

[1] Intel i5-7400 at a clock speed of 3.0 GHz.

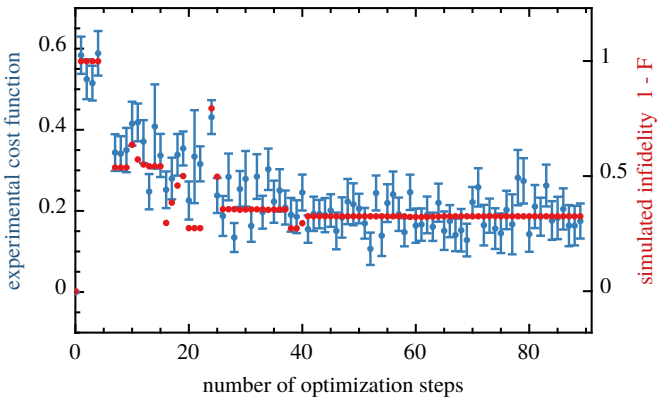

Fig. 5.1: Preliminary results on open loop live feedback optimization. The experimental cost function is a weighted sum of the transport survival and the sideband heights detected by the basic microwave sideband spectroscopy method as introduced in section 3.2. More details can be found in [68].

optimize itself. In the context of optimal control this live feedback optimization strategy was already successfully applied in different fields reaching from improving driving of molecular dynamics using femtosecond laser pulses [123] to engineering quantum phase transitions of ultracold atomic clouds in optical lattices [97].

The preliminary results of a closed loop optimization of optimal control transport sequences using our experimental apparatus are shown in figure 5.1. Starting from a linear ramp of the lattice position we optimized the transport by optimizing only the first two Fourier components of the discrete Fourier approach, equation (4.16), for a transport time of $T = 12\,\mu s$ at a trap depth of $80\,\mu K$. From the evolution of the experimental cost function, which is in good accordance to the simulated infidelity, we can clearly detect an improvement of the transport fidelity. It however saturated at only $\mathcal{F} \approx 70\,\%$ where the optimization algorithm then stopped being unable to detect a gradient in the optimization landscape for the defined step size. The open loop optimization in comparison could reach a transport fidelity of $99.8\,\%$. Additionally, while the experimental sequence consisting of atom loading, state preparation, transport and detection takes only a few hundred milliseconds, the required repetitions to obtain enough statistics for detecting small changes in the transport fidelity and especially the time overhead for programming the transport ramps onto mBed and DDS increase the necessary time to perform a single optimization step to tens of minutes. This currently limits the optimization to just a few tunable parameters and therefore also drastically decreases the solution space.

To overcome this limit from the numerical standpoint, we propose the application of a chopped random basis (CRAB) approach [93], which effectively increase the optimization landscape by randomizing the Fourier basis frequencies. This breaks the orthogonality of the basis elements and therefore allows not only to generate arbitrary frequencies out of just a few optimization parameters like a truncated Fourier basis, but also allows to efficiently escape from constraint induced local, but not global extrema in the optimization landscape similarly to the approach used in simulated annealing. Lately the CRAB algorithm was also successfully dressed to handle optimization problems with a finite bandwidth [94].

In cooperation with the group around Professor Tommaso Calarco and Professor Simone Montangero we recently implemented a link between our experimental apparatus and a dressed and constraint version of the CRAB optimization algorithm running on a server in Ulm and are currently working on the first experimental tests.

O.2 Feed-forward control using a field programmable gate array

We successfully improved the current semi-digital feedback control system used for steering both intensity and phase of the optical lattice beams for the application of fast high-fidelity single atom

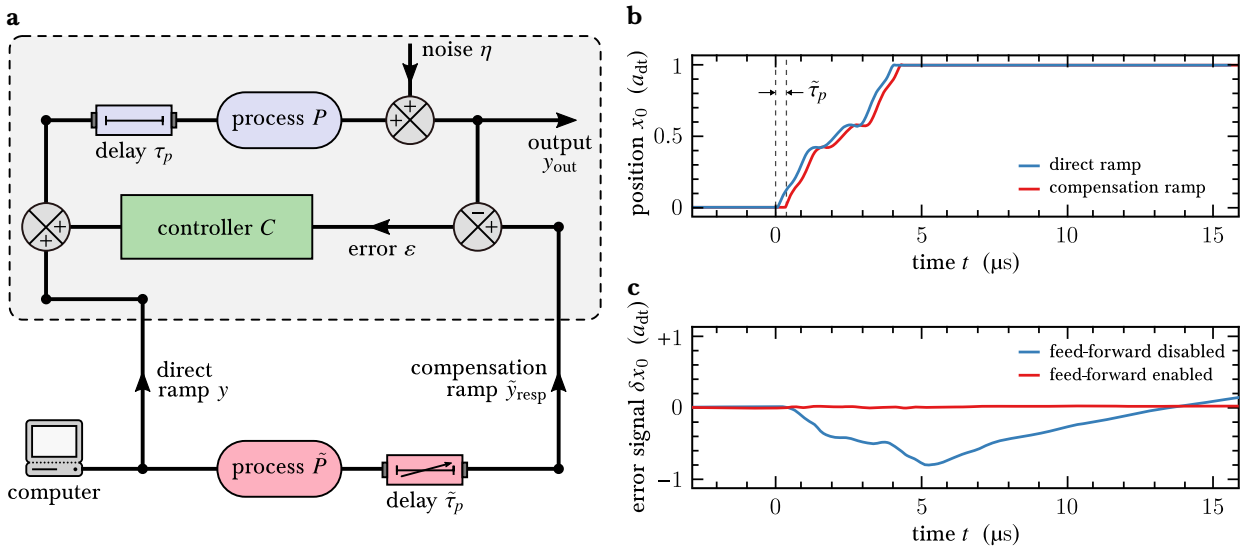

Fig. 5.2: Feed-forward feedback control principle (a) and its application for the execution of fast transport sequences (b), (c). The control signal y is applied directly to the process P with intrinsic delay τ_p whose output y_{out} is controlled via feeding back an error signal ε to a PID controller C. By additionally applying a compensation ramp $\tilde{y}_{\text{resp}}$ to the set-point of the controller, which is derived from a mathematical model $\tilde{P}$ of the process dynamics P and delayed by time $\tilde{\tau}_p$, the error signal ϵ is suppressed. When applying this scheme to a optimal control transport sequence, the control signal y is given by the lattice shift $x_0(t)$ and the error signal ε can be phrased as as discrepancy $\delta x_0(t)$. More details on the feed-forward implementation can be found in [54].

transport. To allow transport times down to a few microseconds the feedback control system used for steering depth and position of the optical lattice deterministically was strongly overdriven and the control transport schemes therefore explored the limits of the current feedback control systems.

Feedforward control

The performance of traditional control schemes is in general limited drastically by the system delay time, meaning the time in which a setpoint change at the controller shows an effect on the system. So called feed-forward control schemes can utilize the fact that system response is usually well known and therefore can be simulated and corrected in real time. It bypasses the traditional error-based adjustment response of the lock electronics by replacing it with knowledge about the system's response itself based on a mathematical model of the process, as illustrated in figure 5.2a. Hence, this internal model control approach effectively removes the system delay when changing the setpoint by tuning the controller.

FPGA-based PID lock

Simulating and compensating for the system response demands for a more complex, but also flexible control feedback setup, which is hard to achieve using feedback controllers based on analog electronics. High-speed digital signal processing can be achieved by use of field-programmable gate arrays (FPGA), which allow designing an integrated circuit by connecting programmable logic blocks by means of software engineering.

Being already reliable used in our second experimental setup in Bonn, we bought a Keysight M3300A arbitrary waveform generator (AWG) and digitizer combination, which, with the AWGs providing sample rates of $500\,\text{MS}\,\text{s}^{-1}$ and up to $16\,\text{Bit}$ of resolution should provide us with a perfect setup for fast modulation of the lattice parameters with an bandwidth up to $200\,\text{MHz}$. With a input to output latency of less then $400\,\text{ns}$ using the included analog to digital converter and the possibility to implement a variety of circuits using the onboard digital synthesizer processor (DSP) cores, we

already showed that we can fully replace our analog PID lock setup by a complete digital version. A full characterization of the new setup showing the high performance increase can be found in [54].

As we identified from our numerical optimization, also allowing reasonable trap depth variations during transport can lower the transport time much further. The implementation of a feed-forward control scheme based on internal model control controlling both trap depth and position of our optical lattice should improve the bandwidth of the feedback dramatically and allow even faster transport ramps with higher precision. The first result for enabling even faster optimal control transport sequences is shown in figure 5.2b and (c), where we executed of a numerically calculated optimal control sequence for $T = 4\,\mu s$ on our new FPGA-based controller unit and measured the resulting error signal. When enabling feed-forward by applying both a direct ramp to the AOM, as well as a compensation ramp to the controller, which simulates the system's response, a fine-tuning of the relative delay allows to suppress the error signal completely. The compensation ramp is obtained by time-shifting the convolution of the desired transport ramp with the AOM impulse response function, which has the form of a Gaussian, as shown in section 2.1.1.

The change to a FPGA based controller unit also removes the unnecessary time overhead in the programming of transport ramps and therefore is an important step to allow closed loop live feedback optimization. The new system already allowed state-dependent transport in our two-dimensional state-dependent lattice setup [10] and recent investigations on an additional linearization of the amplitude lock response using an onboard lookup table were promising, so that we plan to replace the current electronic lock circuit of our one-dimensional lattice setup in the next months.

Appendix

A.1 The ac Stark effect

Consider a many level atom with energy eigenstates $\{|k\rangle\}$ interacting with a classical light field $\boldsymbol{E}(t) = \hat{\boldsymbol{\epsilon}}\, E_0 \cos\omega t$ at the position of the atom $\boldsymbol{x} = 0$, which is assumed to be fixed in time or at least very slowly varying on the relevant timescale given by ω. The Hamiltonian reads

$$\mathscr{H}(t) = \mathscr{H}_0 + \mathscr{H}_{\text{int}}(t) = \mathscr{H}_0 - \boldsymbol{\mu} \cdot \boldsymbol{E}(t), \tag{6.1}$$

where the unperturbed Hamiltonian $\mathscr{H}_0$ defines the eigenenergies $\mathscr{H}_0 |k\rangle = \hbar\omega_k$. We expand the quantum state with respect to the unperturbed energy eigenstates $|\psi(t)\rangle = \sum_k a_k(t)\, \mathrm{e}^{-\mathrm{i}\omega_k t} |k\rangle$ and assume that the atom is initially in a ground state $|\psi(0)\rangle = |i\rangle$. To obtain the energy shift due to the interaction, we can now use time-dependent perturbation theory [Q] to expand the ground state coefficient in orders of $\mathscr{H}_{\text{int}}$:

$$a_i(t) = a_i^{(0)}(t) + a_i^{(1)}(t) + a_i^{(2)}(t) + \dots \tag{6.2}$$

$$= 1 - \frac{\mathrm{i}}{\hbar}\int_0^t \mathrm{d}t' H_{ii}(t') - \frac{1}{\hbar^2}\sum_k \int_0^t \mathrm{d}t' \int_0^t \mathrm{d}t'' \mathrm{e}^{\mathrm{i}(\omega_{ik}t' + \omega_{ki}t'')} H_{ik}(t') H_{ki}(t'') + \dots, \tag{6.3}$$

where $H_{kl}(t) = \langle k| \mathscr{H}_{\text{int}}(t) |l\rangle$ and $\omega_{kl} = \omega_k - \omega_l$. Due to symmetry arguments the first order correction vanishes $H_{ii}(t) = -\langle i| \boldsymbol{\mu} \cdot \boldsymbol{E}(t) |i\rangle = e \sum_n \langle i| \boldsymbol{r_n} |i\rangle \cdot \boldsymbol{E}(t) = 0$, where $\boldsymbol{r_n}$ are the electron positions. The second order contribution can be simplified to

$$a_i^{(2)}(t) = -\frac{E_0^2}{4\hbar^2} \sum_k \frac{|\langle k| \boldsymbol{\mu} |i\rangle \cdot \boldsymbol{E}(t)|^2}{\omega_{ki} - \omega} \left(\frac{1 - \mathrm{e}^{-\mathrm{i}\omega_{ki}t}}{\omega_{ki}} - \frac{1 - \mathrm{e}^{-\mathrm{i}\omega t}}{\omega} \right). \tag{6.4}$$

Here we assumed ω to be near resonant with the transition frequencies ω_{ji} and used the rotating wave approximation to ignore fast oscillating terms $\sim e^{\mathrm{i}(\omega+\omega_{ki})}$. We now assume that the perturbation is small so that $|a_i(t)| \approx 1$ for all times t and therefore write $a_i(t) = \mathrm{e}^{\mathrm{i}\phi(t)}$. This allows approximating $|\psi(t)\rangle \approx \mathrm{e}^{-\mathrm{i}(\phi(t) - \omega_i t)} |i\rangle \approx \mathrm{e}^{-\mathrm{i}(\langle \dot{\phi}(t)\rangle_t - \omega_i)t} |i\rangle$, where $\left\langle \dot{\phi}(t) \right\rangle_t$ denotes the time average of $\partial_t \phi(t)$ over one period $t \in [0, 2\pi/\omega)$. The ac Stark shift of the ground state energy $\hbar\omega_i$ can then be written as

$$\Delta E_{|i\rangle,\text{ac Stark}} = -\hbar \left\langle \dot{\phi}(t) \right\rangle_t \tag{6.5}$$

$$= \mathrm{i}\hbar \langle \partial_t \log a_i(t) \rangle_t = \mathrm{i}\hbar \log a_i(2\pi/\omega) \tag{6.6}$$

$$= \frac{E_0^2}{4\hbar} \sum_k \frac{|\langle k| \boldsymbol{\mu} |i\rangle \cdot \boldsymbol{\epsilon}|^2}{\omega - \omega_{ki}}, \tag{6.7}$$

where in the last step we made use of a series expansion around $\omega_{ki}/\omega \sim 1$ to first order.

A.2 Dipole trap crosstalk

Potential seen by state $|\downarrow\rangle$

We like to express the dipole trap potential seen by spin state $|\downarrow\rangle$ as a sinusodial potential with a global energy offset. Therefore we want to solve

$$\begin{aligned} U^{\downarrow}(\boldsymbol{x}) &= \left\{-\frac{7}{8}U_0^- \cos^2\left[k_{\mathrm{dt}}(x-x_0^-)\right] - \frac{1}{8}U_0^+ \cos^2\left[k_{\mathrm{dt}}(x-x_0^+)\right]\right\} \mathrm{e}^{-2\rho^2/w_{\mathrm{dt}}^2} \\ &= \left\{\delta U^{\downarrow} - U_0^{\downarrow}\cos^2\left[k_{\mathrm{dt}}(x-x_0^{\downarrow})\right]\right\} \mathrm{e}^{-2\rho^2/w_{\mathrm{dt}}^2} \end{aligned} \tag{6.8}$$

for $U_0^{\downarrow}$, $x_0^{\downarrow}$ and $\delta U^{\downarrow}$ in depency of x_0^+ and x_0^-. When canceling out the radial dependency by setting $\rho = 0$ and by writing $\cos^2(\alpha) = \frac{1}{2}\left[\cos(2\alpha) - 1\right]$ we obtain

$$\begin{aligned} &U_0^{\downarrow}\cos\left[2k_{\mathrm{dt}}(x-x_0^{\downarrow})\right] - \frac{7}{8}U_0^-\cos\left[2k_{\mathrm{dt}}(x-x_0^-)\right] - \frac{1}{8}U_0^+\cos\left[2k_{\mathrm{dt}}(x-x_0^+)\right] \\ &= 2\delta\, U^{\downarrow} + \frac{7}{8}U_0^- + \frac{1}{8}U_0^+ - 2\,U_0^{\downarrow}\,. \end{aligned} \tag{6.9}$$

Since this equation should hold true for all x, we now evaluate it at $x = 0$, $x = a_{\mathrm{dt}}/2$ and at $x = a_{\mathrm{dt}}/4$ and get

$$U_0^{\downarrow}\cos\left[2k_{\mathrm{dt}}x_0^{\downarrow}\right] - c^{\pm} = 2\delta\, U^{\downarrow} - U_0^{\downarrow} + \frac{7}{8}U_0^- + \frac{1}{8}U_0^+\,, \tag{6.10}$$

$$-U_0^{\downarrow}\cos\left[2k_{\mathrm{dt}}x_0^{\downarrow}\right] + c^{\pm} = 2\delta\, U^{\downarrow} - U_0^{\downarrow} + \frac{7}{8}U_0^- + \frac{1}{8}U_0^+\,, \tag{6.11}$$

$$U_0^{\downarrow}\sin\left[2k_{\mathrm{dt}}x_0^{\downarrow}\right] - s^{\pm} = 2\delta\, U^{\downarrow} - U_0^{\downarrow} + \frac{7}{8}U_0^- + \frac{1}{8}U_0^+\,, \tag{6.12}$$

where $s^{\pm}$ and $c^{\pm}$ are defined by equation 1.22. Adding (6.10) and (6.11) leads to

$$\boxed{\delta U^{\downarrow} = \frac{1}{2}\left(U_0^{\downarrow} - \frac{1}{8}U_0^+ - \frac{7}{8}U_0^-\right)}\,. \tag{6.13}$$

Equation (6.10) and (6.12) then become

$$U_0^{\downarrow}\cos\left[2k_{\mathrm{dt}}x_0^{\downarrow}\right] - c^{\pm} = 0\,, \tag{6.14}$$

$$U_0^{\downarrow}\sin\left[2k_{\mathrm{dt}}x_0^{\downarrow}\right] - s^{\pm} = 0\,. \tag{6.15}$$

Deviding (6.14) and (6.15) gives us

$$\boxed{x_0^{\downarrow} = \frac{a_{\mathrm{dt}}}{2\pi}\arctan\left[\frac{s^{\pm}}{c^{\pm}}\right]}\,. \tag{6.16}$$

Using the fact that $\cos(\arctan(\alpha)) = \left(1+\alpha^2\right)^{-1/2}$ and inserting (6.16) into (6.14) finally leads to

$$\boxed{U_0^{\downarrow} = \sqrt{s^{\pm 2} + c^{\pm 2}}}\,. \tag{6.17}$$

Crosstalk compensation

From equation 6.17 we obtain

$$0 = \left(U_0^-\right)^2 + \frac{2}{7}\,U_0^-\,U_0^+\cos\left[2k_{\mathrm{dt}}(x_0^+ - x_0^-)\right] + \left(\frac{1}{7}U_0^+\right)^2 - \left(\frac{8}{7}U_0^{\downarrow}\right)^2\,. \tag{6.18}$$

The solution for $U_0^- \geq 0$ reads

$$\boxed{U_0^- = \frac{1}{7}\left\{\sqrt{\left(8\,U_0^{\downarrow}\right)^2 - U_0^{+2}\sin^2\left[2k_{\mathrm{dt}}(x_0^+ - x_0^-)\right]} - U_0^+\,\cos\left[2k_{\mathrm{dt}}(x_0^+ - x_0^-)\right]\right\}}. \tag{6.19}$$

From equation (6.9) we obtain using (6.13):

$$\frac{7}{8}U_0^-\cos\left[2k_{\mathrm{dt}}(x - x_0^-)\right] + \frac{1}{8}U_0^+\cos\left[2k_{\mathrm{dt}}(x - x_0^+)\right] = U_0^{\downarrow}\cos\left[2k_{\mathrm{dt}}(x - x_0^{\downarrow})\right]. \tag{6.20}$$

Evaluating this equation at $x = x_0^{\downarrow} + a_{\mathrm{dt}}/4$ we get the final expression

$$\boxed{x_0^- = x_0^{\downarrow} + \frac{1}{2k_{\mathrm{dt}}}\arcsin\left\{\frac{U_0^+\sin\left[2\,k_{\mathrm{dt}}\,(x_0^{\downarrow} - x_0^+)\right]}{7\,U_0^-}\right\}}. \tag{6.21}$$

A.3 Transformation to a non-inertial reference frame

We consider a massive particle of mass M trapped in a potential $V(x - x_0(t))$ which moves along a trajectory $x_0(t)$ in time. We will further assume that the potential shows no direct time-dependency, $\partial_t\,V(x) = 0$, which would correspond to a constant trap depth of the optical lattice considered before. The associated time-dependent Hamiltonian is then given by

$$H(t) = \frac{p^2}{2\,M} + V\left(x - x_0(t)\right) \tag{6.22}$$

and defines the equation of motion, $-\mathrm{i}\,\hbar\,\partial_t\;|\psi(t)\rangle = H(t)\;|\psi(t)\rangle$, where $|\psi(t)\rangle$ is chosen to be the wave function describing the dynamical motion in the Schrödinger picture. We define this reference frame as the laboratory frame – the frame in which experimental observations, like detecting the atoms position by fluorescence imaging, take place.

The Lorentz transformation to a reference frame moving along a trajectory $x_{ref}(t)$,

$$\boxed{x \to x + x_{\mathrm{ref}}(t)} \tag{6.23}$$

with $x_{\mathrm{ref}}(t)$ being implicitly time-dependent, is in general non-trivial, since the associated unitary transformation is time-dependent and the transformation can violate the non-relativistic equivalence principle [124].

A general time-dependent unitary transformation $\mathrm{U}(t)$, which acts on the wave function as $|\psi(t)\rangle \to |\tilde{\psi}(t)\rangle = \mathrm{U}(t)\;|\psi(t)\rangle$ transforms the Hamiltonian as follows

$$H(t) \to \tilde{H}(t) = \mathrm{U}^{\dagger}(t)\,H(t)\,\mathrm{U}(t) - \mathrm{i}\,\hbar\,\mathrm{U}^{\dagger}(t)\,\frac{\partial}{\partial\,t}\mathrm{U}(t), \tag{6.24}$$

with $\tilde{H}(t)$ satisfying the transformed Schrödinger equation $-\mathrm{i}\,\hbar\partial_t\;|\tilde{\psi}(t)\rangle = \tilde{H}(t)\;|\tilde{\psi}(t)\rangle$. In a one-dimensional system, the Lorentz transformation associated to a position change $x \to x + \delta x$ for time independent δx is generated by the operator of momentum p and the respective unitary operator reads $\mathrm{T}(\delta x) = \exp\left(-\mathrm{i}\,\delta x\,p\,/\,\hbar\right)$. However, we also have to account for the momentum shift $p \to p + M\,\partial_t\,x_{\mathrm{ref}}(t)$, which the moving reference frame introduces. Analogously the generator of a momentum change $p \to p + \delta p$ is the position operator x and the unitary transformation is given by $\mathrm{K}(\delta p) = \exp\left(-\mathrm{i}\,\delta p\,x/\,\hbar\right)$ Since the two operator do not commute, $[x\;p] = \mathrm{i}\,\hbar$, when trying to phrase the transformation, which connects the two reference frames as a combination of a shift both in position and in momentum, we are confronted with the choice of ordering the two operators.

If we choose $\mathrm{U}(t) = \mathrm{e}^{-\mathrm{i}\,\gamma(t)/\hbar}\,\mathrm{K}[M\,\dot{x}_{\mathrm{ref}}(t)]\,\mathrm{T}[x_{\mathrm{ref}}(t)]$ with an additional arbitrary time-dependent and real phase $\gamma(t)$, whose choice is a Gauge freedom, a lengthy but straight-forward calculation yields the Hamiltonian in the moving frame

$$\tilde{H}(t) = \frac{p^2}{2\,M} + V\left[x + x_{\mathrm{ref}}(t) - x_0(t)\right] + M\,\ddot{x}_{\mathrm{ref}}(t)\,x - \left[\frac{1}{2}\,M\,\dot{x}^2_{\mathrm{ref}}(t) + \dot{\gamma}(t)\right]. \tag{6.25}$$

Here ‘˙’ and ‘¨’ denotes the first and second time derivative. Analogously by choosing the unitary operator for the transformation as $\mathrm{U}(t) = \mathrm{e}^{-\mathrm{i}\,\bar{\gamma}(t)/\hbar}\,\mathrm{T}[x_{\mathrm{ref}}(t)]\,\mathrm{K}[M\,\dot{x}_{\mathrm{ref}}(t)]$ the Hamiltonian becomes

$$\tilde{H}(t) = \frac{p^2}{2\,M} + V\left[x + x_{\mathrm{ref}}(t) - x_0(t)\right] + M\,\ddot{x}_{\mathrm{ref}}(t)\,x + \left[\frac{1}{2}\,M\,\dot{x}^2_{\mathrm{ref}}(t) + M\,x_{\mathrm{ref}}(t)\,\ddot{x}_{\mathrm{ref}}(t) - \dot{\bar{\gamma}}(t)\right]. \tag{6.26}$$

By using the Gauge freedom and setting

$$\gamma(t) = \bar{\gamma}(t) - M\,\left(x_{\mathrm{ref}}(t)\,\dot{x}_{\mathrm{ref}}(t) - x_{\mathrm{ref}}(0)\,\dot{x}_{\mathrm{ref}}(0)\right) = \frac{1}{2}\,M\int_0^t \mathrm{d}\,\tau\;\;\dot{x}^2_{\mathrm{ref}}(\tau) \tag{6.27}$$

the transformed Hamiltonians become identical and we can write

$$\boxed{\tilde{H}(t) = \frac{p^2}{2\,M} + V(x + x_{\mathrm{ref}}(t) - x_0(t)) - M\,\ddot{x}_{\mathrm{ref}}(t)\,x} \tag{6.28}$$

independent of the order of transformation. The transformation to the moving frame is described by the associated unitary operator

$$\mathrm{U}(t) = \exp\left(-\frac{M}{2\,\hbar}\int_0^t \mathrm{d}\,\tau\;\;\dot{x}^2_{\mathrm{ref}}(\tau)\right)\exp\left(-\frac{\mathrm{i}}{\hbar}\,M\,\dot{x}_{\mathrm{ref}}(t)\,x\right)\,\exp\left(-\frac{\mathrm{i}}{\hbar}\,x_{\mathrm{ref}}(t)\,p\right). \tag{6.29}$$

Lattice reference frame

In the lattice reference frame which moves with the potential minimum, $x_{\mathrm{ref}}(t) = x_0(t)$, the equation of motion is simplified dramatically. The Hamiltonian,

$$\boxed{\tilde{H}(t) = \frac{p^2}{2\,M} + V(x) - M\,\ddot{x}_0(t)\,x}, \tag{6.30}$$

is the sum of a static part defined by the time-independent potential and a time-dependent force, which is linear in position and results from the lattice acceleration $\ddot{x}_0(t)$.

Classical particle reference frame

For the classical particle reference frame we set $x_{\mathrm{ref}}(t) = x_{\mathrm{cl}}(t)$, where $x_{\mathrm{cl}}(t)$ is the solution to the Newtonian equation of motion

$$M\,\frac{\partial^2}{\partial\,t^2}\,x_{\mathrm{cl}}(t) = -\,\frac{\partial}{\partial\,x}V\,(x)\bigg|_{x=x_{\mathrm{cl}}(t)-x_0(t)} = -V'\,(x_{\mathrm{cl}}(t) - x_0(t))\;. \tag{6.31}$$

The moving frame Hamiltonian is then given by

$$\boxed{\tilde{H}(t) = \frac{p^2}{2\,M} + V(x + x_{\mathrm{cl}}(t) - x_0(t)) + V'\,(x_{\mathrm{cl}}(t) - x_0(t))\;x}, \tag{6.32}$$

where ‘ ’’ denotes the partial derivative in position.

A.4 Quantum simulation of atomic motion

We consider the time-dependent Schrödinger equation of the general form

$$\mathrm{i}\hbar\partial_t\psi(x,\,t) = H(x,\,t)\,\psi(x,\,t) = \left(\frac{p^2}{2\,M} + V(x,\,t)\right)\psi(x,\,t) \tag{6.33}$$

where $p = -\mathrm{i}\hbar\partial_x$ is the momentum operator and are interested in the time-dependent solutions $\psi(x,\,t)$ in position space.

Split-step operator method

If we assume that the Hamiltonian commutes with itself at different points in time, we can approximate the time evolution for small time steps δt as follows

$$\begin{aligned}
\psi(x,\,t+\delta t) &= \mathcal{U}_{t\to t+\delta t}\,\cdot\psi(x,\,t) \\
&= \exp\left[-\frac{\mathrm{i}}{\hbar}\int_t^{t+\delta t}\mathrm{d}\,\tau\;\; H(x,\,\tau)\right]\psi(x,\,t) \\
&= \exp\left[-\frac{\mathrm{i}}{\hbar}\left(-\frac{\hbar^2}{2\,M}\,\frac{\partial^2}{\partial\,x^2} + \int_t^{t+\delta t}\mathrm{d}\,\tau\;\; V(x,\,\tau)\right)\right]\cdot\psi(x,\,t) \\
&= \exp\left[-\frac{\mathrm{i}}{\hbar}\left(-\frac{\hbar^2}{2\,M}\,\frac{\partial^2}{\partial\,x^2} + \frac{V(x,\,t)+V(x,\,t+\delta t)}{2}\,\delta t + \mathcal{O}(\delta t^3)\right)\right]\cdot\psi(x,\,t)
\end{aligned} \tag{6.34}$$

where we used the trapezoidal rule to approximate the integral over $V(x,\,t)$ to third order in δt. The integration of the Schrödinger equation over all times can therefore be replaced by the much simpler step-wise propagation in small time steps $t = 0,\,\delta t,\,2\,\delta t,\,\ldots,\,T$.

However the the matrix exponential is in general difficult to calculate, since it is neither diagonal in the position or the momentum space representation. But we can further approximate the exponential using the Baker-Campbell-Hausdorff expansion [125] and therefore split the operator into parts, which are individually diagonal in position or momentum and hence more easy to calculate. Following the calculation in [44] we obtain

$$\mathcal{U}_{t\to t+\delta t} = \exp\left[-\frac{\mathrm{i}\,\delta t}{\hbar}\frac{V(x,\,t+\delta t)}{2}\right]\cdot\exp\left[\frac{\mathrm{i}\,\delta t}{\hbar}\,\frac{\hbar^2}{2\,M}\,\frac{\partial^2}{\partial\,x^2}\right]\cdot\exp\left[-\frac{\mathrm{i}}{\hbar}\frac{V(x,\,t)}{2}\,\delta t\right] + \mathcal{O}(\delta t^3) \tag{6.35}$$

exact to third order in δt. This is the so-called split-step operator representation.

By Fourier transforming $\psi(x,\,t)$ to obtain the wave function representation in momentum space, $\mathcal{F}\left\{\psi(x,\,t)\right\}(p)$, the time evolution for the step $t \to t+\delta t$ can be written as

$$\psi(x,\,t+\delta t) = \mathcal{U}_x(t+\delta t)\,\cdot\mathcal{F}^{-1}\left\{\mathcal{U}_p\,\cdot\mathcal{F}\left\{\mathcal{U}_x(t)\,\cdot\psi(x,\,t)\right\}(p)\right\}(x) \tag{6.36}$$

where the propagators $\mathcal{U}_p$ in momentum and $\mathcal{U}_x(t)$ in position space,

$$\mathcal{U}_p = \exp\left[-\frac{\mathrm{i}\,\delta t}{\hbar}\,\frac{p^2}{2\,M}\right],\qquad \mathcal{U}_x(t) = \exp\left[-\frac{\mathrm{i}\,\delta t}{\hbar}\,\frac{V(x,\,t)}{2\,\hbar}\right], \tag{6.37}$$

can be both expressed as diagonal matrices.

Bibliography

[1] A. D. Ludlow, M. M. Boyd, J. Ye, E. Peik, and P. O. Schmidt, Reviews of Modern Physics **87**, 637 (2015).

[2] T. Nicholson, S. Campbell, R. Hutson, G. Marti, B. Bloom, R. McNally, W. Zhang, M. Barrett, M. Safronova, G. Strouse, and et al., Nature Communications **6**, 6896 (2015).

[3] N. Huntemann, C. Sanner, B. Lipphardt, C. Tamm, and E. Peik, Physical Review Letters **116** (2016) 10.1103/physrevlett.116.063001.

[4] M. Schioppo, R. C. Brown, W. F. McGrew, N. Hinkley, R. J. Fasano, K. Beloy, T. H. Yoon, G. Milani, D. Nicolodi, J. A. Sherman, and et al., Nature Photonics **11**, 48 (2016).

[5] S. B. Koller, J. Grotti, S. Vogt, A. Al-Masoudi, S. Dörscher, S. Häfner, U. Sterr, and C. Lisdat, Physical Review Letters **118** (2017) 10.1103/physrevlett.118.073601.

[6] R. P. Feynman, International Journal of Theoretical Physics **21**, 467 (1982).

[7] M. Ben Dahan, E. Peik, J. Reichel, Y. Castin, and C. Salomon, Physical Review Letters **76**, 4508 (1996).

[8] D. Jaksch, C. Bruder, J. I. Cirac, C. W. Gardiner, and P. Zoller, Physical Review Letters **81**, 3108 (1998).

[9] M. Greiner, O. Mandel, T. Esslinger, T. W. Hänsch, and I. Bloch, Nature **415**, 39 (2002).

[10] T. Groh, S. Brakhane, W. Alt, D. Meschede, J. K. Asbóth, and A. Alberti, Physical Review A **94** (2016) 10.1103/physreva.94.013620.

[11] Y. Ji, Y. Chung, D. Sprinzak, M. Heiblum, D. Mahalu, and H. Shtrikman, Nature **422**, 415 (2003).

[12] E. Bocquillon, V. Freulon, J.-. M. Berroir, P. Degiovanni, B. Placais, A. Cavanna, Y. Jin, and G. Feve, Science **339**, 1054 (2013).

[13] K. von Klitzing, The Quantum Hall Effect, 1 (2005).

[14] C. Robens, "Testing the quantumness of atom trajectories", PhD Thesis (Universität Bonn, 2016).

[15] C. Robens, S. Brakhane, W. Alt, F. Kleißler, D. Meschede, G. Moon, G. Ramola, and A. Alberti, Optics Letters **42**, 1043 (2017).

[16] W. S. Bakr, A. Peng, M. E. Tai, R. Ma, J. Simon, J. I. Gillen, S. Folling, L. Pollet, and M. Greiner, Science **329**, 547 (2010).

[17] J. F. Sherson, C. Weitenberg, M. Endres, M. Cheneau, I. Bloch, and S. Kuhr, Nature **467**, 68 (2010).

[18] T. Xia, M. Lichtman, K. Maller, A. W. Carr, M. J. Piotrowicz, L. Isenhower, and M. Saffman, Physical Review Letters **114** (2015) 10.1103/physrevlett.114.100503.

[19] O. Mandel, M. Greiner, A. Widera, T. Rom, T. W. Hänsch, and I. Bloch, Nature **425**, 937 (2003).

[20] B. M. Terhal, Reviews of Modern Physics **87**, 307 (2015).

[21] A. G. Fowler, M. Mariantoni, J. M. Martinis, and A. N. Cleland, Physical Review A **86** (2012) 10.1103/physreva.86.032324.

[22] C. Robens, W. Alt, D. Meschede, C. Emary, and A. Alberti, Physical Review X ***5*** (2015) 10.1103/physrevx.5.011003.

[23] J. Cayssol, B. Dóra, F. Simon, and R. Moessner, physica status solidi (RRL) - Rapid Research Letters **7**, 101 (2013).

[24] J. K. Asbóth, Physical Review B **86** (2012) 10.1103/physrevb.86.195414.

[25] T. Kitagawa, M. S. Rudner, E. Berg, and E. Demler, Physical Review A **82** (2010) 10.1103/physreva.82.033429.

[26] C. Robens, S. Brakhane, W. Alt, D. Meschede, J. Zopes, and A. Alberti, Physical Review Applied **9** (2018) 10.1103/physrevapplied.9.034016.

[27] D. E. Kirk, *Optimal control theory – an introduction* (Dover Publications, 2004).

[28] G. Riviello, K. M. Tibbetts, C. Brif, R. Long, R.-B. Wu, T.-S. Ho, and H. Rabitz, Physical Review A **91** (2015) 10.1103/physreva.91.043401.

[29] D. Meshulach and Y. Silberberg, Nature **396**, 239 (1998).

[30] R. J. Levis, Science **292**, 709 (2001).

[31] T. Brixner, N. H. Damrauer, G. Krampert, P. Niklaus, and G. Gerber, Journal of Modern Optics **50**, 539 (2003).

[32] L. Viola and S. Lloyd, Physical Review A **58**, 2733 (1998).

[33] S. van Frank, M. Bonneau, J. Schmiedmayer, S. Hild, C. Gross, M. Cheneau, I. Bloch, T. Pichler, A. Negretti, T. Calarco, and S. Montangero, Scientific Reports **6**, 34187, 34187 (2016), arXiv:1511.02247 [quant-ph].

[34] R. Bücker, J. Grond, S. Manz, T. Berrada, T. Betz, C. Koller, U. Hohenester, T. Schumm, A. Perrin, and J. Schmiedmayer, Nature Physics **7**, 608 (2011).

[35] S. van Frank, A. Negretti, T. Berrada, R. Bücker, S. Montangero, J.-F. Schaff, T. Schumm, T. Calarco, and J. Schmiedmayer, Nature Communications ***5*** (2014) 10.1038/ncomms5009.

[36] H. A. Fürst, M. H. Goerz, U. G. Poschinger, M. Murphy, S. Montangero, T. Calarco, F. Schmidt-Kaler, K. Singer, and C. P. Koch, New Journal of Physics **16**, 075007 (2014).

[37] J. J. W. H. Sørensen, M. K. Pedersen, M. Munch, P. Haikka, J. H. Jensen, T. Planke, M. G. Andreasen, M. Gajdacz, K. Mølmer, A. Lieberoth, and et al., Nature ***532***, 210 (2016).

[38] D. Sels, ArXiv e-prints (2017), arXiv:1709.08766 [quant-ph].

[39] S. Deffner and S. Campbell, Journal of Physics A: Mathematical and Theoretical ***50***, 453001 (2017).

[40] I. H. Deutsch and P. S. Jessen, Physical Review A ***57***, 1972 (1998).

[41] D. Jaksch, H.-J. Briegel, J. I. Cirac, C. W. Gardiner, and P. Zoller, Physical Review Letters **82**, 1975 (1999).

[42] M. Karski, L. Forster, J.-M. Choi, A. Steffen, W. Alt, D. Meschede, and A. Widera, Science **325**, 174 (2009).

[43] R. Grimm, M. Weidemüller, and Y. B. Ovchinnikov, Advances In Atomic, Molecular, and Optical Physics, 95 (2000).

[44] D. A. Steck, *Quantum and atom optics*, Available online at http://steck.us/teaching, Revision 0.12.0, May 2017.

[45] M. Karksi, "State-selective transport of single neutral atoms", PhD Thesis (Universität Bonn, 2010).

[46] A. Alberti, W. Alt, R. Werner, and D. Meschede, New Journal of Physics **16**, 123052 (2014).

[47] É. Mathieu, Journal de Mathématiques Pures et Appliquées **13**, 137 (1868).

[48] H. J. W. Müller and R. B. Dingle, Journal für die reine und angewandte Mathematik (Crelles Journal) **1962** (1962) 10.1515/crll.1962.211.11.

[49] J. Meixner, F. W. Schäfke, and G. Wolf, Lecture Notes in Mathematics (1980) 10.1007/bfb0096194.

[50] W. R. Inc., *Mathematica, Version 11.3*, Champaign, IL, 2018.

[51] MATLAB, *Matlab, Version 2017a*, Champaign, IL, 2018.

[52] F. A. Alhargan, ACM Transactions on Mathematical Software **32**, 472 (2006).

[53] K. J. Åström and R. M. Murray, *Feedback systems – an introduction for scientists and engineers* (Princeton University Press, 2008).

[54] M. Werninghaus, "Controlling atom transport in a two-dimensional state-dependent optical lattice", Master Thesis (Universität Bonn, 2017).

[55] B. E. A. Saleh and M. C. Teich, *Fundamentals of photonics*, Wiley series in pure and applied optics (Wiley, 1991).

[56] C. Raman and N. N. Nathe, Proc. Indian Acad. Sci. (Math. Sci.) **2**, 406 (1935).

[57] M. Bass, E. W. V. Stryland, D. R. Williams, and W. L. Wolfe, *Handbook of optics volume ii devices, measurements, and properties 2nd edition* (McGraw-Hill, INC, 1995).

[58] S. Hild, "Resolved raman sideband cooling in a doughnut-shaped optical trap", Master Thesis (Universität Bonn, 2011).

[59] K. Ogata, *Modern control engineering*, 5th ed. (Prentice Hall PTR, Upper Saddle River, NJ, USA, 2001).

[60] MATLAB *Control System Toolbox*, Version 2017a, The MathWorks, Natick, Massachusetts, USA.

[61] D. J. Wineland and W. M. Itano, Physical Review A **20**, 1521 (1979).

[62] H. Perrin, A. Kuhn, I. Bouchoule, and C. Salomon, Europhysics Letters (EPL) **42**, 395 (1998).

[63] S. E. Hamann, D. L. Haycock, G. Klose, P. H. Pax, I. H. Deutsch, and P. S. Jessen, Physical Review Letters **80**, 4149 (1998).

[64] M. Johanning, A. Braun, N. Timoney, V. Elman, W. Neuhauser, and C. Wunderlich, Physical Review Letters **102** (2009) 10.1103/physrevlett.102.073004.

[65] N. Belmechri, L. Förster, W. Alt, A. Widera, D. Meschede, and A. Alberti, Journal of Physics B: Atomic, Molecular and Optical Physics **46**, 104006 (2013).

[66] L. Förster, "Microwave control of atomic motion in a spin dependent optical lattice", PhD Thesis (Universität Bonn, 2010).

[67] S. Blatt, J. W. Thomsen, G. K. Campbell, A. D. Ludlow, M. D. Swallows, M. J. Martin, M. M. Boyd, and J. Ye, Physical Review A **80** (2009) 10.1103/physreva.80.052703.

[68] N. Peter, "Optimal control of vibrational dynamics of single neutral atoms", PhD Thesis (Universität Bonn, 2018 (to be published)).

[69] D. Stefanatos and J.-S. Li, IEEE Transactions on Automatic Control **59**, 733 (2014).

[70] M. Born and V. Fock, Zeitschrift für Physik **51**, 165 (1928).

[71] A. Walther, F. Ziesel, T. Ruster, S. T. Dawkins, K. Ott, M. Hettrich, K. Singer, F. Schmidt-Kaler, and U. Poschinger, Physical Review Letters **109** (2012) 10.1103/physrevlett.109.080501.

[72] R. Bowler, J. Gaebler, Y. Lin, T. R. Tan, D. Hanneke, J. D. Jost, J. P. Home, D. Leibfried, and D. J. Wineland, Physical Review Letters **109** (2012) 10.1103/physrevlett.109.080502.

[73] D. Schrader, S. Kuhr, W. Alt, M. Müller, V. Gomer, and D. Meschede, Applied Physics B **73**, 819 (2001).

[74] M. Genske, W. Alt, A. Steffen, A. H. Werner, R. F. Werner, D. Meschede, and A. Alberti, Physical Review Letters **110** (2013) 10.1103/physrevlett.110.190601.

[75] C. Robens, W. Alt, C. Emary, D. Meschede, and A. Alberti, Applied Physics B **123** (2016) 10.1007/s00340-016-6581-y.

[76] J. Werschnik and E. K. U. Gross, Journal of Physics B: Atomic, Molecular and Optical Physics **40**, R175 (2007).

[77] L. Pontryagin, V. Boltyanskii, R. Gamkrelidze, and E. Mishchenko, *The mathematical theory of optimal processes* (John Wiley and Sons (Interscience Publishers), New York, 1962).

[78] A. Couvert, T. Kawalec, G. Reinaudi, and D. Guéry-Odelin, EPL (Europhysics Letters) **83**, 13001 (2008).

[79] A. Bryson, IEEE Control Systems Magazine **16**, 26 (1996).

[80] J. Bernoulli, *Problema novum ad cujus solutionem mathematici invitantur. (a new problem to whose solution mathematicians are invited.)* Acta eruditorum 18 (1696).

[81] H. Sussmann and J. Willems, IEEE Control Systems **17**, 32 (1997).

[82] C. Brif, R. Chakrabarti, and H. Rabitz, New Journal of Physics **12**, 075008 (2010).

[83] J. Guerrero and F. F. López-Ruiz, Physica Scripta **90**, 074046 (2015).

[84] E. Torrontegui, S. Ibáñez, X. Chen, A. Ruschhaupt, D. Guéry-Odelin, and J. G. Muga, Physical Review A **83** (2011) 10.1103/physreva.83.013415.

[85] D. Guéry-Odelin and J. G. Muga, Physical Review A **90** (2014) 10.1103/physreva.90.063425.

[86] F. M. Leupold, "Bang-bang control of a trapped-ion oscillator", PhD Thesis (ETH Zürich, 2015).

[87] X. Chen, E. Torrontegui, D. Stefanatos, J.-S. Li, and J. G. Muga, Physical Review A **84** (2011) 10.1103/physreva.84.043415.

[88] M. Palmero, E. Torrontegui, D. Guéry-Odelin, and J. G. Muga, Physical Review A **88** (2013) 10.1103/physreva.88.053423.

[89] E. Torrontegui, X. Chen, M. Modugno, S. Schmidt, A. Ruschhaupt, and J. G. Muga, New Journal of Physics **14**, 013031 (2012).

[90] S. Schulz, U. Poschinger, K. Singer, and F. Schmidt-Kaler, Fortschritte der Physik **54**, 648 (2006).

[91] D. J. Tannor, V. A. Kazakov, and V. Orlov, in *Time-dependent quantum molecular dynamics*, edited by J. Broeckhove and L. Lathouwers (NATO ASI, Ser. B, Plenum, New York, 1992).

[92] N. Khaneja, T. Reiss, C. Kehlet, T. Schulte-Herbrüggen, and S. J. Glaser, Journal of Magnetic Resonance **172**, 296 (2005).

[93] T. Caneva, T. Calarco, and S. Montangero, Physical Review A **84** (2011) 10.1103/physreva.84.022326.

[94] N. Rach, M. M. Müller, T. Calarco, and S. Montangero, Physical Review A **92** (2015) 10.1103/physreva.92.062343.

[95] R. Reichle, D. Leibfried, R. B. Blakestad, J. Britton, J. Jost, E. Knill, C. Langer, R. Ozeri, S. Seidelin, and D. J. Wineland, Elements of Quantum Information, 69.

[96] G. De Chiara, T. Calarco, M. Anderlini, S. Montangero, P. J. Lee, B. L. Brown, W. D. Phillips, and J. V. Porto, Physical Review A **77** (2008) 10.1103/physreva.77.052333.

[97] S. Rosi, A. Bernard, N. Fabbri, L. Fallani, C. Fort, M. Inguscio, T. Calarco, and S. Montangero, Physical Review A **88** (2013) 10.1103/physreva.88.021601.

[98] S. An, D. Lv, A. del Campo, and K. Kim, Nature Communications **7**, 12999 (2016).

[99] R. H. Byrd, M. E. Hribar, and J. Nocedal, SIAM Journal on Optimization **9**, 877 (1999).

[100] R. H. Byrd, J. C. Gilbert, and J. Nocedal, Mathematical Programming **89**, 149 (2000).

[101] R. Waltz, J. Morales, J. Nocedal, and D. Orban, Mathematical Programming **107**, 391 (2005).

[102] MATLAB *Optimization Toolbox,* Version 2017a, The MathWorks, Natick, Massachusetts, USA.

[103] R. Wu, A. Pechen, H. Rabitz, M. Hsieh, and B. Tsou, Journal of Mathematical Physics **49**, 022108 (2008).

[104] A. N. Pechen and D. J. Tannor, Physical Review Letters **106** (2011) 10.1103/physrevlett.106.120402.

[105] P. De Fouquieres and S. G. Schirmer, Infinite Dimensional Analysis, Quantum Probability and Related Topics **16**, 1350021 (2013).

[106] T.-S. Ho and H. Rabitz, Journal of Photochemistry and Photobiology A: Chemistry **180**, 226 (2006).

[107] D. V. Zhdanov and T. Seideman, Physical Review A **92** (2015) 10.1103/physreva.92.052109.

[108] L. Mandelstam and I. Tamm, Selected Papers, 115 (1991).

[109] A. del Campo, I. L. Egusquiza, M. B. Plenio, and S. F. Huelga, Physical Review Letters **110** (2013) 10.1103/physrevlett.110.050403.

[110] D. Mondal, C. Datta, and S. Sazim, Physics Letters A **380**, 689 (2016).

[111] M. M. Taddei, B. M. Escher, L. Davidovich, and R. L. de Matos Filho, Physical Review Letters **110** (2013) 10.1103/physrevlett.110.050402.

[112] S. Deffner and E. Lutz, Physical Review Letters **111** (2013) 10.1103/physrevlett.111.010402.

[113] I. Marvian and D. A. Lidar, Physical Review Letters **115** (2015) 10.1103/physrevlett.115.210402.

[114] M. Okuyama and M. Ohzeki, Physical Review Letters **120** (2018) 10.1103/physrevlett.120.070402.

[115] B. Shanahan, A. Chenu, N. Margolus, and A. del Campo, Physical Review Letters **120** (2018) 10.1103/physrevlett.120.070401.

[116] Q. Zhang, J. G. Muga, D. Guéry-Odelin, and X. Chen, Journal of Physics B: Atomic, Molecular and Optical Physics **49**, 125503 (2016).

[117] J. Goh and M. Sim, Operations Research **59**, 973 (2011).

[118] D. Bures, Transactions of the American Mathematical Society **135**, 199 (1969).

[119] J. Hilgevoord, American Journal of Physics **70**, 983 (2002).

[120] J. Uffink, American Journal of Physics **61**, 935 (1993).

[121] N. Margolus and L. B. Levitin, Physica D: Nonlinear Phenomena **120**, 188 (1998).

[122] L. B. Levitin and T. Toffoli, Physical Review Letters **103** (2009) 10.1103/physrevlett.103.160502.

[123] C. Brif, M. D. Grace, M. Sarovar, and K. C. Young, New Journal of Physics **16**, 065013 (2014).

[124] W. Klink and S. Wickramasekara, Annals of Physics **340**, 94 (2014).

[125] R. M. Wilcox, Journal of Mathematical Physics **8**, 962 (1967).

Acknowledgements

First, I would like to thank Professor Meschede for giving me the opportunity to join his research group, in which I spent the most interesting, but also most challenging years of my life at the university, for the advisory and financial support during my work and the opportunity to write this thesis, as well as the chance to participate with my own ideas and work in the scientific world. I would also like to thank Professor Weitz for kindly agreeing to be my second supervisor.

Furthermore, I like to thank Wolfgang Alt and Andrea Alberti for all the motivating and fruitful discussions. I particularly like to thank Andrea as my supervisor for his continuous flow of ideas and for his helpful comments and feedback on any topic I came up with, independently of his own workload, time of day or night. Also I like to thank him for always strengthening my ambitions in my work, motivating me to do and reach more and for his never-ending effort to bring the whole team together and making the institute a productive and simultaneously very welcome place.

I would like to thank my team, Natalie Peter, Carsten Robens and especially Manolo Rivera for the really good teamwork in the lab and for the continuous and fruitful discussions. Thank you for introducing me to the lab, for standing my everlasting curiosity and questions and for always making me feel welcome. You made this work so productive and most importantly a lot of fun.

Most importantly, I would like to thank Fredi, my fiancé for keeping the healthy balance between the lab and the live outside the institute, for being sympathetic, even when I stayed longer, for distracting me from work, reminding me to eat and drink, for always supporting me in my work and for filling my life with all these wonderful and priceless memories.

Last but not least, I like to thank my family: my parents, my brother and my sister for their never ending support, their curiosity in my work and for all the great weekends we spent together on which I could relax and distract me from work.

Declaration of Authorship

I hereby declare that the work presented here was formulated by myself and that no sources or tools other than those cited were used.

Bonn, 30 April 2018

Thorsten Groh